

Cover Page



Universiteit Leiden



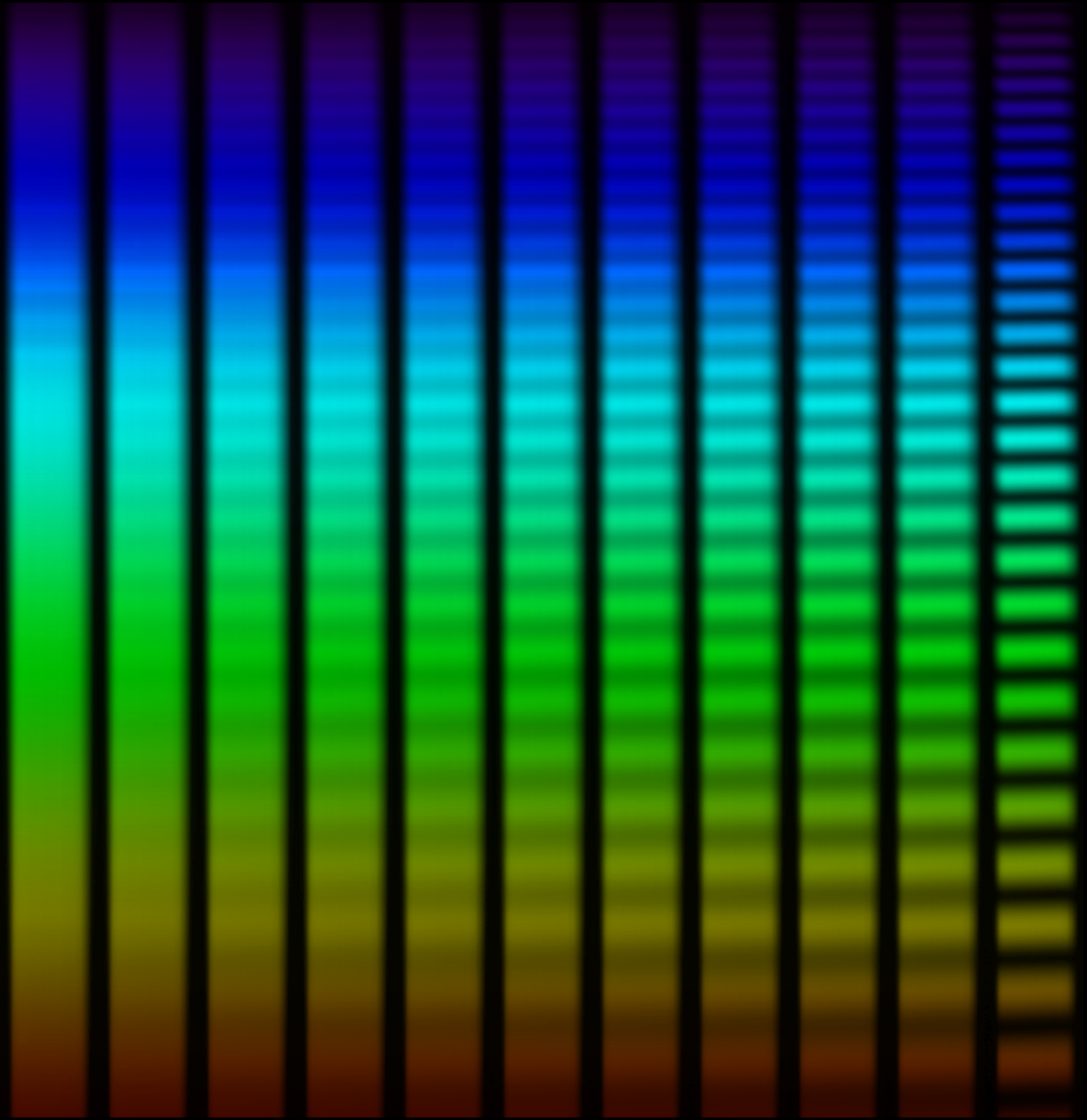
The handle <http://hdl.handle.net/1887/29978> holds various files of this Leiden University dissertation

Author: Harten, Gerard van

Title: Spectropolarimetry for planetary exploration

Issue Date: 2014-12-08

Spectropolarimetry for planetary exploration



Gerard van Harten

Spectropolarimetry for planetary exploration

© 2014 Gerard van Harten
Alle rechten voorbehouden

ISBN 978-94-6259-458-6

Cover image: Spectropolarimetric measurements of visible light with an increasing degree of linear polarization from unpolarized (left) to fully polarized (right), obtained with the Spectropolarimeter for Planetary EXploration (SPEX).

Spectropolarimetry for planetary exploration

Proefschrift

ter verkrijging van
de graad van Doctor aan de Universiteit Leiden,
op gezag van Rector Magnificus prof. mr. C. J. J. M. Stolker,
volgens besluit van het College voor Promoties
te verdedigen op maandag 8 december 2014
klokke 13:45 uur

door

Gerrit van Harten

geboren te Katwijk
in 1984

Promotor:

Prof. dr. Christoph U. Keller

Co-promotor:

Dr. ir. Frans Snik

Overige leden promotiecommissie:

Dr. Matthew A. Kenworthy

Prof. dr. Jérôme C. Riedi (Laboratoire d'Optique Atmosphérique, France)

Prof. dr. Huub J.A. Röttgering

Prof. dr. H. Paul Urbach (Technische Universiteit Delft)

Contents

1	Introduction	1
1.1	Polarimetry of planetary atmospheres	1
1.2	Earth atmosphere	3
1.3	Aerosol measurements	6
1.4	Light scattering and polarization	7
1.5	Atmospheric scattering measurements	12
1.6	Measuring polarization	15
1.7	Polarimeter performance and calibration	19
1.8	Brief history of SPEX	20
1.9	Thesis outline	21
1.10	Outlook	23
2	Prototyping for the Spectropolarimeter for Planetary EXploration (SPEX): calibration and sky measurements	27
2.1	Introduction	29
2.2	SPEX instrument principle	30
2.3	Prototype design	33
2.4	Prototype results	36
2.5	Outlook	41
3	Performance of spectrally modulated polarimetry I: Error analysis and optimization	45
3.1	Introduction	46
3.2	Instrument	47
3.3	Measurement formalism	49
3.4	Error analysis	53
3.5	Static errors	56
3.6	Dynamic errors	60
3.7	End-to-end simulation	68
3.8	Conclusions	71
4	Performance of spectrally modulated polarimetry	

II: Data reduction and absolute polarization calibration of a prototype SPEX satellite instrument	73
4.1 Introduction	74
4.2 SPEX instrument	74
4.3 Data reduction pipeline	78
4.4 Polarization calibration stimulus	84
4.5 SPEX polarimetric calibration	89
4.6 Discussion	93
4.7 Conclusions	95
5 Atmospheric aerosol characterization with a ground-based SPEX spectropolarimetric instrument	97
5.1 Introduction	98
5.2 Measurements	99
5.3 Aerosol retrieval	107
5.4 Results	108
5.5 Discussion	110
5.6 Conclusions and Outlook	112
6 Spectral line polarimetry with a channeled polarimeter	115
6.1 Introduction	116
6.2 Method	118
6.3 Error analysis	122
6.4 Application of line polarimetry to the O ₂ A absorption band	125
6.5 Conclusions	128
Bibliography	131
Samenvatting	141
Curriculum Vitae	147
Acknowledgements	149

Chapter 1

Introduction

Remote characterization of atmospheric aerosols is important because of their impact on public health and climate. To retrieve aerosol concentration and microphysical properties, such as size, shape, and chemical composition, accurate measurements of the intensity, color and polarization of the sky are required at different scattering angles. Polarization is an intrinsic property of light, but unlike intensity and color, it is not visible to the naked eye. However, it can be made visible by filtering light with a certain polarization state using a polarizer. This is used in Polaroid sunglasses to suppress bright, strongly polarized reflections off the road or water, or in modern 3D theater glasses to create depth perception using two slightly shifted images with different polarization states. Any interaction of light with a material, e.g. reflection, refraction or diffraction, changes its polarization state. In fact, the polarization state of sunlight scattered by aerosols in the atmosphere carries more information about the scattering particles than the intensity.

An early example of the power of multi-angle multi-wavelength intensity and polarization measurements is the detailed characterization of clouds on Venus from the Earth. Instrumentation for in-orbit characterization of aerosols in the Earth's atmosphere is still under development; in particular the accuracy of the polarization measurement needs an order of magnitude improvement, which requires groundbreaking concepts for both the instrument and calibration. This drives the development, verification, and field-deployment of the highly accurate Spectropolarimeter for Planetary EXploration (SPEX), as described in this thesis.

1.1 Polarimetry of planetary atmospheres

Detailed characterization of the composition of planetary atmospheres using polarimetry goes back to the year 1929, with Lyot's PhD thesis presenting his "Research

on the polarization of light from planets and from some terrestrial substances" (Lyot 1929). His work includes accurate measurements of the broadband visible polarization of Venus at phase angles¹ of 2–176°, as shown in Fig. 1.1a. The strong polarization peak around 15° indicates a rainbow, caused by liquid droplets, and the peak around 160° is typical forward scattering polarization. Comparison with lab scattering measurements of a large variety of samples led to the conclusion that Venus is covered in opaque clouds with droplet sizes of $\sim 2 \mu\text{m}$ and a refractive index close to water.

In the next decades, several radiometric and spectroscopic observations confirmed that the Venusian surface is hidden behind opaque clouds, but their chemical composition remained unknown. More than a dozen postulated compositions were compatible with the observed intensity distribution across the disk, the intensity as a function of planetary phase angle, and spectral absorption lines and bands. In the sixties, additional polarization measurements were taken in multiple wavelength bands within 340–1050 nm by Dollfus (1966), Coffeen & Gehrels (1969), Dollfus & Coffeen (1970). Researchers in Leiden realized the potential wealth of information in Lyot's and this multi-dimensional data, and developed a full radiative transfer model, including polarization and multiple scattering (Hansen 1971, Hovenier 1971). They ran the atmospheric model for years to obtain a definitive fit for the particle size distribution (Fig. 1.1a) and the spectral refractive index (Fig. 1.1b) that showed that Venus is covered in clouds of concentrated sulfuric acid (Fig. 1.1c) (Hansen & Hovenier 1974).

These results were confirmed by in-situ nephelometer and particle size spectrometer measurements onboard entry probes of the Pioneer Venus Multiprobe and Venera spacecraft a few years later (Knollenberg & Hunten 1980, Marov et al. 1980, Ragent & Blamont 1980). Compared to the disk-integrated Earth-based observations, the descents to the surface provided a detailed profile of the 60 km thick multilayered sulfuric acid cloud and haze system, on top of the 96.5% carbon dioxide atmosphere in the lower 30 km, giving rise to a surface temperature of 740 K and pressure of 93 bar (Basilevsky & Head 2003). These extreme atmospheric conditions, obviously not compatible with human life, are believed to be the result of a runaway greenhouse effect (Rasool & de Bergh 1970).

The groundbreaking interpretation of the polarization of Venus is now applied to the modeling of polarized signals from exoplanets, and the polarimetric characterization of aerosols and clouds in the Earth's atmosphere. For example, disk-integrated polarization measurements of the Earth, as if it were an exoplanet, contain information about the fractional coverage by clouds, oceans, and vegetation (Sterzik et al. 2012). A polarization peak is observed at the Oxygen A absorption band, indicating a large abundance of molecular oxygen, which may serve as a biosignature. The polarized rainbow feature provides a sensitive method for the detection of liquid water clouds on exoplanets, which is a prerequisite for life as we know it (Karalidi et al. 2012).

¹Scattering angle equals 180° minus phase angle.

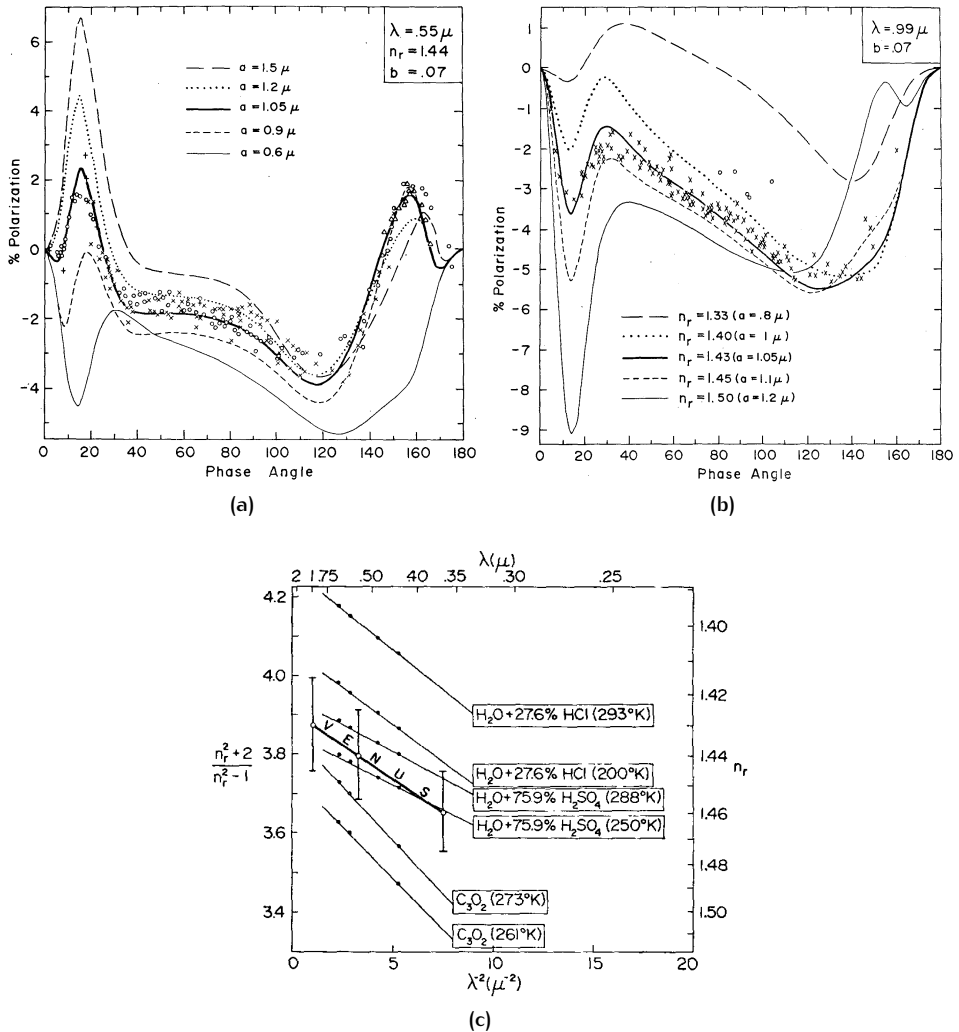


Figure 1.1: The composition of the clouds that cover Venus is discovered using ground-based polarimetry. (a)-(b) Model calculations (lines) are fitted to measurements (symbols) of the degree of linear polarization at multiple phase angles, for various (a) particle sizes a [μm] and (b) refractive indices n_r . (c) The chemical composition is uniquely determined as concentrated sulfuric acid via the spectral refractive index. *Figures from Hansen & Hovenier (1974).*

1.2 Earth atmosphere

The scientific goal of this thesis is the characterization of the Earth's atmosphere, in particular the aerosols in it. Compared to the Earth's radius of 6371 km, the

thickness of the atmosphere is only 100 km. Eighty percent of the atmosphere is contained in the troposphere, the lowest 12 km where weather takes place. The aerosols are mainly located in the lowest kilometer, the planetary boundary layer, where vertical mixing is strongest due to the friction of the Earth's surface on wind, and further upward mixing is inhibited by an inversion layer. However, Saharan dust, volcanic ash, and forest fire smoke sometimes reach higher parts of the atmosphere. Heat is transported from the Earth's surface into the troposphere via convection, so overall the temperature decreases with altitude. In the stratosphere at 12–50 km the temperature goes up again, due to the absorption of solar ultraviolet radiation in the ozone layer. Less than 0.1% of the atmosphere is in the even higher layers, where meteors burn up and aurorae take place.

1.2.1 Aerosols

Aerosols, also known as particulate matter, are particles or droplets suspended in the air. Some types are naturally occurring, such as sea salt, desert dust, and volcanic ash, others are mostly anthropogenic, such as sulfates, nitrates, soot, smoke and ashes from combustion or forest fires, or ammonia salts from agriculture. The sulfates, nitrates and ammonia salts are secondary aerosols, meaning that they are emitted into the atmosphere as gas where they are transformed into particles, in contrast to primary aerosols that started as particles. Aerosols typically have lifetimes of days to weeks before they leave the atmosphere, mainly by rainout, washout, and sweep out. A particle is rained out when a water droplet condenses on it to the point that it precipitates in the form of a raindrop, washout occurs when a particle is incorporated in an existing droplet, and sweep out means that a particle is bombarded by a raindrop. Because of the short lifetimes, transportation by the wind is typically limited to 100–1000 km. The locality of aerosol sources, and their limited transportation ranges cause large regional variations in aerosol load. Note that the deposition of aerosols that reach stratospheric altitudes is less efficient. For example, the eruption of Mount Pinatubo in 1991 released ~ 20 million tons of sulfur dioxide in the atmosphere, that transformed into a global haze of sulfuric acid, causing a global temperature decrease of 0.5 °C for about two years (Hansen et al. 1993).

1.2.2 Climate

Aerosols and clouds influence the Earth's climate by altering its radiative balance. Their direct radiative effect consists of the scattering of sunlight, partly back into space, as well as absorption, particularly in the case of black carbon (McCormick & Ludwig 1967, Ramanathan & Carmichael 2008). Aerosols also affect climate indirectly, because they can act as cloud condensation nuclei, leading to more and smaller cloud droplets (Twomey 1977, Kaufman et al. 2005). This results in increased cloud albedo (reflectivity) and longer cloud lifetimes, because the smaller droplets decrease the precipitation efficiency. The impacts of specific aerosol types

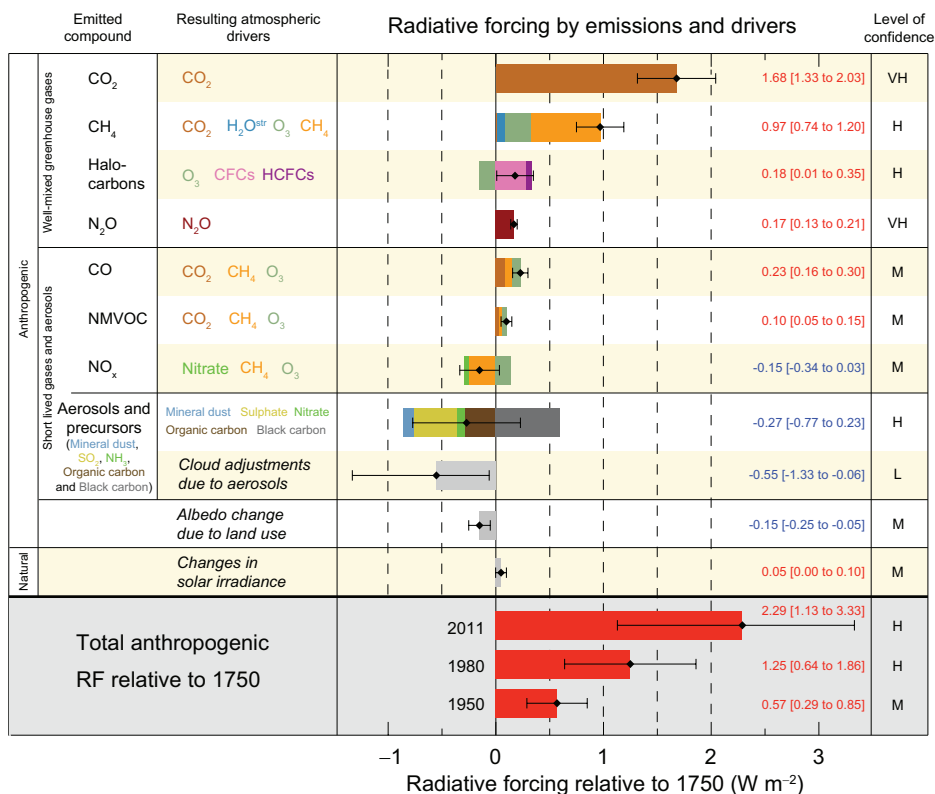


Figure 1.2: The change in the Earth's radiative balance between the pre-industrial era (1750) and the year 2011. Greenhouse gases (upper panel) have a clear warming effect, whereas aerosols (third panel) are the major source of cooling. The uncertainty in the total radiative forcing is dominated by the large error bars on the effect of aerosols. *Figure from IPCC (2013).*

on climate, cloud properties, and precipitation patterns, remain uncertain as particle concentrations, size, shape, and chemical composition are not measured with sufficient accuracy and spatial resolution to resolve their regional variety (IPCC 2013). Figure 1.2 shows the current knowledge of the global anthropogenic aerosol radiative forcing in terms of their direct and indirect effects; the cooling effect of aerosols, although significant in size, is highly uncertain compared to the warming effect of greenhouse gases like CO₂. Therefore, in spite of accurate long-term records of temperature and greenhouse gases, there is a large uncertainty in the climate sensitivity through the uncertainty in the net change in radiative forcing, such that projections for global temperature change in the year 2100 vary by about 2 °C. To reduce this uncertainty, accurate measurements of aerosol properties are needed on a global scale at high spatial resolution.

1.2.3 Air quality

Exposure to particulate matter air pollution also has major adverse human health impacts, including asthma attacks, heart and lung diseases, and premature mortality (Anderson et al. 2011). Particulate matter smaller than 10 micrometer (referred to as PM₁₀) can enter the bronchi, and the smaller and lighter the particles are, the deeper they can penetrate into the lungs. Chemical composition is believed to play a significant role in toxicity; black-carbon (soot)-containing aerosols associated with vehicular traffic appear to be particularly toxic. More accurate measurements of aerosol size and chemical composition are needed to study the links between pollution and public health.

1.2.4 Air traffic

Eruptions of the Icelandic Eyjafjallajökull volcano in 2010 caused major air traffic disruptions, leading to millions of stranded passengers, and an economic damage for the air carriers of over a billion euros. Large parts of the European airspace were closed for safety reasons, due to the damaging effect of ash particles on airplane engines. According to new European guidelines, airplanes are still allowed to fly in regions with ash concentrations below 2 mg/m³, which is about 3 orders of magnitude more than usual (EASA 2013). Accurate concentration measurements with large spatial coverage are needed to identify safe regions and reduce the air traffic downtime; characterization of the microphysical properties improves the forecasting of ash transport and dispersion.

1.3 Aerosol measurements

1.3.1 Particulate matter monitoring

To protect human health, governments set air quality standards, and monitor PM₁₀ and PM_{2.5} levels. These are the most prevalent in-situ aerosol measurements, and are performed in a standardized way. Air is sucked through sampling heads that let particles pass that have a diameter smaller than 10 or 2.5 μm , respectively. The accumulated particles are manually weighed according to the reference method, which is the official method for regulatory compliance and (inter)national comparison. Instead of the expensive and time-consuming manual weighing, often automated measurements are performed of the extinction of beta radiation by the contaminated filter. These automated measurements have to be calibrated frequently using the reference method. The filters can be analyzed in the laboratory to determine the particles' shape and chemical composition.

PM monitoring provides direct measurements of aerosol mass concentration in two particle size groups at ground level, which is the most relevant location for public health, on an hourly basis, but at a limited spatial coverage. For example, the National Air Quality Monitoring Network in the Netherlands (<http://www.lm1.nl>).

rivm.nl) consists of about 60 monitoring stations in different scenes, for example rural areas, urban areas, close to traffic or close to industrial or agricultural activity, which is on average one per 700 square kilometers.

1.3.2 Sunphotometry

AERONET (Aerosol Robotic Network) is a global ground-based measurement network with about 400 stations in 50 countries on all continents, that is mainly used for validation of satellite measurements (Holben et al. 1998). AERONET employs sunphotometers to measure the extinction (i.e. scattering plus absorption) of direct sunlight due to the total aerosol column. Although this aerosol optical thickness (AOT) measurement itself is reliable, it cannot discriminate between the amount of aerosols and the intrinsic extinction capability (aerosol extinction coefficient) of that particular type of aerosols. The AOT is measured in a few spectral bands, to obtain a rough measure of aerosol size: the size of a particle relative to different wavelengths varies rapidly for small particles, and therefore the interaction is highly wavelength dependent, whereas large particles like water droplets exhibit a spectrally flat behavior. Empirical relationships between the AOT of the total aerosol column and PM at ground level have been established, but the correlation remains weak (e.g. Schaap et al. 2009).

1.3.3 Lidar

Lidar is an active remote sensing technique, in contrast to the various passive techniques discussed in this thesis which use the Sun as light source. A lidar instrument sends laser pulses into the atmosphere, and measures the arrival times and intensities of the backscattered light. This results in altitude profiles of the aerosol extinction coefficient. The use of multiple wavelengths gives an indication of particle size, and a depolarization measurement provides information on the aerosol type (e.g. Murayama et al. 1999).

1.4 Light scattering and polarization

It is crucial for our understanding of the impact of atmospheric aerosols on climate and public health to be able to remotely characterize the physical properties of the aerosols, in terms of size, shape and chemical composition. The information content in the direct sun measurements is not large enough for that, and this technique only works from the ground. The measurement dimensionality is greatly increased by looking away from the Sun, to measure the sunlight that is scattered in the atmosphere.

The physical mechanisms behind scattering depend on the size d of the scatterer with respect to the wavelength λ of the light. Note that the size of a molecule is

in the order of nanometers, whereas aerosols and cloud droplets are in the order of 1–10 μm , i.e. 4 orders of magnitude difference.

Rayleigh scattering is the re-radiation of incoming light in all directions by e.g. air molecules with $d \ll \lambda$. To understand this, we should think of light as transverse electromagnetic waves, consisting of an electric and a magnetic field, both oscillating perpendicular to each other and to the direction of propagation. When encountering a small particle, the electric field applies a force to the electrons inside the particle, such that they start oscillating along with the electric field. This oscillating dipole moment in turn emits radiation in all directions, except in the direction of oscillation, i.e. along the dipole axis. This implies that the observed intensity depends on the scattering geometry (location of light source, scattering particle, and observer) and the oscillation direction of the electric field, called the linear polarization direction, as depicted in Fig. 1.3.

A beam of light consists of many electromagnetic waves, that may have different polarization directions. In the most extreme case there is no preferred direction of the electric field, and the light is unpolarized, as is the case for the incoming sunlight. If there is a net polarization, it is described by the angle of linear polarization (ϕ_L) and the degree of linear polarization (P_L), the fraction of the total intensity that is linearly polarized. Figure 1.3 shows that a scattering event at larger angles increases P_L up to 100% at a 90° scattering angle, while decreasing the intensity.

The reason why the sky is blue is the $1/\lambda^4$ wavelength dependence of the Rayleigh scattering efficiency, which is a factor 16 more efficient at 400 nm than at 800 nm. Rayleigh scattering is also responsible for red sunsets: on their long horizontal way through the atmosphere, much more blue than red light gets scattered out of the direct sunlight, leaving a red Sun.

Mie scattering applies for the $d \approx \lambda$ regime, as is the case for cloud droplets and aerosols. It is named after Gustav Mie, who derived exact expressions for the intensity and polarization scattered by a spherical particle, by solving Maxwell's equations (Mie 1908). Extensions have been made to account for non-spherical particles with various shapes (Mishchenko et al. 2000).

The scattering process is a combination of diffraction and reflection off the particle, refraction when entering or exiting it, and interference inside the particle. All these effects exhibit different intensity and polarization properties, and different dependencies on wavelength, scattering angle, particle size, and particle refractive index, giving rise to characteristic scattering signals with high sensitivity to the particle's microphysical properties. For example, a rainbow is created at scattering angles around 138° due to light that refracts when entering a droplet, gets reflected on the backside, and refracts again when exiting the particle, as shown in Fig. 1.4. The refraction angles are slightly wavelength dependent, due to dispersion of the refractive index, which creates the color effect. In polarization, the rainbow shows a distinct bump, as seen for Venus in Fig. 1.1a, where the exact angular position depends on the particle size. Moreover, the width of the particle size distribution determines the broadening and contrast of the rainbow polarization signal.

Large particles scatter all colors more evenly than small particles (scattering

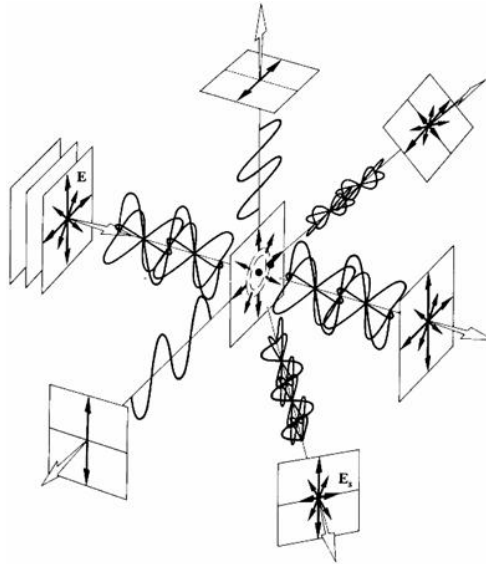


Figure 1.3: Rayleigh scattering of light by air molecules. An unpolarized beam of light is incident from the left, depicted by different electric waves with different oscillation directions. The molecule re-radiates in all directions, albeit only the electric field components that are perpendicular to the direction of scattering. Hence, in the forward direction the scattered light is brightest and unpolarized ($P_L = 0$), whereas at 90° the light is fully polarized ($P_L = 1$) at half the intensity. *Figure from Hecht (2002). HECHT, EUGENE, OPTICS, 4th Edition, © 2002, p.347. Reprinted by permission of Pearson Education, Inc., Upper Saddle River, NJ.*

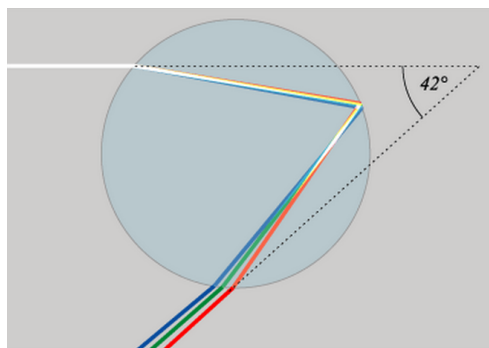


Figure 1.4: The rainbow at a scattering angle of 138° is caused by the refraction of sunlight when entering and exiting a water droplet. It also has a characteristic polarization signal. *Image source: <http://www.neoteo.com>.*

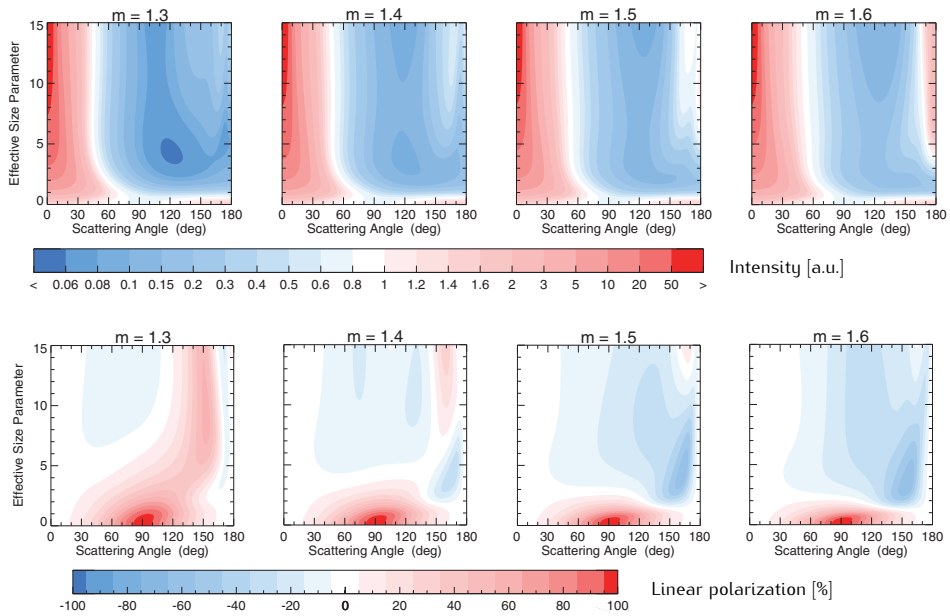


Figure 1.5: Scattered intensity (upper) and degree of polarization (lower) for single scattering of unpolarized incident light, as functions of scattering angle and effective size parameter $x_{\text{eff}} = 2\pi r_{\text{eff}}/\lambda$, for refractive indices m varying from 1.3 to 1.6. The scattering particles are spherical with a Gamma size distribution with an effective radius r_{eff} and variance $v_{\text{eff}} = 0.2 \mu\text{m}$. *Figure adapted from Mishchenko & Travis (1997).*

efficiency scales with $1/\lambda^2$), which is the reason why clouds are white. This also causes a white aureole around the Sun, with a relatively large contribution of scattering by water droplets and aerosols, which decreases rapidly when moving away from the Sun when Rayleigh scattering by small particles takes over. At the small scattering angles close to the Sun, the light is refracted when entering and exiting the particle, which creates polarization in the plane of scattering, according to the Fresnel equations. Note that this is perpendicular to the direction of polarization due to Rayleigh scattering.

Figure 1.5 shows Mie scattering intensity and polarization for different refractive indices and effective size parameters. The latter is a combination of particle size and wavelength, reflecting the fact that measurements at multiple wavelengths provide information about the particle size. The polarization is more sensitive to the aerosol microphysical properties than the scattered intensity, as it shows more variation between the plots (different refractive indices), and more variation along the vertical axis (particle size).

For a formal description of polarization, we consider the electric field in a light

wave traveling in the z -direction through time t , described by:

$$E_x(z, t) = E_{x0} \exp[i(kz - \omega t)] \quad (1.1)$$

$$E_y(z, t) = E_{y0} \exp[i(kz - \omega t + \delta)], \quad (1.2)$$

where k is the wave number, ω is the angular frequency, and δ is the phase delay of the y -component with respect to the x -component. At a fixed position z , the electric field vector traces a Lissajous figure in the $x - y$ -plane over time, which depicts the polarization state of that wave. For example, in the case that $\delta = 0$, the electric field components are in phase, and a linear trace is obtained, i.e., the wave is linearly polarized. For $\delta = \pi$, the electric field components are exactly out of phase, such that again a linear trace is obtained, albeit with its orientation mirrored around the x -axis. In the special case that $E_{x0} = E_{y0}$ and $\delta = \pi/2$, a circular trace is obtained, so the wave is circularly polarized. In general the polarization state of a light wave is elliptical.

This thesis deals with light scattered in the Earth's atmosphere that is the incoherent sum of many light waves with different polarization directions, and is therefore only partially polarized. Hence, the Stokes formalism is used to describe the total intensity I and the intensity and state of the polarized part of the light, according to:

$$\mathbf{S} = \begin{pmatrix} I \\ Q \\ U \\ V \end{pmatrix} = \begin{pmatrix} E_{x0}^2 + E_{y0}^2 \\ E_{x0}^2 - E_{y0}^2 \\ 2 E_{x0} E_{y0} \cos \delta \\ 2 E_{x0} E_{y0} \sin \delta \end{pmatrix} = \begin{pmatrix} \uparrow + \leftrightarrow = \nearrow + \nwarrow = \odot + \ominus \\ \downarrow - \leftrightarrow \\ \nearrow - \nwarrow \\ \odot - \ominus \end{pmatrix}, \quad (1.3)$$

where Q is the difference in intensity between the vertically and the horizontally polarized components, U is the intensity difference between linear polarization at $\pm 45^\circ$, and V is the intensity difference between right- and left-handed circular polarization (Collett 2005).

In the case of light scattering in the Earth's atmosphere, the degree of linear polarization (P_L) can be anything between 0 and almost 1, whereas the degree of circular polarization V/I is on the order of 10^{-4} (Kawata 1978). Therefore, instruments like SPEX are optimized for measuring only intensity and linear polarization. The degree (P_L) and angle (ϕ_L) of linear polarization are related to the Stokes parameters, according to:

$$Q/I = P_L \cos 2\phi_L, \quad (1.4a)$$

$$U/I = P_L \sin 2\phi_L, \quad (1.4b)$$

i.e.:

$$P_L = \sqrt{Q^2 + U^2}/I, \quad (1.5a)$$

$$\phi_L = \arctan 2(U/Q)/2. \quad (1.5b)$$

Optical components that change the polarization state of light are described by a 4×4 Mueller matrix, such that:

$$\mathbf{S}_{\text{out}} = \mathbf{M} \mathbf{S}_{\text{in}}. \quad (1.6)$$

In the context of scattering, this Mueller matrix is called a scattering phase matrix. The general phase matrix for a collection of randomly oriented scattering particles, as a function of scattering angle θ , is of the form:

$$\mathbf{M}_{\text{scat}}(\theta) = \begin{pmatrix} M_{11}(\theta) & M_{12}(\theta) & 0 & 0 \\ M_{12}(\theta) & M_{22}(\theta) & 0 & 0 \\ 0 & 0 & M_{33}(\theta) & M_{34}(\theta) \\ 0 & 0 & -M_{34}(\theta) & M_{44}(\theta) \end{pmatrix}. \quad (1.7)$$

In the case of isotropic, spherical scatterers, $M_{11} = M_{22}$ and $M_{33} = M_{44}$. The upper left block represents the creation of polarization at $\pm Q$, i.e. parallel or perpendicular to the scattering plane, whereas the lower right block describes the conversion of linear polarization at 45° into circular polarization.

Scattering phase matrices are used extensively in radiative transfer algorithms to propagate Stokes vectors through a model atmosphere, to interpret multi-angle multi-wavelength measurements of intensity and polarization in terms of aerosol size, shape, and chemical composition (Dubovik et al. 2006). The model atmosphere is composed of thin plane-parallel layers, each containing a homogenous mixture of air molecules and aerosols, bounded by a diffusely reflecting ground surface. For each layer, the total transmission and reflection properties are calculated, and the layers are subsequently combined while taking into account multiple scattering between different layers, to obtain the intensity and polarization at ground level (Hasekamp & Landgraf 2002, 2005). When fitting the model to SPEX measurements, the free fit parameters are: aerosol optical thickness for large and small mode aerosols, aerosol particle size distribution for both modes, aerosol complex refractive index, aerosol sphericity, and surface albedo. The real part of the refractive index is an indicator for the aerosol chemical composition, as shown for the case of Venus in Fig. 1.1c. The imaginary part describes the amount of absorption by individual aerosols, which is an important parameter for detecting black carbon or soot.

1.5 Atmospheric scattering measurements

Examples of ground-based atmospheric scattering measurements, performed with the groundSPEX instrument described in Chapter 5, are shown in Fig. 1.6. It shows the intensity and degree of linear polarization P_L of the cloud-free sky for three different scattering angles: close to forward scattering, i.e. close to the Sun (10°), close to 90° scattering, and at an intermediate angle. The angles are obtained by pointing the instrument in different directions in the principal plane, which is the vertical plane that goes through the Sun, zenith, and the instrument. This plane provides the largest range of scattering angles, from $0-90^\circ$ if the Sun is at zenith to $0-180^\circ$ if the Sun is at the horizon. The scattered light is horizontally polarized, because of the geometric principle depicted in Fig. 1.3.

The global shape of the intensity spectra is the black-body spectrum of the Sun. On top of this spectrum a large number of spectral features are visible. Many of

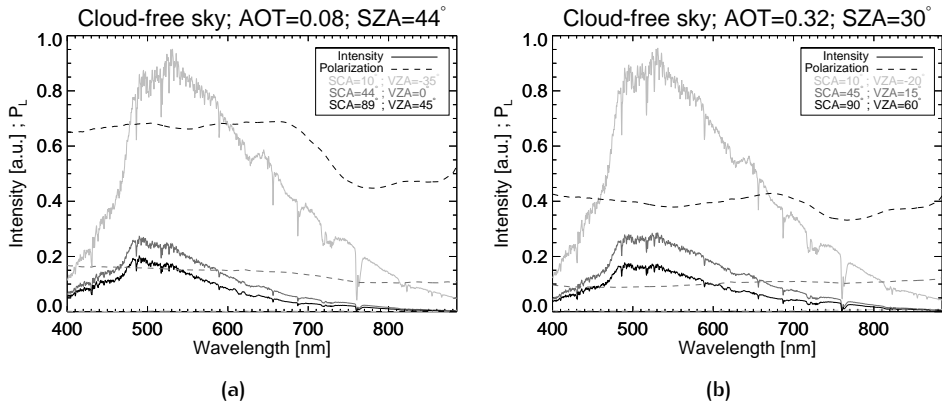


Figure 1.6: Measurements of the intensity and degree of polarization (P_L) of a cloud-free sky, with a small (a) and large (b) aerosol load. The instrument points at three viewing zenith angles (VZA), to create scattering angles (SCA) close to 0, 45 and 90°. The measurements are taken with the groundSPEX instrument at CESAR Observatory, The Netherlands, on July 9, 2013. (a) 8:55 UTC. Solar zenith angle SZA=44°. AOT=0.08 at 550 nm. (b) 11:41 UTC. SZA=30°. AOT=0.32 at 550 nm.

the absorption lines below 600 nm are Fraunhofer lines that originate in the solar atmosphere, whereas the broader absorption bands at longer wavelengths are mainly caused by oxygen and water vapor in the Earth's atmosphere.

When looking away from the Sun, the intensity decreases, and P_L increases, as expected from Fig. 1.3. The intensity decrease is larger at longer wavelengths, which means that the sky gets an increasingly deep blue color when moving away from the Sun. This is the transition from white Mie with strong forward scattering to blue Rayleigh scattering.

The degree of polarization also shows a strong scattering angle dependence: it goes from virtually 0 close to the Sun to 40–70% at 90° scattering. However, the geometrical argument in Fig. 1.3 predicts a P_L of 100% at 90° scattering. The significant depolarization is mainly caused by multiple scattering. If a lightwave gets scattered a second time, the scattering geometry is different, because the first scatterer acts as the light source. This deviating geometry can lead to a different angle of polarization, and hence to depolarization, because it dilutes the main polarization direction due to single scattering. A second depolarizing factor is light that is diffusely reflected by the Earth's surface, before it is scattered in the atmosphere towards the instrument. This surface albedo effect is particularly noticeable when looking close to the horizon, for example for a viewing zenith angle of VZA=45° in Fig. 1.6a. The strong decrease in polarization above 700 nm is due to the strong increase in reflectance of vegetation in the infrared, called the red edge. The small dip at 550 nm is the effect of vegetation reflecting green light, called the green bump. Another

reason why $P_L < 1$ at 90° scattering is the intrinsic depolarization of anisotropic gases, which for the diatomic air molecules leads to a maximum P_L of 0.93 (Hansen & Travis 1974). Finally, thin invisible clouds may be present with increased multiple scattering, leading to depolarization (Pust & Shaw 2008). The maximum polarization in Fig. 1.6b is much lower than in Fig. 1.6a due to the higher AOT and the larger VZA. The latter increases the optical path through the atmosphere and hence the multiple scattering, and the contribution of unpolarized ground reflectance increases closer to the horizon.

1.5.1 Current scattering instrumentation

Several instruments employ passive scattering measurements to determine the atmospheric aerosol load. They all have different numbers of viewing angles and wavelengths, and most of them do not measure polarization, or with very limited accuracy.

The AERONET sunphotometers, for example, also measure scattered light at a large number of viewing angles, typically in four wavelength bands in the visible part of the spectrum. This allows for the retrieval of particle size distribution, and a rudimentary classification of the aerosols using the complex refractive index with an accuracy of 0.04 in the real part and 30% in the imaginary part (Dubovik et al. 2000). A new version of the sunphotometers including polarization measurements at all wavelengths has become available. It has been shown that this instrument indeed improves the retrieval of size distribution and refractive index (Li et al. 2009).

In the end it is crucial to have satellites monitoring and characterizing atmospheric aerosols, because of their large spatial and temporal coverage. Currently, most global aerosol information comes from the MODIS instrument onboard the Aqua and Terra satellites, and MISR onboard Terra, with AOT as their main products. MODIS (Moderate-resolution Imaging Spectroradiometer) employs intensity measurements in 7 wavelength bands within 466–2119 nm for aerosol retrieval, and is viewing in the nadir direction with a cross-track field-of-view of $\pm 55^\circ$ (Salomonson et al. 1989, Remer et al. 2005). The lack of multiple viewing directions limits the retrieval to a number of standard aerosol models. MISR (Multi-angle Imaging SpectroRadiometer) measures intensities in four spectral bands within 446–866 nm, in 9 along-track viewing directions within $\pm 70.5^\circ$, with a cross-track field-of-view of $\pm 14^\circ$ (Diner et al. 1998, Martonchik et al. 1998). These specifications, more similar to AERONET, allow for the retrieval of particle size distribution and complex refractive index. The PARASOL/POLDER instrument, decommissioned in 2013 after 9 years in orbit, combined multi-angle (16 angles within $\pm 43^\circ$) multi-wavelength (443–1020 nm) imaging radiometry with polarimetry in 3 of the 9 spectral bands (Tanré et al. 2011). The additional polarization information, with an accuracy of $\sim 0.01 - 0.02$, greatly improves the retrieval of both macro- and microphysical aerosol properties (Mishchenko & Travis 1997, Hasekamp & Landgraf 2007). Moreover, polarimetry enables the characterization of aerosols near and above clouds, which is crucial for studying the aerosol-cloud interaction (Hasekamp 2010, Knobelspiesse et al. 2011,

Waquet et al. 2013). The ability to retrieve cloud properties along with aerosols also results in much more usable data, because the scene does not have to be strictly cloud-free, and the quality of the aerosol retrieval depends less on the cloud screening and residual cloud contamination, which is particularly interesting in the twilight zone around clouds, the transition region from cloud droplets to dry particles.

To achieve a significant reduction of the uncertainty in climate sensitivity, an understanding of the aerosol radiative forcing at the 0.25 W/m^2 level is required, through detailed and accurate aerosol characterization (Hansen et al. 1995, Schwartz 2004). The corresponding accuracies for macro- and microphysical aerosol properties have been derived (Mishchenko et al. 2004), and translated into measurement requirements (Hasekamp & Landgraf 2007, Hasekamp 2010), showing that sub-percent polarimetric accuracy is the key to success for the next generation multi-angle multi-wavelength polarimeters. As shown in Fig. 1.7, sufficiently accurate retrieval of the important parameters of aerosol optical thickness and real refractive index (indicative of aerosol type and chemical composition) can only be achieved with a polarimetric accuracy of ~ 0.003 . This is an order of magnitude better than the current instrumentation (Tanré et al. 2011), and requires groundbreaking concepts for both the instrument and calibration. This is what we aim for with the development and calibration of the SPEX instrument described in this thesis.

1.6 Measuring polarization

The intensity and linear polarization of light are described by 3 parameters: intensity I , degree of linear polarization P_L , and angle of linear polarization ϕ_L , or equivalently, Stokes I , Q , and U . In fact, the definition of the Stokes parameters in Eq. (3.2) provides direct instructions for measuring them using polarization filters at different angles. For example, Stokes Q is the intensity transmitted through a vertical polarizer minus that through a horizontal polarizer, i.e., $Q = \uparrow - \leftrightarrow$. The sum of the two intensities is the total intensity I , i.e., $I = \uparrow + \leftrightarrow$, and Stokes U is measured using a polarizer at 45° and -45° , according to $U = \nearrow - \nwarrow$. A rotating polarizer is a common way of measuring linear polarization, and is used in Chapter 4 for calibration purposes.

The optics and detector behind the polarizer often exhibit polarization sensitivity, such that rotation of the polarizer creates a spurious polarization signal. Therefore, an alternative approach is to rotate or modulate the polarization in front of a fixed polarizer. The modulation is usually performed using a retarder that induces a phase retardation δ between polarization along its ordinary (o) and extraordinary (e) axis, according to:

$$\delta = \frac{2\pi \Delta n d}{\lambda}, \quad (1.8)$$

where d is the thickness of the retarder, and λ is the wavelength of the light. The birefringence $\Delta n \equiv n_e - n_o$ describes the difference in the retarder's refractive

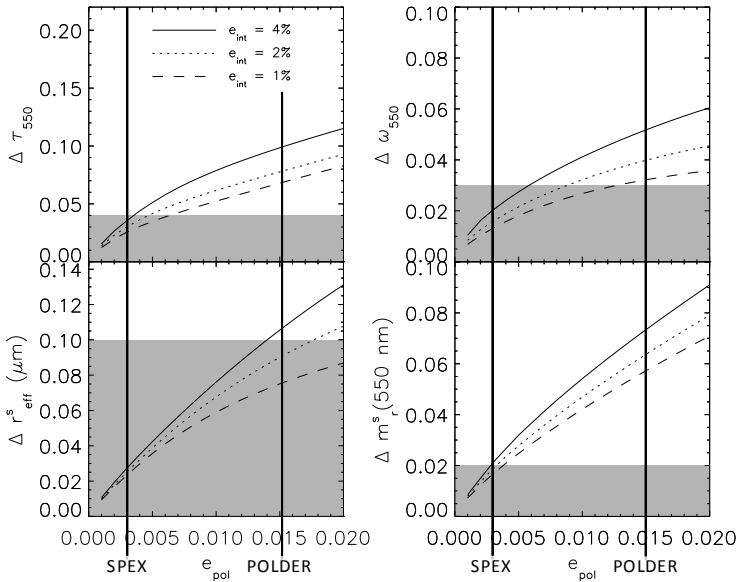


Figure 1.7: Uncertainty in retrieved aerosol parameters as a function of polarimetric accuracy: aerosol optical thickness (upper left), single scattering albedo (upper right), effective radius small mode (lower left), real part of refractive index of small mode (lower right). The shaded areas represent the requirements for climate research (Mishchenko et al. 2004). The vertical lines represent the polarimetric accuracies of PARASOL/POLDER and SPEX. The calculations are performed for radiometric accuracies of 4% (solid line), 2% (dotted line) and 1% (dashed line). The simulated satellite instrument has 17 along-track viewing angles within $\pm 60^\circ$ and 10 spectral bands within 350–2200 nm. *Figure based on simulations by Hasekamp (2010).*

index for o and e polarization, which causes polarization dependent propagation velocities, and hence a phase shift upon exiting. Waveplates, made of birefringent crystals, such as quartz or magnesium fluoride, or stretched polymers, have a fixed birefringence at a fixed orientation. For example, half-wave plates mirror the angle of incoming polarization around their axes by inducing a retardance of $\delta = \pi$, whereas a quarter-wave plate with $\delta = \pi/2$ converts circular into linear polarization and vice versa. In order to modulate the polarization, several options exist to vary the retarder's orientation or its retardance. For example, a rotating half-wave retarder at 0° (vertical) and 45° , in front of a polarizer at 0° , provides a measurement of Stokes Q , whereas rotation angles of 22.5° and -22.5° provide U . The axis of a ferroelectric liquid crystal (FLC) can switch between two orientations by applying an alternating electric field that rotates the long axes of the liquid crystal. In the case of a liquid crystal variable retarder (LCVR), the retardance is tunable by applying an electric field that tilts the long axes of the liquid crystal in the depth direction, thereby reducing the anisotropy between e and o . A photoelastic modulator (PEM) applies an alternating mechanical stress to a glass to induce a varying birefringence.

We showed two intuitive examples of polarization measurements, using a rotating polarizer and a rotating retarder. In general, and more formally, the measured intensity at modulation state i is given by the dot product of the first row of the Mueller matrix of the polarimeter at modulation state i and the Stokes vector under study, as shown in Eqs. (3.2) and (3.5). Hence, a modulation matrix \mathbf{O} can be constructed, consisting of the first rows of the Mueller matrices of the m modulation states, such that the modulation process can be described as:

$$\begin{pmatrix} I_1 \\ I_2 \\ \vdots \\ \vdots \\ I_m \end{pmatrix} = \begin{pmatrix} M_{1(11)} & M_{1(12)} & M_{1(13)} & M_{1(14)} \\ M_{2(11)} & M_{2(12)} & M_{2(13)} & M_{2(14)} \\ \vdots & \vdots & \vdots & \vdots \\ \vdots & \vdots & \vdots & \vdots \\ M_{m(11)} & M_{m(12)} & M_{m(13)} & M_{m(14)} \end{pmatrix} \begin{pmatrix} I \\ Q \\ U \\ V \end{pmatrix}_{\text{in}}, \quad (1.9)$$

i.e.:

$$\mathbf{I} = \mathbf{O}\mathbf{S}. \quad (1.10)$$

The measurements are demodulated afterwards using the demodulation matrix \mathbf{D} , according to:

$$\mathbf{S} = \mathbf{D}\mathbf{I}, \quad (1.11)$$

where \mathbf{D} is the pseudoinverse of \mathbf{O} , i.e.:

$$\mathbf{D} = (\mathbf{O}^T \mathbf{O})^{-1} \mathbf{O}^T. \quad (1.12)$$

It follows from Eq. (1.11) that the propagation of measurement noise to the Stokes parameters is determined by the magnitudes of the demodulation matrix elements. This leads to the definition of the polarimetric efficiency for the i th Stokes parameter, according to (del Toro Iniesta & Collados 2000):

$$\epsilon_i = \left(m \sum_{j=1}^m D_{ij}^2 \right)^{-1/2}, \quad (1.13)$$

which is an important metric in polarimeter design. Maximization of polarimetric efficiency is equivalent to the maximization of the modulation amplitudes for the different Stokes parameters.

Remote aerosol characterization requires only linear polarimetry, i.e. the measurement of I , Q and U . This can be achieved using a linear polarization filter (polarizer) at different orientations. The Mueller matrix of a polarizer at 0° is given by:

$$\mathbf{M}_{\text{pol}} = \frac{1}{2} \begin{pmatrix} 1 & 1 & 0 & 0 \\ 1 & 1 & 0 & 0 \\ 0 & 0 & 0 & 0 \\ 0 & 0 & 0 & 0 \end{pmatrix}, \quad (1.14)$$

and it can be rotated over an angle ϕ around the optical axis according to:

$$\mathbf{M}(\phi) = \mathbf{R}(-\phi) \mathbf{M} \mathbf{R}(\phi) ; \mathbf{R}(\phi) = \begin{pmatrix} 1 & 0 & 0 & 0 \\ 0 & \cos 2\phi & \sin 2\phi & 0 \\ 0 & -\sin 2\phi & \cos 2\phi & 0 \\ 0 & 0 & 0 & 1 \end{pmatrix}. \quad (1.15)$$

Hence, the modulation and demodulation matrix corresponding to a polarizer at 0° and 90° , and 45° and -45° , are given by:

$$\mathbf{O} = \frac{1}{2} \begin{pmatrix} 1 & 1 & 0 & 0 \\ 1 & -1 & 0 & 0 \\ 1 & 0 & 1 & 0 \\ 1 & 0 & -1 & 0 \end{pmatrix} ; \mathbf{D} = \frac{1}{4} \begin{pmatrix} 1 & 1 & 1 & 1 \\ 2 & -2 & 0 & 0 \\ 0 & 0 & 2 & -2 \\ 0 & 0 & 0 & 0 \end{pmatrix}. \quad (1.16)$$

The practical implementations for modulating polarization can be very different, each having their advantages and disadvantages. This is reflected in the various measurement concepts that are currently in development for remote aerosol characterization. One of the main design choices is the dimension or domain in which the modulation is performed:

- *Temporal modulation.* The recently decommissioned POLDER instrument employs a rotating filter wheel with polarizers at 0 , 60 and 120° to create the different modulation states sequentially. Misregistration between successive images, due to satellite motion during the ~ 0.6 s modulation cycle, directly translates into polarization errors. The main image shift is compensated using wedged prisms in the polarizer assembly (Hagolle et al. 1999), leaving a polarimetric accuracy of 1% over the ocean to 2% over land, depending on spatial gradients. The 3MI instrument, currently under development by CNES for the MetOp (Meteorological Operational satellite) Second Generation programme of ESA and EUMETSAT, is based on the POLDER concept.

NASA supports the development and comparison of three polarimeter concepts for its future ACE (Aerosol-Cloud-Ecosystem) mission: MSPI, APS and PACS. The MSPI instrument employs temporal modulation at 25 Hz, using photoelastic modulators with a rapidly oscillating retardance. At this frequency, satellite motion is not an issue, but strict synchronization between the retarder and detector is required to avoid mixing of modulation states. A polarimetric uncertainty of < 0.003 has been demonstrated in the lab (Diner et al. 2010).

- *Spatial modulation.* The APS instrument, that failed to reach orbit in 2011, employs pairs of identical telescopes with polarizers rotated by 45° to simultaneously measure Stokes Q and U . Since each modulation state uses an independent optical path and detector, polarimetric errors may arise from differences in transmission and detector gain. APS uses single-pixel detectors in combination with an along-track scanning mirror for multi-angle observations, which allows for the use of an in-flight polarization calibration unit. The polarimetric accuracy of APS is < 0.002 (Cairns et al. 2003).

PACS is a wide-field 2D imager, using a three-way polarizing beamsplitter to image polarization at 0, 60, and 120° (optimal for linear polarimetry) onto three independent focal planes. Preliminary calibration results show a polarimetric accuracy of ~ 0.005 (Buczowski et al. 2013).

- *Spectral modulation.* SPEX, the instrument described in this thesis, employs a static birefringent crystal and a spectrograph to encode the degree and angle of linear polarization as the amplitude and phase of a sinusoidal modulation pattern in the intensity spectrum. This provides the full spectral intensity and linear polarization information in a single shot, without moving or active modulation optics (Snik et al. 2009). The most basic implementation of spectral modulation is susceptible to aliasing between the spectrally modulated polarization and features in the incoming intensity spectrum with similar spectral widths, such as absorption bands. The polarimetric accuracy of SPEX is $\sim 0.001 + 0.005 \cdot P_L$, as demonstrated in Chapter 4.

The most sensitive astronomical polarimeters combine temporal and spatial modulation to eliminate their intrinsic errors to first order, a technique called beam-exchange polarimetry or spatio-temporal modulation (Semel et al. 1993, Bagnulo et al. 2009). For example, a rotating half-wave retarder in front of a polarizing beam-splitter rotates the incoming polarization, such that each polarization direction is measured twice: first the polarization is transmitted in beam *A* and blocked in beam *B*, while in the second measurement the beams are exchanged. SPEX uses a spatio-spectral version of beam-exchange polarimetry, where the two measurements are not separated in time, but shifted in wavelength, providing the same redundancy that eliminates intrinsic modulation errors, but in a snapshot fashion (see Chapter 6).

1.7 Polarimeter performance and calibration

Besides the modulation-specific errors, accurate polarimetry is hampered by a variety of static and dynamic errors. Typical error sources inside a polarimeter are: instrumental polarization due to differential transmission or absorption, depolarization due to scattering, and crosstalk between different Stokes parameters due to, e.g., misalignment or stress birefringence (Keller 2002). These errors may have a dynamic component, e.g. due to temperature sensitivity. Moreover, intrinsically random errors are present, such as detector noise or in-flight contamination of the first optical surface. The static errors are often much larger than the dynamic errors, but after careful calibration the dynamic errors may dominate; imperfect calibration leaves residual static errors.

Each optical element in the polarimeter typically has several effects on the polarization, each described by a 4×4 Mueller matrix. Hence, it is almost impossible to intuitively understand how polarization propagates through even the simplest setups. An approximated method to make a Mueller matrix model of a polarimeter more manageable is obtained by linearization with respect to the independent physical

parameters (de Juan Ovelar et al. 2011, Snik & Keller 2013). The approach in this thesis for the error analysis of SPEX is the construction of a full Mueller matrix model, followed by a realistic model of the polarimetric calibration. Monte Carlo simulations on this end-to-end model, using realistic values for all error sources, predict the complete polarimetric performance.

The purpose of polarimetric calibration is to find the modulation matrix that relates measured intensities to the incoming Stokes vector, according to Eq. (1.10). By applying different known polarization states \mathbf{S} using a calibration stimulus, and measuring the corresponding intensities \mathbf{I} , one can solve for the modulation matrix \mathbf{O} . However, due to errors in the calibration measurements, and instrument changes after calibration, the modulation matrix and hence the applied demodulation matrix are not perfect. Therefore, a measured Stokes vector \mathbf{S}' differs from the true input \mathbf{S} , according to:

$$\mathbf{S}' = \mathbf{X} \mathbf{S}, \quad (1.17)$$

where \mathbf{X} is the 4×4 response matrix (Ichimoto et al. 2007).

The main performance parameters of a calibrated polarimeter are its polarimetric accuracy and sensitivity. The accuracy is the difference between the measured and the true Stokes vectors, according to:

$$\mathbf{S}' - \mathbf{S} = (\mathbf{X} - \mathbf{I}_4) \mathbf{S} \equiv \Delta \mathbf{X} \mathbf{S}, \quad (1.18)$$

where \mathbf{I}_4 is the 4×4 identity matrix. In other words, a complete description of accuracy is a 4×4 matrix $\Delta \mathbf{X}$ that describes the deviation from unity of the response matrix. Polarimetric sensitivity describes the smallest measurable (change in) polarization, which is ultimately limited by detection noise, and obviously sets a lower limit to the polarimetric accuracy.

1.8 Brief history of SPEX

Even though SPEX, the Spectropolarimeter for Planetary EXploration, is currently focussing on the characterization of aerosols in the Earth's atmosphere, the instrument was originally designed in 2007 for studying massive dust storms on Mars onboard the ExoMars Trace Gas Orbiter (Snik et al. 2008). A functional prototype was developed in 2008–2010 by a Dutch consortium of academia and industry², according to the specifications in Table 1.1. Several calibration campaigns were executed with the Mars prototype in the years following 2010, including the calibration of polarimetric sensitivity and accuracy as presented in this thesis. In the meantime, a design study was performed for the Europa Jupiter System Mission, later called Jupiter Icy Moon Explorer, to fly SPEX in orbit around Jupiter to study clouds and haze particles, and Jupiter's moons Europa and Ganymede to study the

²The SPEX functional prototype for Mars is constructed by a Dutch consortium consisting of SRON Netherlands Institute for Space Research, Leiden University, NOVA-ASTRON, TNO, Mecon, cosine, and Dutch Space.

Instrument parameter	Mars	Earth
Observables	I and P_L	I and P_L
Wavelength range	400–800 nm	400–800 nm minimum 400–1600 nm goal
Polarization accuracy	$0.01 + 0.05 \cdot P_L$	$0.001 + 0.005 \cdot P_L$
Radiometric accuracy	–	2%
Spectral resolution P_L	20 nm	20 nm
Spectral resolution I	2 nm	1.5 nm
# viewing angles	9	30
Cross-track field-of-view	7°	30°
Ground pixel size	$1^\circ \times 1^\circ$ 14 km \times 14 km	$0.42^\circ \times 0.42^\circ$ 2.5 km \times 2.5 km

Table 1.1: Typical specifications for a SPEX instrument for in-orbit characterization of the atmospheres of Mars and Earth.

composition and roughness of their icy surfaces. Radiation tests simulating Jupiter’s strong radiation belts were successfully executed.

Soon it became clear that the performance of the prototype instrument exceeds the requirements for Mars, and SPEX was considered a good candidate for the more stringent requirements for Earth observation (see Table 1.1). Earth observation is more demanding, because it requires the simultaneous retrieval of a large variety of aerosols, clouds, and the highly variable surface albedo. The more stringent polarimetric accuracy requirement is driven by the ability to discriminate between different aerosol types via the refractive index (see Fig. 1.7). The large amount of viewing angles is needed to sample the scattering phase matrix at the rainbow angles for detection of clouds and determination of the cloud droplet size distribution. This enables the characterization of aerosols near clouds, and reduces cloud contamination in the retrieved aerosol parameters. The increased cross-track field-of-view provides context around clouds and aerosol sources, and improves the spatial coverage. An additional short-wave infrared channel improves the characterization of coarse mode aerosols.

1.9 Thesis outline

Chapter 2 describes the SPEX instrument’s optical and mechanical design, and the realized prototype. Fundamental calibrations and data reduction steps are described that are necessary to convert raw detector images into intensity and polarization spectra. In particular, the spectral polarimetric efficiency and its dependency on the polarization angle is determined using a rotating polarizer, and interpreted. We establish the $2 \cdot 10^{-4}$ sensitivity of the polarimetric response of the SPEX prototype by supplying partially polarized light with slowly increasing degree of linear polarization, using an increasingly tilted glass plate in front of a light source. Although the absolute degree of polarization of this stimulus is not calibrated, fits to a Fresnel model leave residuals of < 0.006 , which is already better than the required accuracy

for Mars of $0.01 + 0.05 \cdot P_L$. We perform on-sky verification measurements, and provide a qualitative interpretation. Moreover, the on-sky data led to various improvements in the hardware and data reduction pipeline.

Chapter 3 presents a comprehensive theoretical error analysis for spectrally modulated polarimetry as implemented in SPEX. Various error sources are identified, and classified according to their effect after calibration: static errors, such as misalignments, decrease the measurement efficiency but do not impact the P_L measurement after calibration, whereas dynamic errors, e.g. due to temperature variations, directly influence the measured P_L . Relevant dynamic effects for SPEX are in-flight contamination of the first optical surface, temperature-induced variations in the multiple-order retardance, and spectrograph defocus due to thermal expansion, which directly changes the spectral modulation contrast on the detector, but the polarimetric performance is limited by shot noise. We present an end-to-end model of an in-orbit SPEX instrument, including static and dynamic errors and a realistic on-ground calibration. We employ this model for Monte Carlo simulations of the in-flight performance, showing that the probability of measuring the degree of linear polarization with an error within ± 0.001 (± 0.002) is 76% (99%) without in-flight calibration.

The results in Chapters 2 and 3 demonstrate the potential for reaching the required polarimetric accuracy of $0.01 + 0.05 \cdot P_L$ with the SPEX prototype for Mars, and even the $0.001 + 0.005 \cdot P_L$ for Earth observation. The goal in **Chapter 4** is the experimental verification of the polarimetric accuracy of the SPEX prototype at the challenging level of 10^{-3} . The full data reduction pipeline of SPEX is presented first, and examples are shown of the demodulation of a fully and a partially polarized measurement. We subsequently present the constructed polarization calibration stimulus: a carefully depolarized light source followed by two tiltable glass plates to provide white calibration light to SPEX with a degree of linear polarization of $0 \lesssim P_L \lesssim 0.5$ at an accuracy of $0.001 + 0.005 \cdot P_L$. This accuracy cannot be guaranteed by design over the entire P_L -range due to uncertainties in the polarization properties of the glass plates and their coatings. Therefore, a dual-beam rotating analyzer verification polarimeter is constructed, and calibrated using both fully polarized light and the unpolarized output of the calibration stimulus, showing a verification accuracy of $4 \cdot 10^{-4}$. The stimulus zero-point is $\sim 10^{-4}$ by design, which is confirmed with SPEX in a direct P_L measurement, as well as an indirect, P_L -independent method based on the measured rate of change of the angle of linear polarization at small P_L . The resulting difference between SPEX and the verification polarimeter is smaller than $0.001 + 0.01 \cdot P_L$ across the calibrated range of $0 \lesssim P_L \lesssim 0.5$. However, after correction for a reproducible, systematic deviation, the difference between the polarimeters is smaller than $0.001 + 0.005 \cdot P_L$. The polarimetric accuracy of SPEX is suitable for the characterization of aerosols in the Earth's atmosphere. My contribution to this chapter is the design, construction and verification of the calibration stimulus.

Once the excellent polarimetric performance results of the SPEX prototype started trickling in, the Netherlands National Institute for Public Health and the Environment (RIVM) expressed its interest in the development of a ground-based SPEX instrument to investigate future air-quality monitoring networks. **Chapter 5** presents the groundSPEX instrument that we developed, a low-cost, weatherproof SPEX instrument on a motorized altazimuth mount for autonomous spectropolarimetric sky measurements. We analyze the random and systematic errors in the radiometry and polarimetry, and their propagation to the retrieved aerosol parameters. We present the results of the four-day field-commissioning, in terms of AOT, particle size, and refractive index, which are consistent with the co-located AERONET station. GroundSPEX is handed over to RIVM, which is commissioning it for permanent operation.

In Chapters 2–5 we have shown that the SPEX concept is suitable for high-accuracy polarimetry at a spectral resolution of ~ 20 nm, which is crucial for remote aerosol characterization. **Chapter 6** introduces new functionalities enabled by the unique and powerful combination of a spectrograph and dual-beam spectrally modulated polarimetry. We make use of the fact that the sum of the orthogonally modulated spectra is the unmodulated intensity spectrum at the spectrograph’s intrinsic resolution. This prevents aliasing between the modulation pattern and spectral features in the incoming intensity spectrum, and hence greatly improves the accuracy of both the radiometry and polarimetry. We show how differential transmission between the opposite spectra leads to residual modulation in the sum-spectrum, and provide an iterative algorithm for post-facto extraction and correction of the differential transmission from the measured spectra. This dynamic transmission correction reduces the associated polarimetric error by orders of magnitude, and enhances the instrument’s long-term in-flight stability. We prove that the redundancy in the spatio-spectral modulation reduces the sensitivity to uncorrected dark signal and transmission or gain changes by orders of magnitude with respect to a beam-splitting-only polarimeter. We demonstrate the ability of measuring polarization at the spectrograph’s intrinsic resolution of ~ 1 nm. We measure the spectral polarization of the clear sky using the groundSPEX instrument, showing $P_L = 0.160 \pm 0.010$ in the Oxygen A absorption band, compared to $P_L = 0.2284 \pm 0.0004$ in the continuum. This high-resolution absorption band polarimetry, unique amongst the various concepts for high-accuracy polarimetry for satellite-based atmospheric aerosol characterization, provides crucial information on the aerosol vertical stratification.

1.10 Outlook

The work in this thesis shows that we achieved all polarimetric requirements with the SPEX prototype instrument, and presents a comprehensive theoretical error analysis showing its long-term stability. Moreover, we demonstrate our end-to-end ability to remotely characterize aerosols in the Earth’s atmosphere.

The next step for SPEX is the application on a high-altitude airplane, which will be carried out by SRON. This provides the most realistic testbed for studying and developing the retrieval of aerosols near clouds, the impact of variable surface albedo, instrument stability in a high-altitude environment, and co-registration, including the effects of the moving platform and the viewing-angle dependency of the ground-pixel size. Moreover, an airborne campaign will provide the first downward-looking science data with SPEX, including measurements of the Oxygen A absorption band. Such a field campaign will fly over aerosol instrumentation at ground level, including lidars, and perhaps features an onboard lidar, providing aerosol vertical profiles that will be used to study the information content in SPEX' absorption band polarimetry. In-flight comparison with other high-accuracy polarimeters, such as NASA's MSPI, PACS, and RSP (airborne prototype of APS), is crucial for understanding their and SPEX' true accuracy, since we are all at the forefront of polarimetric remote sensing, and the instrument concepts are all very different. At this moment all nine viewing apertures of the SPEX prototype instrument are being equipped with polarization optics in preparation for flight campaigns starting in 2015. The polarization calibration stimulus will be further improved to calibrate all viewing apertures with an accuracy of $0.001 + 0.005 \cdot P_L$.

A future SPEX satellite instrument for Earth observations requires a redesign with a larger number of viewing angles (~ 30) and a larger swath ($\sim 30^\circ$), but with identical polarimetry. In this thesis we show that such an extended version of the Mars prototype, including enhanced thermal compensation of the spectrograph, in combination with the athermal multiple-order retarder, the dynamic transmission correction, and the low polarimetric susceptibility to in-flight surface contamination, opens the way to high-accuracy polarimetry without in-flight calibration. SPEX' technological breakthrough enables the crucial remote characterization of aerosol microphysical properties in the Earth's atmosphere.

The work in this thesis is also a contribution to the development of the field of polarimetry at a more abstract level. Most polarimeter designs are still based on simple principles that can be understood intuitively, such as the rotating half-wave retarder. Other polarimeters are used in a non-optimum way, such that the information content in the measurements is not maximized, or the information is not recognized and is lost in the data reduction (del Toro Iniesta & Collados 2000). The use of generalized mathematical formalisms is emerging, enabling more generalized design approaches to maximize the information content and minimize the susceptibility to measurement errors (del Toro Iniesta & Collados 2000, Alenin & Tyo 2014). Error analyses are often limited to random Gaussian measurement noise; only a few attempts have been made to include systematic errors, and the effects of imperfect polarimetric calibration and data reduction (e.g. Tyo 2002, de Juan Ovelar et al. 2011, Mahler et al. 2011a).

The abstraction of the concept of modulation, and the deeper understanding of the properties of the different modulation domains and combinations thereof, starts to result in more exotic polarimeter concepts. For example, the SPEX concept is

only a member of a whole family of channeled polarimeters, including channeled imaging polarimetry with the modulation ripples in the image, and a version with the modulation partly in the spatial and partly in the spectral domain (Kudenov & Goldstein 2011, Sparks et al. 2012). The combination of modulation domains, such as spatio-temporal and spatio-spectral modulation is shown to improve the polarimetric performance significantly. It is worth investigating the addition of a modulation domain to existing polarimeters. For example, all it takes to add spectral modulation to any existing spectropolarimeter is the insertion of two static birefringent crystals with a thickness in the order of a millimeter.

Another interesting development is polychromatic modulation for spectropolarimetry over extremely large spectral ranges (Tomczyk et al. 2010). The polarimetric efficiency of a modulator often decays when moving away from the central wavelength, due to the wavelength dependence of the modulating retarder (see Eq.(1.8)). The classical approach to increase the spectral coverage is the combination of different crystals to enhance the achromaticity of the modulating element. Polychromatic modulation, however, aims at maximizing the polarimetric efficiency at each wavelength, without the achromaticity constraint. This enables polarimetry over unprecedented spectral ranges, such as the 300–2500 nm rotating retarder modulator that we are developing for the X-shooter spectrograph on the Very Large Telescope (VLT) (Snik et al. 2012). Moreover, the spectrally varying modulation due to the polychromatic optimization even allows for an additional spectral demodulation. Another polychromatic modulator is currently being implemented in the Extreme Polarimeter (ExPo) in Leiden: an integral-field unit enables simultaneous full-Stokes imaging polarimetry and spectropolarimetry over 450–900 nm of circumstellar environments, where the fast modulation is performed using a combination of two FLCs and two fixed waveplates (Rodenhuis et al. 2014). The current out-of-the-box mentality towards polarization modulation will lead to many more examples of versatile and accurate polarimeters in the near future.

Chapter 2

Prototyping for the Spectropolarimeter for Planetary EXploration (SPEX): calibration and sky measurements

We present the Spectropolarimeter for Planetary EXploration (SPEX), a high-accuracy linear spectropolarimeter measuring from 400 to 800 nm (with 2 nm intensity resolution), that is compact (~ 1 liter), robust and lightweight. This is achieved by employing the unconventional spectral polarization modulation technique, optimized for linear polarimetry. The polarization modulator consists of an achromatic quarter-wave retarder and a multiple-order retarder, followed by a polarizing beamsplitter, such that the incoming polarization state is encoded as a sinusoidal modulation in the intensity spectrum, where the amplitude scales with the degree of linear polarization, and the phase is determined by the angle of linear polarization. An optimized combination of birefringent crystals creates an athermal multiple-order retarder, with a uniform retardance across the field of view. Based on these specifications, SPEX is an ideal, passive remote sensing instrument for characterizing planetary atmospheres from an orbiting, air-borne or ground-based platform. By measuring the intensity and polarization spectra of sunlight that is scattered in the planetary atmosphere as a function of the single scattering angle, aerosol microphysical properties (size, shape, composition), vertical distribution and optical thickness can be derived. Such information is essential to fully understand the climate of a planet. A functional SPEX prototype has been developed and calibrated, showing excellent agreement with end-to-end performance simulations. Calibration tests show that the precision of the polarization measurements is at least $2 \cdot 10^{-4}$. We performed multi-

angle spectropolarimetric measurements of the Earth's atmosphere from the ground in conjunction with one of AERONET's sun photometers. Several applications exist for SPEX throughout the solar system, a.o. in orbit around Mars, Jupiter and the Earth, and SPEX can also be part of a ground-based aerosol monitoring network.

Van Harten, Snik, Rietjens et al. *Proceedings of SPIE*, **8160**, 81600Z (2011)

2.1 Introduction

Atmospheric aerosol research is gaining more and more attention, mainly because of climate models showing their large impact on the Earth's climate, whereas the actual aerosol input for the models is poorly known (IPCC 2007). Aerosols, 0.2–200 μm sized particles suspended in the atmosphere, such as tiny water droplets, sand and sea salt, have a direct effect on the climate by absorbing and reflecting incoming sunlight, thereby cooling our planet. Moreover, some types of aerosols act as cloud condensation nuclei, with an increase of such aerosol leading to clouds containing more and smaller water droplets. Since small droplets yield less efficient precipitation, they increase the lifetime of clouds, and hence influence the effects of clouds on the climate. The direct and indirect climate effects of aerosol particles are shown to be extremely sensitive to the aerosol microphysical properties, such as size, shape and chemical composition, and to their concentration and spatial distribution. Hence, accurate aerosol characterization is necessary for a thorough understanding of our climate, and it may ultimately give us a mechanism for climate control, by regulating the anthropogenic aerosol contribution, such as combustion soot and smoke, but also artificial nanoparticles. Clearly, continuous monitoring of atmospheric aerosol on small spatial and time scales is important because of their immediate and local effects on, e.g., air quality and health. Moreover, a monitoring system can minimize the direct economical impact of, e.g., volcanic ash clouds, hampering air traffic.

By studying different planetary atmospheres, such as Mars, Jupiter, Saturn and Venus, each having a completely different climate, we deepen our knowledge about climate systems in general. In addition, it allows for studying individual phenomena, such as the extreme dust storms on Mars, thereby giving insight into elements of our own climate, which cannot be studied separately in the Earth's complex atmosphere.

Obviously, remote sensing is the way to obtain the required coverage, either from an airborne platform (e.g. from a satellite, balloon or airplane(s)), or from a ground-based network. By measuring the spectral intensity and linear polarization of sunlight, scattered at different angles by a patch of atmosphere, and by fitting this to radiative transfer calculations, the micro- and macrophysical aerosol properties can be determined unambiguously (Hasekamp & Landgraf 2007, Mishchenko & Travis 1997). This powerful technique has already been used in several missions, such as Pioneers 10, 11 and Venus, Voyagers 1 and 2, Galileo, and in various Earth observing missions using the POLDER polarimeter. So far, polarimetry has only been performed using either temporal or spatial polarization modulation, which have their intrinsic problems (see Snik & Keller 2013). Temporal modulation implies the measurement of the input polarization by applying different modulation states sequentially. However, during a sequence, the polarimeter is looking at different scenes due to the movement of the platform, thereby inducing spurious polarization signals. For spatial modulation, the beam is split up, such that different modulation states can be measured simultaneously. The difference in the beams' optical paths again induces spurious polarization.

We present SPEX (Spectropolarimeter for Planetary EXploration), which employs

a novel spectral polarization modulation technique, providing high-accuracy linear spectropolarimetry at moderate spectral resolution throughout the visible, at the same time being fully passive, compact, robust and lightweight. The instrument principle is explained in Section 2.2. A functional prototype has been developed, which design is shown in Section 2.3. The first results obtained with this prototype are presented in Section 2.4, viz. several calibration results, as well as ground-based measurements of aerosols in the Earth's atmosphere. Section 2.5 describes the future perspective of SPEX, including the current efforts being taken to be ready for missions to Mars and Jupiter, as well as for Earth observation from space and from the ground.

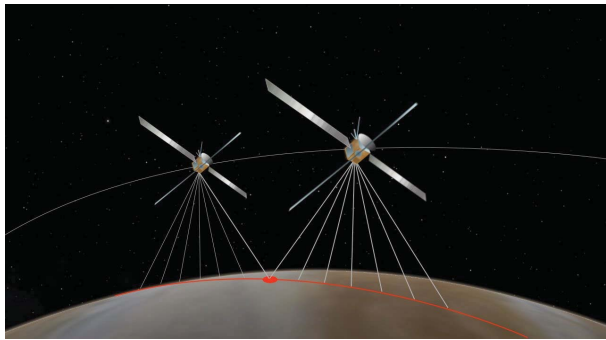


Figure 2.1: SPEX onboard a satellite measures the intensity and linear polarization of sunlight scattered in a planetary atmosphere, for 9 ground pixels along the track simultaneously. While flying over the planet, each ground pixel has eventually been observed at 9 different scattering angles. Combined with the moderate spectral resolution throughout the visible, the parameter space is sufficiently sampled to reveal the micro- and macrophysical properties of the atmospheric aerosol, by interpreting the measurements with radiative transfer calculations.

2.2 SPEX instrument principle

SPEX is a fully passive high-accuracy linear spectropolarimeter with moderate spectral resolution throughout the visible, that is compact (~ 1 liter), robust and lightweight. This is achieved by employing the unconventional spectral polarization modulation technique, also known as channeled spectropolarimetry, optimized for linear polarimetry (see Snik et al. 2009). The polarization modulator consists of an achromatic quarter-wave retarder and a multiple-order retarder, followed by a polarizing beamsplitter, such that the incoming polarization state is encoded as a sinusoidal modulation in the intensity spectrum, where the amplitude scales with the degree of linear polarization (DoLP), and the phase determines the angle of linear polarization (AoLP) (see Fig. 2.2). It can be shown that the modulated spectrum, as a function of the incoming intensity spectrum $I_0(\lambda)$, the incoming linear polarization

DoLP(λ) and AoLP(λ), and the waveplate retardance $\delta(\lambda, T)$, can be written as

$$I_{\pm}(\lambda) = \frac{1}{2} I_0(\lambda) \left[1 \pm \text{DoLP}(\lambda) \cos \left(\frac{2\pi \delta(\lambda, T)}{\lambda} + 2 \text{AoLP}(\lambda) \right) \right], \quad (2.1)$$

where the \pm sign corresponds to the analyzer being parallel or perpendicular to the quarter-wave retarder.

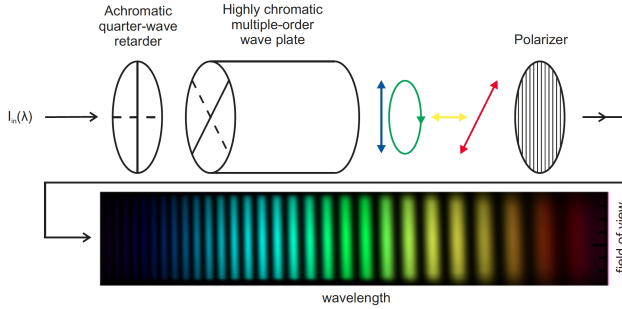


Figure 2.2: The SPEX principle, viz. the spectral modulation of linear polarization. The colored arrows after the highly chromatic multiple-order waveplate denote the strongly wavelength dependent polarization modulation. Analyzing this polarization leads to a characteristic intensity spectrum, containing the linear polarization information, according to equation (2.1).

A demodulation algorithm determines for every wavelength the local modulation amplitude (DoLP(λ)) and phase (AoLP(λ)), as well as the unmodulated intensity ($I_0(\lambda)$), resulting in a spectral resolution of roughly a factor 10 worse than the sampling resolution. This is the price we have to pay for using spectral modulation, however, as long as the linear polarization varies slowly across the spectrum, which applies for scattering polarization, these data products can be achieved very accurately and with sufficient spectral resolution for aerosol characterization. Note that the period of the modulation is constant in the inverse wavelength domain, so for shorter wavelengths the modulations are faster and the spectral resolution is higher.

In case the analyzer is implemented as a polarizing beam splitter, both $I_+(\lambda)$ and $I_-(\lambda)$ are measured, and the sum of these spectra yields the unmodulated intensity spectrum at full spectral resolution. The issue of differential transmission can be circumvented by realizing that the normalized modulations, i.e. I_{\pm}/I_0 , should be centered around 1/2. Systematic deviations from this value reveal the differential transmission, according:

$$\frac{T_+}{T_-}(\lambda) = \left\langle \frac{I_-}{I_+ + I_-} \right\rangle^{-1}(\lambda) - 1, \quad (2.2)$$

where the operator $\langle \rangle$ means spectral averaging of the argument, such that the modulation is eliminated. This way, differential transmission is deduced from the measured spectra themselves, in addition to separate calibration measurements.

The T in equation (2.1) denotes the strong temperature dependence of the multiple-order retarder. The equation shows that temperature changes directly translate into apparent changes in the AoLP. In order to keep the instrument passive and energy efficient, temperature control is avoided, using the following solution: the retarder consists of two plates with opposite temperature effects. Measurements published in reference Snik et al. (2010) show that a subtractive combination of MgF_2 and Al_2O_3 (i.e. with their fast axes crossed), with a thickness ratio of 2.4 : 1, yields optimum performance over the wavelength range 350–800 nm. The residual temperature effect is less than $1.5 \cdot 10^{-2}$ rad/ $^\circ\text{C}$, and can be corrected during data reduction if the temperature is known, or the other way around, the actual temperature can be deduced if the incoming AoLP is known, which is the case for scattering polarization. Note that our main observable, the DoLP, is (to first order) insensitive to changes in the multiple-order retardance, e.g. due to temperature changes.

Although the SPEX principle is generic, the instrument can be optimized for specific applications. For example, different planets can have maximum atmospheric information in different wavelength ranges, and can require different spectral or spatial resolutions and coverage. Moreover, orbit specifications differ from mission to mission. SPEX has been submitted as scientific payload instrument for the Mars Trace Gas Mission orbiter, as part of the former ESA-NASA ExoMars Programme. At 300–500 km altitude, it would characterize airborne dust and soil, as well as ice clouds high in the atmosphere Stam et al. (2008). The corresponding specifications of SPEX are shown in Table 2.1, which also forms the baseline of the constructed prototype, as presented in the next sections.

spectropolarimeter volume	~ 1 l
mass including electronics	~ 2 kg
maximum power consumption	~ 2 W
spectral range	400–800 nm
spectral resolution for polarization	20 nm
spectral resolution for intensity	2 nm
viewing directions	9 along the track: $0, \pm 14, \pm 28, \pm 42, \pm 56^\circ$
field of view for each viewing direction	$1^\circ \times 7^\circ$ (cross-flight, to deal with planet's rotation)
pupil size for each viewing direction	~ 1.1 mm ²
measured polarization properties	Stokes I, Q & U
polarization sensitivity	0.005 (degree of linear polarization)
relative polarization accuracy	5% (down to 0.01 absolute)

Table 2.1: Typical specifications for SPEX onboard the Mars Trace Gas Mission orbiter. From Snik et al. (2010).

2.3 Prototype design

2.3.1 Optical design

The optical system described below can be divided into two main parts; the pre-slit optics (which includes the polarimeters), and the spectrometer optics. Nine fields of view, of which each individual field is split according to two orthogonal polarization states, should be imaged within the sides of the 12.5×12.5 mm, 512×512 pixels detector. For the SPEX prototype, only 3 fingers are filled with polarization optics. This section is largely based on the work in (Snik et al. 2010).

Pre-slit optics

The incoming beam, which has a diameter of 1.1 mm, will first pass the polarization optics to ensure zero instrumental polarization: a BK7C18 Fresnel rhomb for the achromatic quarter-wave retarder, an athermal combination of 1.22 mm sapphire and 2.88 mm MgF_2 for the thick retarder and an α BBO Wollaston prism for the polarizing beam-splitter, see Fig. 2.3b. All optical components are non-moving. In the baseline design, only one single lenslet ($F = 10$ mm) focuses the two polarized beams on two separated slits (1.4×0.2 mm). The advantage of this solution is that only nine relatively large lenses can be used (although still being just 4 mm in diameter), relaxing the manufacturing tolerances as compared to a solution using 18 smaller lenslets (one for each field and polarization state). The dispersion within the Wollaston prism is largely compensated by the dispersion caused by the off-axis light path through the lenslets.

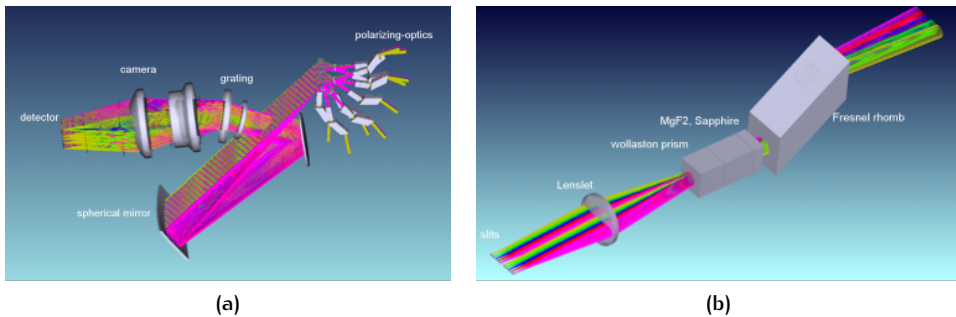


Figure 2.3: (a) Optical design for SPEX. Light enters the 9 fingers with polarization optics on the upper right, is directed to the slit plane via 9 mirrors (not shown), then goes through the spectrograph optics, onto the detector. For the prototype, only 3 fingers are filled with polarization optics, and the detector is an off-the-shelf camera, connected to the SPEX housing. (b) One of the fingers containing the polarization optics for one viewing direction. Light enters the finger on the upper right. From Snik et al. (2010).

Spectrometer optics

Light will enter the slit with a focal ratio of $F/10$, and will be demagnified by the camera lens into $F/3.3$ in order to have a good match with the detector and the specified spectral resolution. The current design has been optimized for an altitude of 300 km, with viewing angles of $0, \pm 14, \pm 28, \pm 42, \pm 56$ degrees. The camera contains three radiation-resistant glass lenses of which two are identical aspheres (see Fig. 2.3a). Manufacturing aspherical surfaces is more difficult than spherical surfaces, but modern manufacturing techniques nowadays can guarantee good quality. Testing is more straightforward as only one test setup is needed to test the twin aspherical components, reducing the costs of such a set-up. For the SPEX prototype, the off-the-shelf CCD camera QImaging Retiga 4000R is used, which has an extremely low dark current of $1.64 \text{ e}^-/\text{pix}/\text{s}$, a read noise of 12 e^- , and a linear full well depth of $40,000 \text{ e}^-$.

For reasons of compactness we decided to use a (quartz) transmission grating, having a spacing of 750 lines per mm. Spectral overlap of orders is partially solved by the quantum efficiency of the intended detector, which is typically zero outside 400–1000 nm, which means that together with the low transmission of the radiation resistant F2G12 lens at shorter wavelengths, the 350–400 nm regions will not be registered. Further filtering of the unwanted wavelengths (750–1000 nm) is done by using a blocking filter.

At least 80% of the energy of all fields and wavelengths should be focused within an area of 2×2 pixels ($50 \times 50 \mu\text{m}$), which has been achieved with this optical design.

2.3.2 Mechanical design

Several renderings of the mechanical design of the SPEX prototype are shown in Fig. 2.4.

The SPEX prototype is designed for environmental testing of the instrument to allow for TRL6 qualification. As such the mechanical design incorporates many design features aimed at the operation of the instrument in harsh space environment and survival of the launch vibrations. In addition the design is very stiff, yet light (0.9 kg) and compact (< 1 liter). The main frame is made out of a solid block of Aluminum of $12 \times 12 \times 6$ cm into a structure of ~ 1.5 mm thickness. Due to the combination of smart design and modern production techniques like spark eroding and diamond turning, we have succeeded in producing a design that requires no active alignment of optical elements, other than the focusing of the spectrometer detector.

A number of numerical simulations have been performed to verify and support the mechanical design. This comprises Finite Element Model (FEM) thermal analysis, stiffness and strength calculations. In particular a large effort was made to reduce the stresses exerted on the elements of the polarization optics. In general changes of stress on optical elements will result in variation of the birefringence. As a result the polarization measurement would be affected in an unpredictable manner and after the calibration of the instrument. As a result, the optical elements are mounted

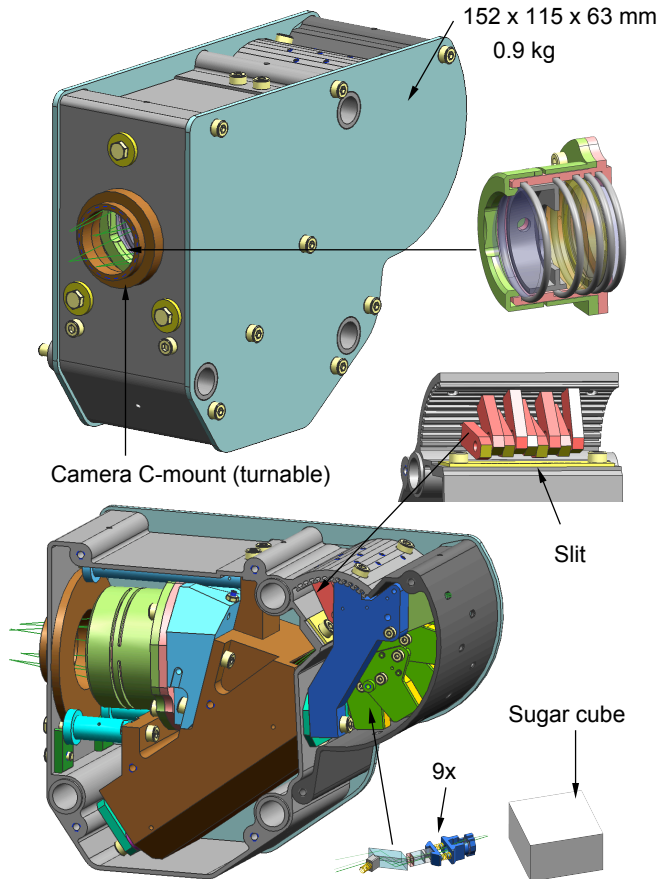


Figure 2.4: Multiple views of the mechanical design of the SPEX prototype.

very stiff to survive the launch vibrations, but yet with very low forces to minimize the induced stresses.

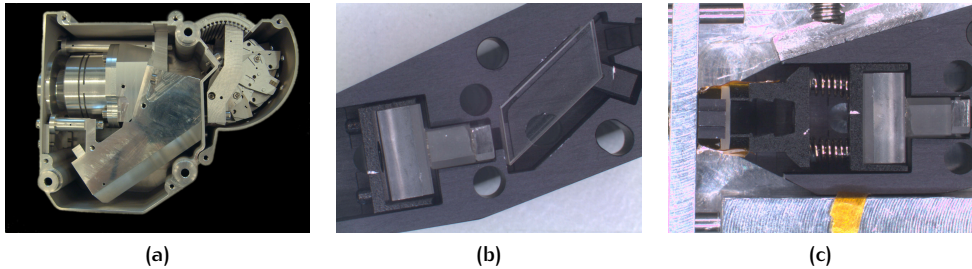


Figure 2.5: (a) The constructed SPEX prototype, with the top lid removed (detector is not shown). (b) Close-up on one of the fingers containing the polarization optics, viz. the BK7G18 Fresnel rhomb, Al_2O_3 crystal, MgF_2 crystal, and αBBO Wollaston prism, from right to left. (c) Another close-up on one of the fingers, showing the spring loaded polarization optics mount, the baffling and slit lens.

2.4 Prototype results

A prototype SPEX instrument has been constructed (see Fig. 2.5), based on the specifications as listed in Table 2.1, and by the design as presented in Section 2.3. Several calibration measurements are being performed to characterize its spectral- and field-of-view behavior, as well as its polarimetric performance. Although the calibration program is still ongoing, some promising results are already presented in Subsection 2.4.1. A detailed field-of-view characterization will be presented in a forthcoming paper, and we plan to determine the polarimetric accuracy within a year.

Ground-based aerosol measurements have been performed using the prototype, as presented in Subsection 2.4.2.

2.4.1 Calibration

A raw detector image showing the two perpendicularly polarized spectra for each of the three fingers containing optics is shown in Fig. 2.6a. This image has been used to determine the pixels corresponding to the centra of the fields-of-view, which show a curvature from 400 to 800 nm of 10 pixels, away from the center of the detector, for the lower and upper finger, when the spectra of the central finger are perfectly horizontal.

The wavelength calibration has been performed by taking exposures of an HgAr spectral line lamp, which produces tens of emission lines between 250 and 920 nm. First the isolines of six wavelengths, quite uniformly distributed between 400 and 800 nm, are determined by fitting a quadratic function through the pixels corresponding to the centra of the fields-of-view, containing the maximum line intensities. Then a third order polynomial is fitted through each detector row, to obtain a complete wavelength map for the detector, as shown in Fig. 2.6b.

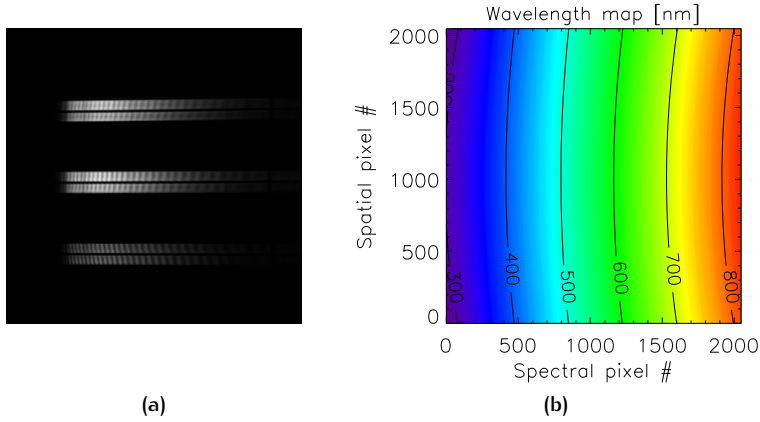


Figure 2.6: (a) Raw detector image of the SPEX prototype, with all three fingers filled with polarization optics illuminated. For each finger, two perpendicularly polarized spectra are measured, corresponding to the two output beams of the Wollaston analyzer. (b) The determined wavelength map, assigning a wavelength to each detector pixel.

The polarimetric efficiency of the central finger has been measured by placing a polarizer at different AoLPs in front of the SPEX prototype. The thus determined DoLP efficiency, averaged over 180° AoLP and corrected for the polarizer's spectral polarizance, is strongly dependent on wavelength (see Fig. 2.7a), with a maximum efficiency of about 90%. This is fully predicted by the SPEX instrument simulator Snik et al. (2010), and can be attributed to the slit function of the spectrometer, in combination with spectral modulation, which is faster at the blue side of the spectrum, such that in the blue the measured intensity is an average over a larger part of the modulated input spectrum. In addition to this spectral dependence, the polarimetric efficiency is also a function of the AoLP of the incoming light, as shown in Fig. 2.7b, showing an amplitude of 0.005 for the efficiency variation. One would expect the highest polarimetric efficiency at AoLP = 0° , because Stokes Q ($+Q$ is in the plane of the Fresnel rhomb's internal reflecting surface) can simply pass through the Fresnel rhomb, whereas an imperfect conversion of U into V causes a decrease in efficiency. However, the highest observed efficiency is close to AoLP = 45° , which can be explained by a misalignment between the Fresnel rhomb and the multiple-order retarder. Stokes Q , after passing through the Fresnel rhomb, will then be partially converted into V , so that it is not fully transmitted or blocked by the analyzer, which is a decrease in Q efficiency. Stokes U , however, will be converted into V , which is always fully converted into linear polarization, albeit at the same offset angle as the multiple-order retarder with respect to Stokes U . This effect apparently drowns out the imperfect Fresnel rhomb performance. Calculations show that, upon neglecting the Fresnel rhomb performance, a misalignment of 1.6° can account for this efficiency variation of size 0.005, which is in perfect agreement with the measured misalignment

of 1.7° (see Fig. 2.7b). The wavelength dependence of the efficiency curve follows from the dispersion of the Fresnel rhomb retardance, so eventually this efficiency curve should be determined also as a function of wavelength.

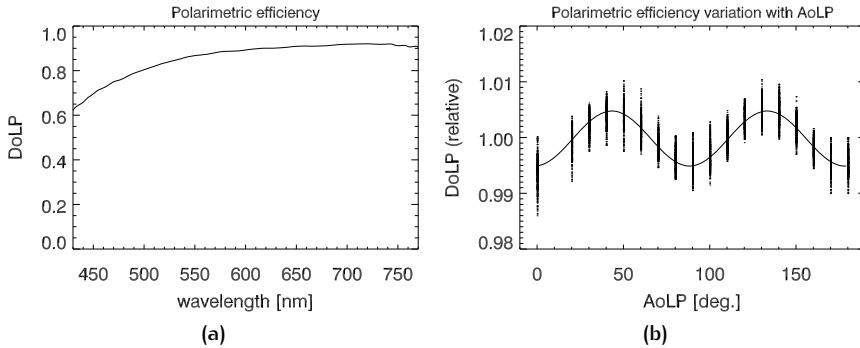


Figure 2.7: (a) The determined spectral polarimetric efficiency, i.e., the measured DoLP in case of 100% linearly polarized input. (b) The measured variation on the polarimetric efficiency, as a function of the AoLP of the incoming light. The relative polarimetric efficiency is determined for all wavelengths simultaneously (dots). A fit of a sine function to the data yields an efficiency variation of 0.005 (solid line).

Partial polarization measurements have been performed, in order to assess the polarimetric performance for $\text{DoLP} < 0.30$, which is the usual regime for scattering polarization measurements. The partial polarization states are created by transmitting light through a glassplate at different angles of incidence. The polarization of the incident light is unknown, as well as the refractive index of the glassplate, so the measurements are fitted to a Mueller matrix model containing these as free parameters. The measurements as a function of different angles of incidence are shown in Figs. 2.8a-c, and the fit residuals are shown in Figs. 2.8d-f. Although the fit residuals across the whole range of incident angles (see Fig. 2.8d) are already within ± 0.006 , the (at least relative) accuracy is expected to be even better, because the systematic errors in the fit residuals indicate that the model is not complete. For example, the effect of multiple reflections inside the glass plate is neglected, as well as beam shift at large angles of incidence. Due to symmetry, the fit residuals for incidence angles close to 0 (see Fig. 2.8e) are almost free from systematic behavior as a function of incident angle, so these measurements can be used to determine the noise level: the total standard deviation, corrected for offsets between different wavelengths, is $4.8 \cdot 10^{-4}$, after averaging 16 almost saturated exposures. The pixels of the off-the-shelf detector of the prototype are 4 times smaller than necessary to meet the required spatial and spectral resolution, so the noise after binning 4×4 pixels is a more relevant quantity, which is $2.0 \cdot 10^{-4}$.

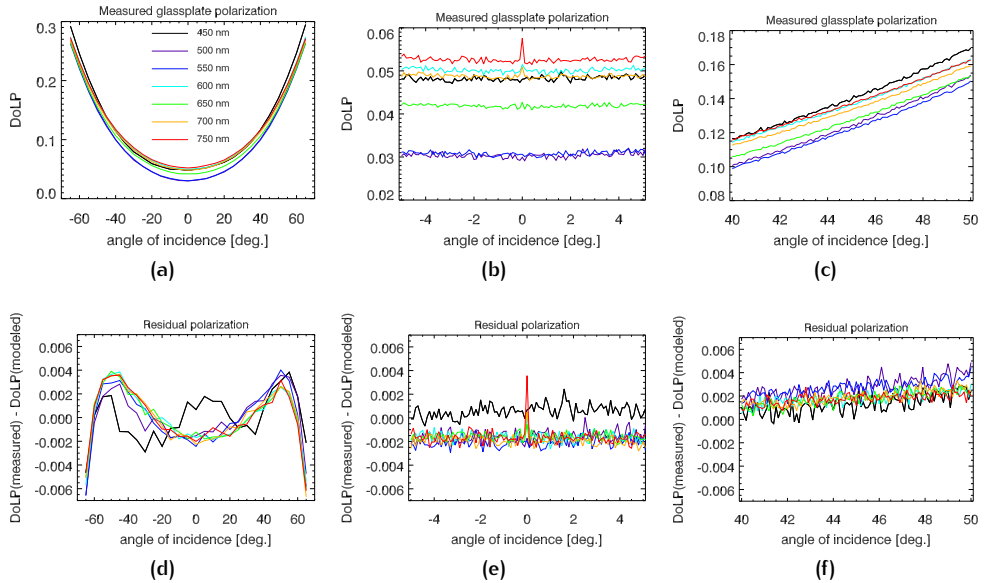


Figure 2.8: Polarization measurements by the SPEX prototype, where the partial polarization states are created by transmitting light through a glassplate at different tilt angles. (a) The full range of incidence angles is sampled with an angular resolution of 5° , and fine steps of 0.1° are taken around (b) 0° and (c) 45° incidence. The polarization of the incident light is unknown, as well as the refractive index of the glassplate, so the measurements for the full range of incidence angles (subfigure (a)) are fitted to a Mueller matrix model containing these as free parameters. The measurements as a function of different glassplate tilt angles are shown in (a-c), and the fit residuals are shown in (d-f). The systematic errors in the fit residuals indicate that the model is not complete. The noise level in subfigure (e) is $4.8 \cdot 10^{-4}$, which becomes $2.0 \cdot 10^{-4}$ after binning 4×4 pixels, corresponding to the required spatial and spectral resolution.

2.4.2 Blue-sky measurements

We performed polarization measurements from the ground with the SPEX prototype to verify its ability to determine atmospheric aerosol properties. The measurements are performed at the Cabauw Experimental Site for Atmospheric Research (CESAR, $51^\circ 58.223' \text{ N}$, $4^\circ 55.575' \text{ E}$), where different aerosol instruments are located, such as an AERONET sun photometer, PM10 and PM2.5 filters and LIDARs, which can be used to either constrain the aerosol retrieval, or to verify retrieved parameter values. The site is located in a rural area, where the closest city is at a distance of 15 kilometers. Within 10 kilometers of the site, the surface is mainly covered with grass.

At three times during the cloudless day of May 25, 2011, the instrument was pointed at about 20 angles from horizon to horizon to sample the scattering phase function. As an example, the dataset corresponding to one of the three sweeps will

be discussed now. The viewing angles are in the north–south plane, and the data was taken between 2:36 and 3:14 pm (GMT+2), so the Sun’s altitude and azimuth are about 55° and 215° , respectively. Data from all three viewing apertures containing optics has been collected, although here we present only the results for the central finger. Fig. 2.9a represents the viewing zenith angles of the measurements that are far enough from the Sun (depicted by the asterisk) to not be subject to possible straylight or detector saturation. The measured polarization as a function of single scattering angle for different wavelengths is shown in Fig. 2.9b, showing maximum values around a single scattering angle of 90° . The two outliers around the 50° single scattering angle correspond to the two measurements close to the south horizon (see Fig. 2.9a), which have a completely different path through the atmosphere than the measurements at the same single scattering angle close to zenith, so the decreased DoLP may be due to multiple scattering. The complete dataset, viz. the measured spectral DoLP for the different viewing angles, is shown in Fig. 2.9c. The following features can be observed:

- The DoLP is relatively high at the shortest wavelengths, because there scattering by molecules, with a relatively high single scattering degree of polarization, plays a significant role. With increasing wavelength, the scattering optical thickness of the molecules decreases, and the polarization is increasingly determined by light that has been scattered by the aerosol particles.
- Around 550 nm, the DoLP is relatively low because of the contribution of weakly polarized light that has been reflected towards the atmosphere by the surface (the so-called ‘green bump’). At the Cabauw site, the surface is mainly covered by grass, which has a relatively high albedo at green wavelengths. The increased contribution of weakly polarized light reflected by the grass can also be seen above 700 nm, since vegetation has high albedos at these long wavelengths (the so-called ‘red edge’).

See reference Aben et al. (1999) for an extensive description of blue sky polarization measurements with the Global Ozone Monitoring Experiment Bread Board Model (GOME BBM) at 300–800 nm with a spectral resolution of about 0.3 nm, and modeling thereof.

Although the polarimetric accuracy of the SPEX prototype for partial polarization measurements is yet to be investigated, the most reliable estimate of the accuracy after calibration so far is given by the wavelength dependent variation of the data in Fig. 2.7b, which is 0.005. In the near future the aerosol retrieval will be performed, by first calculating a general look-up-table of spectral polarization as a function of all relevant aerosol parameters, for a large range of scattering angles, using an adding-doubling algorithm, that calculates polarized radiative transfer including multiple scattering, as described in Stam et al. (1999). The thus determined solution of aerosol parameters will then be improved by iterating through a linearized radiative transfer model, which additionally provides a solid error analysis, as described in Hasekamp & Landgraf (2005).

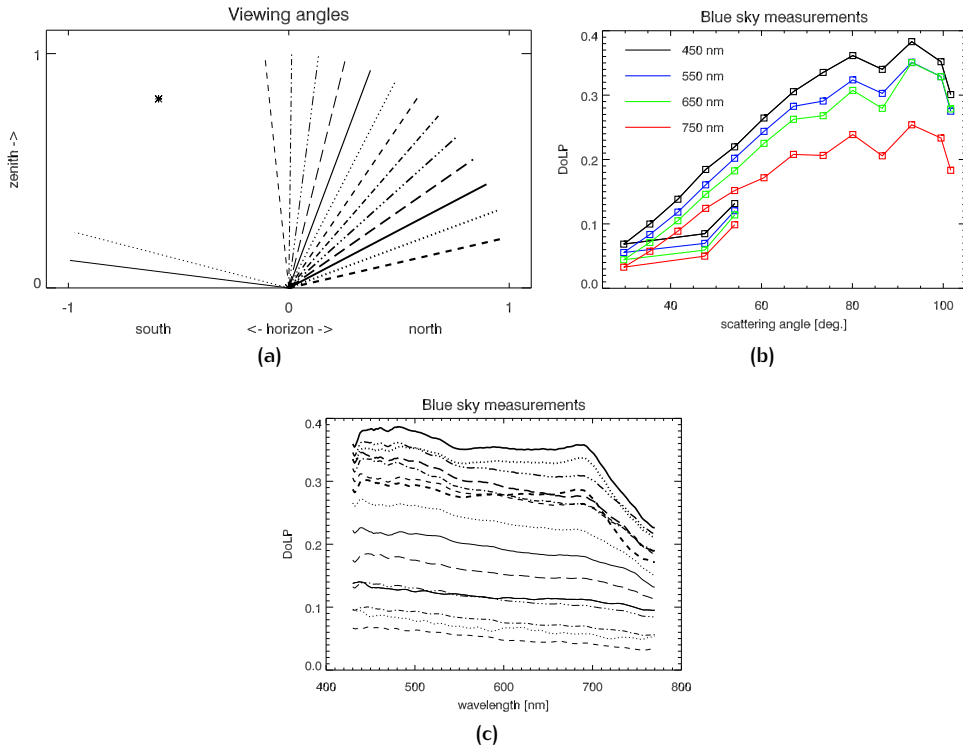


Figure 2.9: Multi-angle spectropolarimetric measurements of a blue sky, performed with the SPEX prototype. (a) The 15 viewing angles in the north–south plane. The approximate position of the Sun is depicted by the asterisk (the Sun is at an angle of 35° with respect to the north–south plane). (b) The degree of polarization behavior with scattering angle, for different wavelengths. (c) The complete dataset, viz. the spectral degree of polarization for the different viewing angles. The coding of the viewing angles corresponds to the coding in subfigure (a).

2.5 Outlook

Our main present objective is to complete the characterization and calibration of the prototype instrument. Absolute calibration of the DoLP is required at levels other than 100% polarized light to determine absolute accuracy and the threshold sensitivity that can be achieved. This will be followed by rework on the prototype to resolve identified discrepancies. Next, the instrument is to be validated and verified by having it airborne. These activities will be undertaken prior to, or in parallel with, preparations for a specific mission opportunity.

The SPEX instrument concept is tailored to missions where a spacecraft orbits a target planetary body. The following missions present target opportunities for SPEX

as a payload on a platform in orbit around a planetary body.

Chinese Mars Orbiter. Recently, the Chinese Academy for Science and Technology (CAST), offered a flight opportunity on their 2015 Mars orbiter mission HX-1. For that mission, SPEX will focus on the characterization of atmospheric dust, water clouds and CO₂ clouds. Deriving the essential properties of dust (typical size, shape, refractive index, optical thickness) will enable a study of the role of dust in the Martian climate. Questions to be addressed are for example how local dust storms develop into much larger ones. Selection of SPEX for this mission will ultimately depend on the ability to achieve a sufficient level of maturity in the next few years.

JUICE. The SPEX team is investigating the feasibility of the polarimetric measurement concept for the Jupiter Icy Moons Explorer (JUICE)¹. SPEX will target clouds and haze structures in the Jovian atmosphere and probe surfaces of the Galilean moons during flybys, with a closer polarimetric look at the surface of Ganymede during the final, low orbit of the spacecraft around this moon. One of the technical challenges is the complexity of the mission profile, demanding compatibility of the instrument concept under a variety of observational and environmental conditions.

ISS. SPEX is also perfectly suited as a remote sensing instrument for Earth atmospheric research. The large uncertainty of radiative forcing by aerosol is considered to be one of the major issues in present day climate studies IPCC (2007) and precludes reliable predictions of climate change. In a dedicated low Earth orbit, SPEX would deliver multi-angle, spectral polarization data that are key to derive the required aerosol parameters. The International Space Station may also serve as a stepping-stone platform for SPEX to demonstrate the remote sensing capabilities. SPEX will be proposed as an instrument in response to ESA's call for experiments for Climate studies from the ISS. For this purpose, achieving good coverage is essential and this requires an extension of the field-of-view of the SPEX design. These points are currently under study.

In addition to these space-based applications, SPEX will also be part of a ground-based aerosol monitoring network. This research, carried out for the Dutch National Institute for Public Health and the Environment (RIVM), aims at determining the health effects of air quality. To that end, the local atmospheric aerosol properties will be remotely sensed, which is cheaper, faster, more accurate, and yields more detailed aerosol information than the current filtering system. At the moment, one ground-based SPEX is being constructed, which will be operational before 2012, to investigate the ability to create an autonomous ground-based network of SPEX instruments.

¹The mission was formerly a NASA-ESA collaboration, under the name of Europa Jupiter System Mission. With the withdrawal of NASA from number of collaborative programs, ESA is reformulating the Cosmic Vision L-class missions.

Acknowledgements

The design study for SPEX, the prototype construction and testing, and the JUICE preparations are supported by PEP grants from the Netherlands Space Office.

Performance of spectrally modulated polarimetry

I: Error analysis and optimization

Spectral polarization modulation is a polarimetric technique that encodes the polarization state in a sinusoidal modulation in the intensity spectrum. It provides snapshot measurements, with no moving or switching components, it does not rely on the exact retardance of the modulating element, or on synchronization between the modulating element and the detector, and a dual-beam implementation allows for a dynamic differential transmission correction. These properties make spectral modulation an interesting candidate for accurate space-based polarimetry, potentially without the need for in-flight calibration. Therefore, we present a complete end-to-end performance analysis for dual-beam spectrally modulated linear polarimetry. We provide an overview of static and dynamic error sources, and identify the worst offenders. The instrument including errors is described in a Mueller matrix model, along with the modulation / demodulation process. We present end-to-end Monte Carlo simulations of the combined performance of the instrument, calibration and measurements. We find that the probability of measuring degree of linear polarization with an error within ± 0.001 (± 0.002) is 76% (99%) after calibration.

Van Harten, Rietjens, Snik et al. *Applied Optics*, To be submitted (2014)

3.1 Introduction

The polarization state of light carries information about the object that scattered, reflected or transmitted it (Hansen & Hovenier 1974, Mishchenko & Travis 1997, Hasekamp & Landgraf 2007), and enhances the contrast between different objects compared to intensity only (Tyo et al. 2006, Keller et al. 2010). The polarization state cannot be measured directly, but is inferred from multiple intensity measurements filtered for different components of the polarization. This polarization modulation can be performed sequentially, e.g. using a rotating or optically variable birefringent retarder, or simultaneously by splitting the beam according to polarization and measuring on different detectors or parts of the same detector. Each technique has its intrinsic limitations: slow temporal modulation suffers from variability of the source or viewing geometry, whereas fast modulation requires strict synchronization between the modulating element and the detector; spatial modulation is limited by transmission differences between the beams and gain differences between the different cameras / pixels (Tyo et al. 2006, Snik & Keller 2013). The differential effects of either modulation technique largely cancel out by combining both modulations in a beam-exchange or dual-beam polarimeter (Semel et al. 1993, Bagnulo et al. 2009, Snik et al. 2014).

This paper deals with a novel polarimetric technique: spectral modulation (Nordsieck 1974, Oka & Kato 1999). The full polarization state is encoded in the amplitudes and phases of sinusoidal modulation patterns in the intensity spectrum, using two static retarders, an analyzer, and a spectrometer. Different retarder and analyzer implementations allow for spectropolarimetry, imaging polarimetry, and combinations thereof (Kudenov & Goldstein 2011, Sparks et al. 2012). The focus in this paper is on a dual-beam implementation for linear spectropolarimetry (Snik et al. 2009), the passive and snapshot equivalent of a beam-exchange polarimeter. The modulation of the two beams is out of phase, such that their sum is the unmodulated intensity spectrum at the spectrograph's intrinsic resolution. In this way, aliasing between spectrally modulated polarization and features in the intensity spectrum is prevented. The redundancy in the both spectrally and spatially modulated polarization is used to extract differential transmission from the data itself, and to measure polarization at full resolution (van Harten et al. 2014c).

Dual-beam spectral polarization modulation is a robust concept because there are no moving or optically switching components, it is a snapshot measurement, it does not rely on the exact retardance of the modulating element, or on synchronization between the modulating element and the detector, and the redundant modulation allows for a dynamic differential transmission correction. We believe that this robustness leads to high polarimetric accuracy and long-term stability. These are particularly interesting assets for space-based polarimetry if this obviates the need for in-flight calibration.

Several errors sources and optimization approaches for spectral polarization modulation have been described in separate publications: aliasing and the dual-beam solution (Craven & Kudenov 2010, Snik et al. 2009), retardance change with temper-

ature, and athermal crystal combinations and correction in data reduction (Okabe et al. 2009, Snik et al. 2009, Taniguchi et al. 2006), diattenuation (polarization dependent transmission) (Okabe et al. 2009) and dichroism (polarization dependent absorption) in the retarders (Kudenov et al. 2007), and alignment and retardance errors (Mu et al. 2013). However, a systematic polarimetric error analysis is notoriously difficult (Tyo 2002, Keller & Snik 2009, de Juan Ovelar et al. 2011). The variety of systematic and random error sources, combined with the facts that polarization errors are matrix quantities, and that a measurement involves a calibration and inversion of the modulation matrix (Ramos & Collados 2008), leads to lengthy matrix equations, and often loss of intuitive understanding, even for relatively simple systems (Zallat et al. 2006, Dong et al. 2012). The most appropriate approach for performance prediction is to make a complete overview of errors, include those in the instrument model, and simulate the combined performance of instrument, calibration and measurements in a Monte Carlo way (Mahler et al. 2011a).

With this first paper in a series of two, we aim to present a complete performance analysis for spectrally modulated polarimetry. First, the instrument is described in Section 3.2, followed by the mathematical frameworks to model the instrument including errors, as well as the modulation / demodulation process in Section 3.3. An overview of error sources and their specific impacts on the polarization measurement is provided in Section 3.4, to differentiate between static and dynamic errors, and to enable the identification of the worst offenders. Sections 3.5 and 3.6 elaborate on the static and dynamic errors, and describe their inclusion in the instrument model. Finally, end-to-end simulations are presented, including errors in the instrument, calibration and measurements.

The second paper in this series (Rietjens et al. 2014) presents the practical implementation of the data reduction for the SPEX instrument, as well as its absolute polarimetric calibration using various degrees of polarization as input states. SPEX is a dual-beam spectrally modulating linear polarimeter for space-based remote sensing of aerosols in the Earth's atmosphere. For this application, the required accuracy in the degree of linear polarization P_L is $0.001 + 0.005 \cdot P_L$ (Mishchenko & Travis 1997, Hasekamp & Landgraf 2007).

3.2 Instrument

A spectrally modulating linear polarimeter consists of the following components:

- achromatic quarter-wave retarder with fast axis at 0° ;
- multiple-order retarder with fast axis at -45° ;
- polarizer at 0° or polarizing beam splitter splitting polarization at 0 and 90° ;
- spectrometer.

Figure 3.1 provides a schematic representation of the instrument, including the definitions of the orientations and Stokes parameters (see also Eq. (3.2)). The figure also

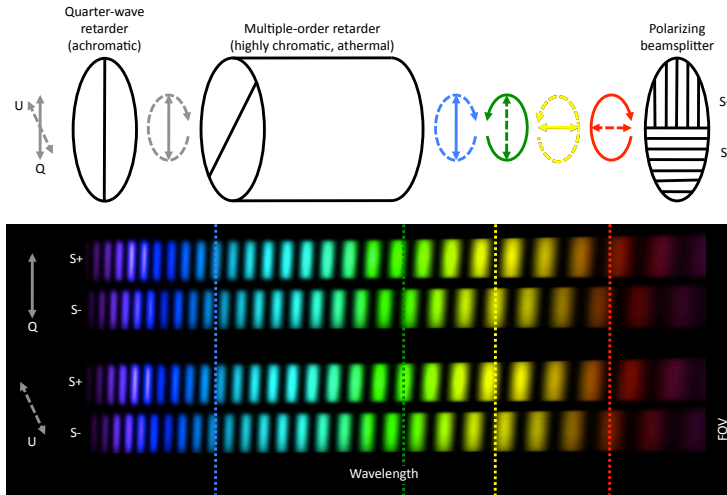


Figure 3.1: Schematic representation of a dual-beam spectrally modulating linear polarimeter, like SPEX. Both spectra out of the polarizing beamsplitter carry the spectral polarization information according to Eq. (3.1): the degree and angle of linear polarization are described by the amplitude and phase of the spectral modulation pattern, respectively. For example, the modulation of fully polarized light along Q (solid arrows) and U (dashed arrows) is shown as they propagate through the instrument for four wavelengths. The same wavelengths are indicated with vertical dotted lines in the resulting intensity pattern on the detector (black part). The slit direction (denoted by FOV) is perpendicular to Stokes Q .

shows the spectral modulation of linearly polarized light as it propagates through the instrument. The modulation takes place inside the multiple-order retarder, which changes the polarization ellipticity in a highly wavelength dependent way. The multiple-order retarder induces an absolute phase shift of $\delta \approx 25 \mu\text{m}$ between the components of the incoming polarization along its ordinary and along its extraordinary axis. However, relative to the wavelength of the light, this absolute retardance is a gradually changing retardance of $\sim 60\text{--}30$ waves from $400\text{--}800$ nm, respectively. Hence, upon analyzing the modulated polarization using the polarizing beam-splitter, ~ 30 modulation cycles appear in the intensity spectrum of each beam. Linear polarization aligned with the axes of the multiple-order retarder is not modulated, therefore the achromatic quarter-wave retarder first converts linear polarization at 45° into circular polarization, and vice versa. After the multiple-order retarder, the ellipticity of the polarization under study varies rapidly with wavelength, such that the spectrum transmitted by the polarizing beam-splitter shows a sinusoidal modulation (see Fig. 3.1). As shown in Section 3.3.2, the modulated

spectrum is described by:

$$\begin{aligned} S_{\pm}(\lambda) &= \frac{1}{2} I_0(\lambda) [1 \pm P_L(\lambda) \cos \psi(\lambda)], \\ \psi(\lambda) &\equiv \frac{2\pi\delta(\lambda)}{\lambda} + 2\phi_L(\lambda), \end{aligned} \quad (3.1)$$

where $P_L(\lambda)$ and $\phi_L(\lambda)$ are the degree and angle of linear polarization, respectively, $I_0(\lambda)$ is the intensity spectrum, and $\delta(\lambda)$ is the multiple-order retardance.

For a single-beam setup, features in the intensity spectrum can alias with the modulation pattern, thereby creating spurious polarization. This is the main reason for using a polarizing beam-splitter, since the sum of the two orthogonally polarized beams is the unmodulated spectrum at the spectrograph's intrinsic resolution (Snik et al. 2009, Craven & Kudenov 2010). This intensity is consecutively used to normalize the modulated spectra. Moreover, the redundant modulation allows for the extraction of differential transmission between the beams from the data itself, and enables polarimetry in spectral lines (van Harten et al. 2014c).

3.3 Measurement formalism

In this section the formalisms are described that relate the true incoming polarization to the measured polarization. The baseline instrument model is set up, that allows for inclusion of instrumental errors in subsequent sections. A general modulation / demodulation formalism is adopted, that employs a computationally cheap matrix inversion for demodulation, thereby enabling the simulation of many perturbed instruments, calibrations, and measurements in Section 3.7. Moreover, the formalism provides a generic metric for the measurement efficiency of a polarimeter.

Note that the results obtained in this paper do not depend on the choice of (de)modulation formalism. Algorithms based on Fourier analysis (Oka & Kato 1999), direct deprojection (Sparks et al. 2012), or curve fitting (Snik et al. 2009, Rietjens et al. 2014) are all equivalent in that they reconstruct continuously modulated Stokes parameters from an orthogonal basis (Alenin & Tyo 2014).

3.3.1 Polarization modulation

The polarization state of the light is described by the Stokes vector:

$$\mathbf{S} = (I, Q, U, V)^T, \quad (3.2)$$

where I is the intensity, Q is the difference in intensity between the vertically and the horizontally polarized components, U is the intensity difference between $\pm 45^\circ$, and V describes the amount and rotational direction of circular polarization. The Stokes parameters are related to the degree (P_L) and angle (ϕ_L) of linear polarization,

according to:

$$Q/I = P_L \cos 2\phi_L, \quad (3.3)$$

$$U/I = P_L \sin 2\phi_L. \quad (3.4)$$

Each optical element in a polarimeter, or any linear effect on the polarization, is described by a Mueller matrix \mathbf{M} , that relates the incoming and outgoing Stokes vectors according to:

$$\mathbf{S}_{\text{out}} = \mathbf{M}\mathbf{S}_{\text{in}}. \quad (3.5)$$

The entire optical train can thus be described by one Mueller matrix \mathbf{M}_{tot} :

$$\mathbf{M}_{\text{tot}} = \mathbf{M}_n \mathbf{M}_{n-1} \dots \mathbf{M}_1, \quad (3.6)$$

where \mathbf{M}_1 is the optical component that is encountered by the light first.

Since optical detectors are insensitive to polarization, a polarimeter filters for different polarization directions before measuring the corresponding intensities. Formally, a polarimeter takes on m different modulation states, each with a different \mathbf{M}_{tot} , and the corresponding m intensities are measured as \mathbf{I} . A polarization measurement can thus be described by:

$$\mathbf{I} = \mathbf{O}\mathbf{S}, \quad (3.7)$$

where \mathbf{O} is the $m \times 4$ modulation matrix, composed of the first rows of each \mathbf{M}_{tot} matrix. The polarimetric demodulation can then be described by a matrix inversion process, according to:

$$\begin{aligned} \mathbf{S} &= \mathbf{D}\mathbf{I}, \\ \mathbf{D} &= (\mathbf{O}^T \mathbf{O})^{-1} \mathbf{O}^T, \end{aligned} \quad (3.8)$$

where \mathbf{D} is the optimum demodulation matrix, namely the Moore-Penrose inverse of \mathbf{O} (Tyo 2002, del Toro Iniesta & Collados 2000).

The goal in polarimetric calibration is to find the modulation matrix \mathbf{O} and the corresponding demodulation matrix \mathbf{D} . However, due to imperfect calibration an erroneous demodulation matrix $\mathbf{D}^* \equiv \mathbf{D} + \Delta\mathbf{D}$ is determined. Moreover, instrument changes after calibration, e.g. due to temperature fluctuations, result in a perturbed modulation matrix of $\mathbf{O}^{**} \equiv \mathbf{O} + \Delta\mathbf{O}$. In addition, the measured intensities suffer from systematic detection errors $\Delta\mathbf{I}$ like residual dark signal, detector non-linearity, or imperfect gain table calibration, as well as zero-mean random noise with a standard deviation of σI . Hence, the actual measurements are given by $\mathbf{I}^{**} = \mathbf{O}^{**} \mathbf{S} + \Delta\mathbf{I} \pm \sigma I$. Since the measurements are demodulated with \mathbf{D}^* , the measured Stokes vector is given by:

$$\begin{aligned} \mathbf{S}^{**} &= \mathbf{D}^* \mathbf{I}^{**} \\ &= \mathbf{S} + (\mathbf{D}\Delta\mathbf{O} + \Delta\mathbf{D}\mathbf{O}^{**}) \mathbf{S} + \mathbf{D}^* \Delta\mathbf{I} \pm \sigma\mathbf{S}, \end{aligned} \quad (3.9)$$

$$\sigma S_i = \sigma I \left(\sum_{j=1}^m D_{ij}^{*2} \right)^{1/2}. \quad (3.10)$$

Equation (3.9) will be used throughout this paper to express the polarimetric impact of a variety of error sources in spectrally modulated polarimetry.

In an efficient polarimeter, the amplitude or contrast of the polarization modulation pattern is maximized, in order to minimize the propagation of measurement noise to the Stokes parameters in the demodulation process (see Eq. (3.10)). This leads to the following generic metric for the measurement efficiency for the i th Stokes parameter (del Toro Iniesta & Collados 2000):

$$\epsilon_i = \left(m \sum_{j=1}^m D_{ij}^{*2} \right)^{-1/2}. \quad (3.11)$$

Comparison of Eqs. (3.10) and (3.11) shows that ϵ is directly proportional to the polarimetric signal to noise ratio. The maximum efficiencies for a normalized modulation matrix are given by:

$$\epsilon_1 \leq 1, \quad \sum_{i=2}^4 \epsilon_i^2 \leq 1. \quad (3.12)$$

For example, an ideal and balanced linear polarimeter, such as the spectral modulator described in Section 3.2, exhibits an efficiency of $\epsilon = (1, 1/\sqrt{2}, 1/\sqrt{2}, 0)$, just like a rotating-polarizer polarimeter.

Imperfections in the instrument, such as misalignments or retardance deviations, may lead to reduced modulation amplitudes and measurement efficiencies. Uneven or sparse sampling of the modulation pattern also reduces the efficiency.

3.3.2 Instrument model

A spectrally modulating linear polarimeter is modeled as a train of Mueller matrices, according to Eq. (3.6). The baseline instrument is shown to produce spectral modulation according to Eq. (3.1). In subsequent sections, various errors are included in this model.

The Mueller matrix of a retarder that induces a phase retardation of Δ between polarization along the vertical and the horizontal axis is given by:

$$\mathbf{M}_{\text{ret}}(\Delta) = \begin{pmatrix} 1 & 0 & 0 & 0 \\ 0 & 1 & 0 & 0 \\ 0 & 0 & \cos \Delta & -\sin \Delta \\ 0 & 0 & \sin \Delta & \cos \Delta \end{pmatrix}. \quad (3.13)$$

In the case of a quarter-wave retarder $\Delta = \pi/2$. The Mueller matrix of the multiple-order retarder is obtained by rotating this matrix over $\phi = -45^\circ$, according to:

$$\mathbf{M}(\phi) = \mathbf{R}(-\phi) \mathbf{M} \mathbf{R}(\phi), \quad (3.14)$$

using the rotation matrix:

$$\mathbf{R}(\phi) = \begin{pmatrix} 1 & 0 & 0 & 0 \\ 0 & \cos 2\phi & \sin 2\phi & 0 \\ 0 & -\sin 2\phi & \cos 2\phi & 0 \\ 0 & 0 & 0 & 1 \end{pmatrix}. \quad (3.15)$$

The Mueller matrix of a partial polarizer with a transmission of $T_{s,p}$ along $\pm Q$ is given by:

$$\mathbf{M}_{\text{pol}} = \begin{pmatrix} \frac{T_s+T_p}{2} & \frac{T_s-T_p}{2} & 0 & 0 \\ \frac{T_s-T_p}{2} & \frac{T_s+T_p}{2} & 0 & 0 \\ 0 & 0 & c\sqrt{T_s T_p} & s\sqrt{T_s T_p} \\ 0 & 0 & s\sqrt{T_s T_p} & c\sqrt{T_s T_p} \end{pmatrix}, \quad (3.16)$$

with $c = 1$ and $s = 0$, unless the partial polarizer induces a phase shift between s and p , as is the case with anti-reflection coatings or surface contamination (see Section 3.6.3).

The total Mueller matrix for, e.g., the S_+ beam in the ideal instrument is thus given by:

$$\begin{aligned} \mathbf{M}_+(\lambda) &= \mathbf{M}_{\text{pol}}(T_s = 1, T_p = 0) \dots \\ &\quad \mathbf{R}(45^\circ) \mathbf{M}_{\text{ret}}\left(\frac{2\pi\delta}{\lambda}\right) \mathbf{R}(-45^\circ) \dots \\ &\quad \mathbf{M}_{\text{ret}}(\pi/2) \\ &= \frac{1}{2} \begin{pmatrix} 1 & \cos \frac{2\pi\delta}{\lambda} & \sin \frac{2\pi\delta}{\lambda} & 0 \\ 1 & \cos \frac{2\pi\delta}{\lambda} & \sin \frac{2\pi\delta}{\lambda} & 0 \\ 0 & 0 & 0 & 0 \\ 0 & 0 & 0 & 0 \end{pmatrix}. \end{aligned} \quad (3.17)$$

The modulated intensity spectrum is the product of the first row of $\mathbf{M}_+(\lambda)$ and the incoming Stokes vector, so Q is modulated with the cosine wave and U with the sine wave. This can be written as Eq. (3.1), using Eq. (3.4) and one of the Prosthaphaeresis formulas.

During demodulation, S_+ is first normalized by the unmodulated intensity spectrum $S_+ + S_-$. Therefore, the normalized S_+ and S_- are not independent, so it is sufficient to consider only the model for S_+ .

Since the polarization modulation is performed in the spectral domain, the spectral resolution of the demodulated polarization products is lower than the resolution of the spectrometer. The polarization at wavelength λ is typically (but not necessarily) demodulated in a spectral window centered around λ that spans one modulation cycle. Considering Eq. (3.1), the size $\Delta\lambda$ of the spectral window is thus given by the solution of $\frac{\delta}{\lambda - \Delta\lambda/2} = \frac{\delta}{\lambda + \Delta\lambda/2} + 1$, which is $\sim \lambda^2/\delta$.

The modulation matrix $\mathbf{O}_+(\lambda)$ for one modulation cycle centered around λ is composed of the first rows of the normalized matrices $\mathbf{M}_+(\lambda_i)$ for all m wavelength samples λ_i inside one modulation cycle, i.e.:

$$\mathbf{O}_+(\lambda) = \begin{pmatrix} 1 & \cos \frac{2\pi\delta}{\lambda_0} & \sin \frac{2\pi\delta}{\lambda_0} & 0 \\ 1 & \cos \frac{2\pi\delta}{\lambda_1} & \sin \frac{2\pi\delta}{\lambda_1} & 0 \\ \vdots & \vdots & \vdots & \vdots \\ 1 & \cos \frac{2\pi\delta}{\lambda_{m-1}} & \sin \frac{2\pi\delta}{\lambda_{m-1}} & 0 \end{pmatrix},$$

$$\lambda_i = \lambda + \Delta\lambda \left(\frac{i}{m} - \frac{1}{2} \right). \quad (3.18)$$

This generalized modulation matrix representation helps demystify the spectral modulation technique by showing the analogy with e.g. temporal modulation using a stepped retarder polarimeter. Moreover, it allows for a straightforward propagation of instrumental and detection errors, according to Eq. (3.9), and calculation of measurement efficiencies, according to Eq. (3.11). Demodulation can be as straightforward and computationally cheap as using the inverse of the modulation matrix, according to Eq. (3.8) (Sabatke et al. 2003). The practical implementation of the demodulation of SPEX measurements and its advantages are presented in the second paper in this series (Rietjens et al. 2014).

3.4 Error analysis

In this section, various error sources are identified, and classified according to polarimetric impact. The effect of imperfections in the instrument, calibration and detections is twofold:

- Static imperfections in the instrument that are determined during calibration do not lead to polarimetric errors. However, the calibrated modulation matrix will have reduced efficiencies, so the instrument is more sensitive to detection errors.
- Dynamic instrument changes after calibration, as well as errors in the calibration, and detection errors directly translate into polarization errors, according to Eq. (3.9).

An overview of error sources in spectrally modulated linear polarimetry is presented in Table 3.1. Arranged per error source (rows) and instrument component (columns), it provides short descriptions of the errors and their quantitative impacts on the measurement of degree of linear polarization, which is often the main observable. The calculations and assumptions behind these numbers are presented in Sections 3.5 and 3.6.

	Quarter-wave retarder (QWR)	Multiple-order retarder (MOR)	Polarizing beamsplitter (POL)	Spectrometer	
STATIC	Intrinsic	Retardance deviation causes incomplete transformation of U into V . Reduction of modulation amplitude for U of $\lesssim 10^{-4}$.	Retardance may deviate from nominal value due to uncertainty in refractive index or thickness. After calibration, this has no impact on polarimetry.	Non-ideal extinction ratio reduces modulation amplitudes by $\sim 2 \cdot 10^{-5}$.	Finite spectral resolution washes out the modulation contrast by $\lesssim 0.5$.
	Stress	Inherent and clamping stress in glass cause birefringence, and hence phase retardation along unknown axes. Reduction of modulation amplitude for U of $\lesssim 0.02$.	Worst case, clamping stress birefringence is aligned with QWR. Reduction of modulation amplitude for U of $\lesssim 10^{-10}$.	Worst case, clamping stress birefringence is at intermediate angle between MOR and POL. Negligible reduction of modulation amplitudes.	
	Diattenuation	Transmission at an interface depends on refractive index. The axes of a birefringent retarder therefore exhibit differential transmission, causing instrumental polarization along Q of $\sim 3 \cdot 10^{-4}$.	Differential transmission along MOR axes is not modulated, so it is not measured as instrumental polarization. It rotates the modulation away from polarizer axes, reducing the modulation amplitudes by $\sim 6 \cdot 10^{-8}$.	Differential transmission along POL axes does not alter the modulation pattern. Residual differential transmission between the two modulated spectra is extracted from the data.	Residual differential transmission between the two modulated spectra after calibration is extracted from the data.
	Alignment	Q , by definition aligned with QWR, is not at 45° with respect to MOR in case of misalignment. Reduction of modulation amplitude for Q of $\sim 4 \cdot 10^{-5}$.	Equivalent to the combined effect of joint misalignment of QWR and POL. Reduction of modulation amplitude of $\sim 2 \cdot 10^{-4}$ for Q and $\sim 4 \cdot 10^{-5}$ for U.	The linear polarization out of the MOR at the modulation maxima and minima is misaligned with polarizer. Reduction of modulation amplitudes of $\sim 4 \cdot 10^{-5}$.	Stray light and ghosts directly disturb modulation pattern. Need to be suppressed at the level of the polarimetric accuracy, by design or in data-reduction.
	Non-normal incidence	Fresnel rhombs utilize phase shift at total internal reflection on hypotenuse at specific angle. Non-normal incident rays reflect at different angles, resulting in different phase shifts. Reduction of modulation amplitude for U of $\lesssim 10^{-4}$.	Retardance change due to longer path and different projection onto refractive indices moves modulation pattern in spectral direction. Finite instantaneous field of view washes out the modulation contrast by $\lesssim 2 \cdot 10^{-4}$.	The maximum FOV for a calcite double Wollaston prism with index matching gel is $\pm 17^\circ$. Beyond this angle one of the polarizations undergoes total internal reflection instead of transmission.	
DYNAMIC	Non-normal incidence	Differential transmission for polarization parallel / perpendicular to plane of incidence. Instrumental polarization along Q of $\sim 6 \cdot 10^{-3}$.	Differential transmission for polarization parallel / perpendicular to plane of incidence at MOR entrance creates instrumental polarization along Q of $\sim 3 \cdot 10^{-3}$. Differential transmission at MOR exit is aligned with POL axes, so it does not alter the modulation pattern.	Differential transmission along POL axes does not alter the modulation pattern. Residual differential transmission between the two modulated spectra is extracted from the data.	
	Intrinsic	Contamination on first surface reduces diattenuation, and changes differential transmission and retardance at non-normal incidence. Uncertainty in instrumental polarization along Q of $\lesssim 6 \cdot 10^{-5}$.			Detection uncertainty in P_L of $5 \cdot 10^{-4}$ due to shot noise, $2 \cdot 10^{-3}$ due to read-out noise. Dark noise is negligible, even for higher temperatures. Residual non-linearity of 10^{-3} causes error in P_L of $\lesssim 3 \cdot 10^{-4}$. Residual relative flat-field variations of 10^{-3} induce P_L error of $4 \cdot 10^{-4}$.
	Temperature		Retardance deviation shifts modulation pattern in spectral direction. This spurious ϕ_L change induces error in P_L , via ϕ_L -dependent efficiency correction, of $\sim 2 \cdot 10^{-4}/K$, or $\sim 5 \cdot 10^{-5}/K$ with temperature-compensating crystal combination.		Defocus due to thermal expansion of spectrograph reduces modulation contrast by $\lesssim 7 \cdot 10^{-9}/K$. Athermal spectrograph design is desired.
		Thermal expansion changes the forces on the optics, and hence the stress birefringence therein. Reduction of modulation amplitude for U of $\lesssim 2 \cdot 10^{-9}/K$.	Thermal expansion changes the forces on the optics, and hence the stress birefringence therein. Reduction of modulation amplitude for U of $\lesssim 10^{-10}/K$.	Thermal expansion changes the forces on the optics, and hence the stress birefringence therein. Negligible reduction of modulation amplitudes.	Differential wavelength shift for the two modulated beams leads to skewed modulation patterns after normalization, with an equivalent reduction of the modulation contrast of $\lesssim 2 \cdot 10^{-8}/K$.
	Non-normal incidence	Inhomogeneous illumination of instantaneous field of view causes uncertainty in angle of incidence and hence retardance. This introduces uncertainty in modulation amplitude for U of $\lesssim 10^{-5}$.	Inhomogeneous illumination of instantaneous field of view causes uncertainty in angle of incidence and hence retardance and ϕ_L. Via the ϕ_L dependent efficiency correction, this introduces uncertainty in P_L of $\ll 3 \cdot 10^{-4}$, or $\ll 2 \cdot 10^{-5}$ with compensating crystal combination.		
	Inhomogeneous illumination of instantaneous field of view causes uncertainty in angle of incidence, and hence in instrumental polarization along Q of $\lesssim 5 \cdot 10^{-5}$.	Inhomogeneous illumination of instantaneous field of view causes uncertainty in angle of incidence, and hence in instrumental polarization along Q of $\lesssim 3 \cdot 10^{-5}$.			

Table 3.1: Overview of error sources in spectrally modulated linear polarimetry. The static errors are determined during instrument calibration, whereas the dynamic errors are still uncertain after calibration, and hence limit the polarimetric performance. Major effects are shown in black, with the worst offenders in bold, and minor effects in grey. The temperature effects apply for a range of $0 < T < 40^\circ\text{C}$, and the effects of non-normal incidence for a $\pm 15^\circ$ slit along $-Q$. The errors are explained in more detail in Sections 3.5 and 3.6.

3.4.1 Worst offenders

The error overview in Table 3.1 helps to identify the worst offenders, and to define specific instrument design requirements. It shows that the most critical component is the spectrometer, including the detector. The potentially enormous static reduction of the modulation amplitude due to the finite spectral resolution needs to be taken into account in the design of the instrument and observing strategies, to get a sufficient signal to noise ratio. In the end, the performance of the instrument is limited by the dynamic errors. A potential worst offender there is spectrograph defocusing with temperature, which directly translates into modulation contrast reduction. However, spectrographs can be designed such as to have a temperature-compensated focus. Combined with an athermal combination of multiple-order retarders, spectrally modulating polarimeters are usable over a large temperature range. The error overview shows that the polarimetric performance of such an athermal instrument is shot noise limited at the $5 \cdot 10^{-4}$ level.

3.4.2 Modulation errors

The impact of static and dynamic errors on the spectral modulation patterns for fully polarized light along Q and U is shown in Fig. 3.2. The modulation is shown at the blue edge of the 400–800 nm spectrum, for normal incidence and 15° incidence (left and right half of the page, respectively). Realistic values for errors are applied as described in Table 3.1, and in more detail in Sections 3.5 and 3.6, and as used later on in the end-to-end simulation (see Section 3.7).

The upper plots demonstrate the spectral smearing effect due to a relatively low spectral resolution compared to the modulation period, which is typical for the blue end of a grating spectrometer. This severely reduces the modulation amplitudes, and hence the polarimetric efficiencies, to ~ 0.6 .

The first (and third) column shows the effect of static errors, as reduced modulation amplitudes compared to the baseline instrument. When constructing an instrument, any of these simulated outcomes is possible, due to random misalignments, retardance deviations, and stress birefringence. Note that the actually constructed instrument will be calibrated, so the range of modulation amplitudes due to static errors does not translate into polarimetric errors.

The second (and fourth) column shows the effect of dynamic errors on the actual constructed and calibrated instrument. After calibration, there is a residual uncertainty in the response, due to temperature fluctuations of ± 0.5 K, inhomogeneous illumination of the $\pm 0.125^\circ$ instantaneous fields-of-view, and the growth of a 10 nm-thick contamination layer on the first surface. The range of these red lines at the modulation maxima and minima is a measure of the instrument's polarimetric stability, in the absence of detection errors and calibration errors. The latter effects are included in end-to-end simulations in Section 3.7. The distribution of the modulation patterns due to dynamic errors is narrower at the long-wavelength side of the plots. This is the correlated temperature effect of spectrograph defocus that

decreases the modulation amplitude with increasing temperature, and a simultaneous increase in multiple-order retardance that shifts the modulation pattern towards longer wavelengths.

The plots for non-normal incidence are centered around the wavelengths that are expected to have a modulation maximum or minimum, taking into account the multiple-order retardance at non-normal incidence (see Section 3.6.2). The residual shift of the modulation patterns for U towards higher wavelengths is caused by the differential transmission along $\pm Q$, leading to a real change in angle of linear polarization.

3.4.3 Calibration

Polarimetric calibration entails the application of fully linearly polarized input at different angles of polarization. This provides the modulation amplitude, i.e. the polarimetric scale, as well as the multiple-order retardance from the frequency of the modulation. The dependency on the angle of polarization mainly stems from imperfections in the quarter-wave retarder that pertains only to U , not Q . Therefore, even though the degree of linear polarization is the main observable, the angle of polarization needs to be measured to correct P_L for the appropriate modulation efficiency. More advanced calibration includes the measurement of an unpolarized source to determine the polarimetric zero point due to instrumental polarization. The response between $P_L = 0$ and $P_L = 1$ is anticipated to be linear, apart from the possible effect of detector non-linearity (see Section 3.6.4). The most complete calibration also includes partial polarization, which requires an advanced polarization state generator and calibration thereof (Mahler & Chipman 2011, Rietjens et al. 2014). The polarimetric calibration of the SPEX instrument using such a calibration stimulus is described in paper II (Rietjens et al. 2014).

3.5 Static errors

This section elaborates on the static errors as listed in Table 3.1. Component-specific considerations are given first, before discussing the impact of system-level effects, such as behavior with temperature and incidence angle. The polarimetric impact of errors is calculated by including them in Eq. (3.17). Some errors can be included directly, like a retardance that deviates from its nominal value, for others additional Mueller matrices are provided.

3.5.1 Quarter-wave retarder

Linear polarization aligned with the axes of the multiple-order retarder is not modulated, only polarization with components along both axes and circular polarization is. In order to create sensitivity to both Q and U , the task of the quarter-wave retarder is to turn U into V and vice versa.

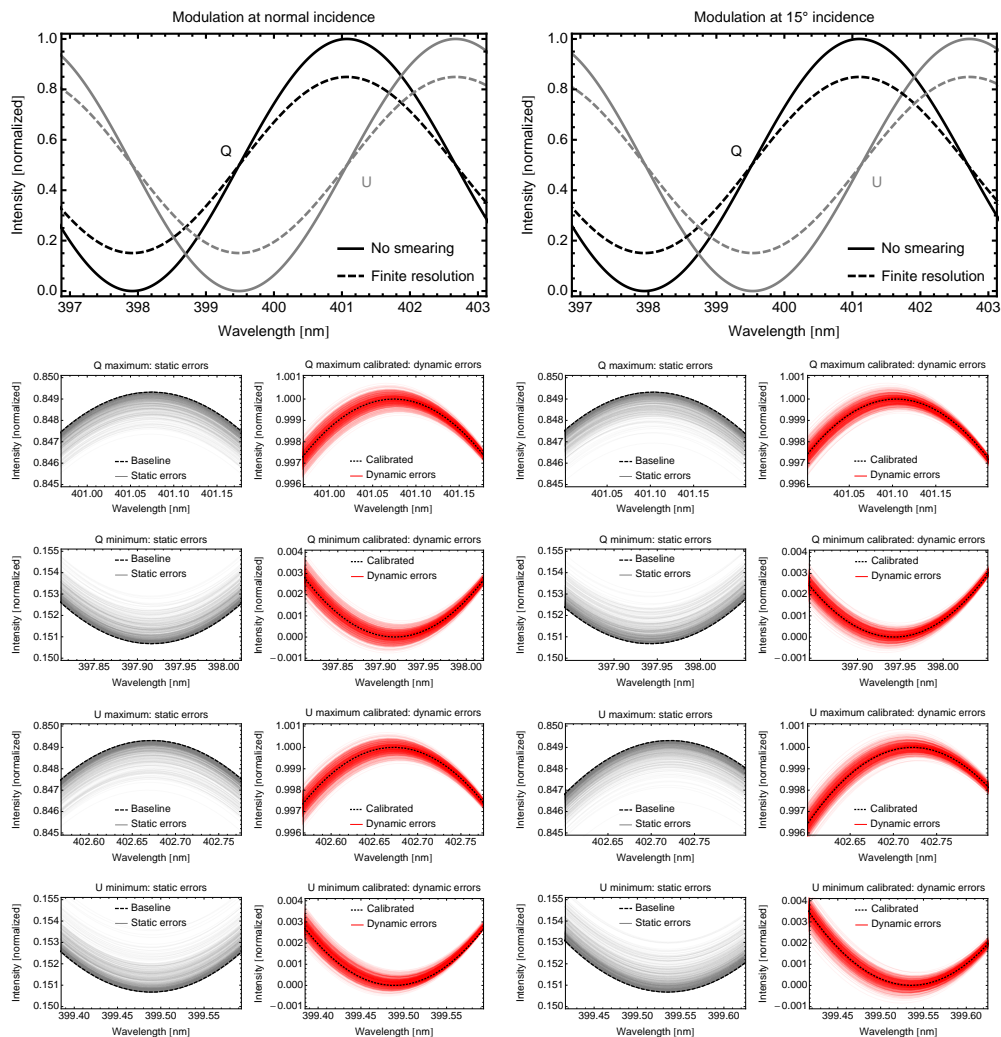


Figure 3.2: The spectral modulation pattern for fully polarized input at Q and U , subject to static and dynamic errors. *Left half of the page:* At normal incidence. *Right half of the page:* At 15° incidence. *Top row:* Modulation in the absence of spectral smearing, and the baseline instrument including finite spectral resolution and imperfect focus. *Row 2:* Zoomed in around modulation maximum for Q . *Row 3:* Zoomed in around modulation minimum for Q . *Row 4:* Zoomed in around modulation maximum for U . *Row 5:* Zoomed in around modulation minimum for U . *Columns 1 & 3:* Baseline instrument, and the effect of random static errors (misalignments, retardance deviations, stress birefringence) for 4000 simulated instruments. *Columns 2 & 4:* The calibrated instrument (one of the simulated instruments with static errors from row 2), and the effect of random dynamic errors (due to uncertainty in temperature, angle of incidence, and contamination) for 4000 simulated instruments.

If the retardance is not exactly a quarter wave, the residual polarization along U will pass through the polarizer unmodulated. In order to maximize the modulation contrast and measurement efficiency for U across the entire spectrum, the retardance needs to be achromatic. Even the most achromatic retarders, like Fresnel rhombs, exhibit a spectral retardance offset of $\pm 2.5 \cdot 10^{-3}$ waves within 400–800 nm. This translates into a reduction of the modulation amplitude for U of $\lesssim 10^{-4}$.

In the case of misalignment, polarization at 45° with respect to the quarter-wave retarder is still turned into V and hence fully modulated. However, polarization along its axes, defined as $\pm Q$, is then partially aligned with the multiple-order retarder. A typical alignment error of 0.25° leads to a reduction of the modulation amplitude for Q of $5 \cdot 10^{-4}$.

3.5.2 Multiple-order retarder

A static deviation of the multiple-order retardance from its nominal value causes a spectral shift of the modulation pattern, but does not change the modulation amplitude. Therefore, it has no impact on the polarimetric performance of the instrument after calibration.

The effect of misalignment with respect to the quarter-wave retarder is discussed in Section 3.5.1. Misalignment with respect to the polarizer causes an overall reduction of the modulation contrast, because the linear polarization out of the multiple-order retarder is never perfectly parallel or perpendicular to the polarizer axes. The combined effect for a typical alignment error of 0.25° is a reduction of the modulation amplitude for Q of $\sim 2 \cdot 10^{-4}$ and for U of $\sim 4 \cdot 10^{-5}$.

3.5.3 Polarizing beamsplitter

The modulation amplitude scales with the polarizance of the polarizing beamsplitter, defined as $(T_s - T_p)/(T_s + T_p)$. The extinction ratio T_s/T_p of a Wollaston prism is at least 10^5 , which results in a maximum contrast reduction of $4 \cdot 10^{-5}$.

The field-of-view that a calcite Wollaston prism can serve is limited to $\pm 14^\circ$, because the hypotenuse needs to be large enough to provide sufficient beam separation, but at the same time, the angle between rays at the edge of the field-of-view and the hypotenuse gets smaller, leading to total internal reflection instead of transmission. Ray tracing calculations show that a double Wollaston prism (Wu et al. 2009) enables $\sim \pm 17^\circ$ angles of incidence. For even larger angles of incidence, a cube beam-splitter is required. Cubes employing a wiregrid on the splitting interface can have an extinction ratio for the transmitted beam of $> 10^3$ across at least $\pm 30^\circ$ (Baur 2005). The reflected beam's extinction ratio, however, can be as low as 10, so an additional polarizer should be placed at the exit surface.

3.5.4 Spectrometer

When the modulation period approaches the spectral resolution of the spectrometer, the modulation contrast gets washed out, potentially leading to large efficiency reductions. For example, on the blue side of the spectrum, where the modulation period is smallest (see Fig. 3.1), the modulation amplitude is reduced to 60% in the SPEX instrument (see Section 3.6.1 for details). This has a similar effect on the polarimetric signal to noise ratio as a reduced instrument transmission of $T = 0.36$. Therefore, spectral smearing needs to be taken into account in the instrument design to ensure a sufficient signal to noise ratio.

3.5.5 Diattenuation

The transmission at an interface between two materials at normal incidence is dependent on their refractive indices $n_{1,2}$ according to:

$$T = 1 - \left(\frac{n_1 - n_2}{n_1 + n_2} \right)^2. \quad (3.19)$$

If one of the materials is birefringent, the transmission along its ordinary axis is different from the extraordinary axis, a phenomenon called diattenuation. This is effectively a partial polarizer, and can be modeled using Eq. (3.16). The application of an anti-reflection coating increases the total transmission and reduces the diattenuation, as can be modeled using the equations in Section 3.6.3.

If the quarter-wave retarder is implemented as a (superachromatic) waveplate, diattenuation creates $\sim 3 \cdot 10^{-4}$ instrumental polarization along Q (Beckers 1971, Frecker & Serkowski 1976). Polarization and hence diattenuation along the axes of the multiple-order retarder is not modulated, so it is not measured as instrumental polarization. However, the differential transmission along $\pm U$ makes the polarization out of the multiple-order retarder slightly elliptical, with the axes rotated away from $\pm Q$. The resulting modulation amplitude is given by:

$$A = \sin \left(2 \arctan \sqrt{\frac{T_{+U}}{T_{-U}}} \right), \quad (3.20)$$

which deviates from 1 by an amount of $\sim 6 \cdot 10^{-8}$ for a typical birefringent crystal.

3.5.6 Stress birefringence

Stress in an optical component induces birefringence, and thus acts as a retarder. The polarimetric impact depends on the amount of stress and the orientation; stress along the optical axis has no effect (at normal incidence). Three sources of stress are distinguished:

- Inherent stress in glass due to uneven shrinking in the annealing process. High quality glass typically contains less than 4 nm/cm intrinsic birefringence (Schott 2011), with a random orientation. If the quarter-wave retarder

is implemented as a BK7G18 Fresnel rhomb with a 3 cm path length, stress birefringence can add up to 0.03 waves retardance at 400 nm. In the worst case that the stress is aligned with one of the Fresnel rhomb's axes, this causes a reduction of the modulation amplitude for U of $\lesssim 0.02$.

- Clamping stress. A clamping force of 0.1 N applied over an area of 25 mm², as is the case for the SPEX instrument (Lemmen 2009), induces 0.004 N/mm² stress. The amount of birefringence per unit stress is described by the stress optical coefficient, which for BK7G18 is $2.77 \cdot 10^{-6}$ mm²/N (Schott 2013). The resulting worst case modulation amplitude reduction for U due to clamping stress in the Fresnel rhomb is $\lesssim 2 \cdot 10^{-5}$.

Clamping stress in the multiple-order retarder that is aligned with its axes has no polarimetric impact (see Section 3.5.2). Stress along the quarter-wave retarder axes only reduces the modulation amplitude of U (see Section 3.5.1). Stress at intermediate angles affects both Q and U . For the athermal multiple-order retarder combination of Al₂O₃ and MgF₂ crystals, as described in Section 3.6.1, the stress optical coefficients are $0.74 \cdot 10^{-6}$ mm²/N for Al₂O₃ (Jeppeesen 1958), and for MgF₂ a value could not be found, so it is assumed to be similar to that of Al₂O₃. A total thickness of 3 mm results in a maximum reduction of the modulation amplitudes for U of $\sim 2 \cdot 10^{-10}$, and for Q it is even better.

Clamping stress in the polarizer that is aligned with its own axes or with the multiple-order axes has no polarimetric impact. Stress at intermediate angles affects both Q and U by the same negligible amount.

- Thermal stress. Thermal expansion changes the forces on the optics, and hence the stress birefringence in the optics. This is a dynamic error, and will be included in Section 3.6.

3.6 Dynamic errors

Dynamic errors are the errors that are still present after calibration, and therefore limit the instrument's performance. In this section, the dynamic effects of temperature, non-normal incidence, and detection errors, as presented in Table 3.1, are explained in more detail.

3.6.1 Temperature

Most of the optical components exhibit temperature sensitivity. Therefore, the instrument needs to be calibrated for the entire operational temperature range. After calibration, the uncertainty in the temperature of the instrument, assumed to be ± 0.5 K, translates into a dynamic thermal error.

Athermal multiple-order retarder

Birefringent retarders are known to be temperature sensitive, in particular thick ones such as the multiple-order retarder. However, crystals can be combined such as to have a temperature-compensated retardance (e.g. Snik et al. 2009, Mahler et al. 2011b). As shown in Table 3.1, the multiple-order retarder's thermal behavior is more critical than the retardance change at non-normal incidence, therefore, athermalization is performed.

The normalized retardance change with temperature T of a birefringent crystal is given by:

$$\gamma(\lambda) = \frac{1}{\delta(\lambda)} \frac{\partial \delta(\lambda)}{\partial T} = \frac{1}{d} \frac{\partial d}{\partial T} + \frac{1}{\Delta n(\lambda)} \frac{\partial \Delta n(\lambda)}{\partial T}, \quad (3.21)$$

which is the combined effect of a change in thickness d and a change in birefringence $\Delta n \equiv n_e - n_o$. An athermal set of crystals at wavelength λ_0 is obtained using the appropriate ratio of retardances, such that:

$$\frac{\partial \delta_{\text{tot}}(\lambda_0)}{\partial T} = \delta_1(\lambda_0) \gamma_1(\lambda_0) \pm \delta_2(\lambda_0) \gamma_2(\lambda_0) = 0,$$

with the \pm sign depending on the crystal axes being parallel or perpendicular, respectively (Hale & Day 1988). Crystals mostly have $\gamma < 0$, i.e. the absolute retardance decreases with temperature, so an athermal combination requires that the fast axes are crossed. An athermal combination of a positive and a negative crystal is particularly interesting, because that also exhibits a stable retardance at non-normal incidence, as will be shown in Section 3.6.2.

For example, a subtractive set of MgF_2 and Al_2O_3 with a retardance ratio of 2.9 : 1 is athermal at 600 nm (Snik et al. 2009, Ghosh 1998). The residual temperature sensitivity at 400 nm is $3 \cdot 10^{-4} \mu\text{m}/\text{K}$ for a total retardance of $25 \mu\text{m}$. It follows from Eq. (3.1) that this change $\Delta \delta$ in multiple-order retardance induces an apparent change $\Delta \phi_L$ in the angle of linear polarization, according to:

$$\Delta \phi_L = \frac{\pi}{\lambda} \Delta \delta, \quad (3.22)$$

which is $0.14^\circ/\text{K}$. This error propagates to the degree of linear polarization P_L via the ϕ_L -dependent efficiency correction, according to:

$$\frac{\Delta P_L}{P_L} \leq 2 (A_Q - A_U) \Delta \phi_L, \quad (3.23)$$

where $A_Q - A_U$ is the difference in normalized modulation amplitudes for Q and U , which is on the order of 0.01 (see Table 3.1). This results in a maximum polarization error due to residual thermal sensitivity in the athermal multiple-order retarder of $5 \cdot 10^{-5}/\text{K}$. For comparison, a single MgF_2 retarder yields $\Delta \phi_L \lesssim 0.45^\circ/\text{K}$ and $\Delta P_L/P_L \lesssim 2 \cdot 10^{-4}/\text{K}$.

Thermal defocus

Thermal expansion of the spectrograph causes defocus and hence a decrease in modulation contrast. The modulation amplitude A for a spectral resolution element size of $\Delta\phi$, expressed in radians of the local modulation pattern, is given by:

$$A(\Delta\phi) = \frac{1}{\Delta\phi} \int_{-\Delta\phi/2}^{\Delta\phi/2} \cos \phi \, d\phi = \text{sinc} \frac{\Delta\phi}{2}. \quad (3.24)$$

For example, the static spectral smearing error as shown in Fig. 3.2 is the result of a spectral resolution of ~ 3 nm at a modulation period of ~ 6 nm, i.e. $\Delta\phi \approx \pi$, and hence $A \approx 0.6$.

Suppose that the modulation is sampled by 10 pixels with a width of $8 \mu\text{m}$, then the physical width of one modulation period on the detector is $80 \mu\text{m}$. An aluminum spectrograph with a thermal expansion coefficient of $23 \cdot 10^{-6}/\text{K}$ and a focal length of 60 mm defocuses by an amount of $1.4 \mu\text{m}/\text{K}$ (Lide 2005). For a focal ratio of $f/3$, this translates into a thermal spot size change at the detector of $0.5 \mu\text{m}/\text{K}$. This translates into a change of modulation amplitude with temperature of $\lesssim 7 \cdot 10^{-3}/\text{K}$.

It is possible to design a spectrometer such as to have an athermal focus. For example, the expansion of the aluminum can be compensated by the change in focal length of the camera lens, due to the temperature dependence of its refractive index. Alternatively, the spectrometer can be made of Invar, a material with an extremely low thermal expansion, or an all-aluminum reflective spectrometer can be used, such that the focal length scales with the expansion of the instrument. For the simulations in this paper, a partially athermalized spectrometer is used that reduces the thermal modulation amplitude change by a factor of 10.

Thermal stress birefringence

Finite element analysis shows that thermal expansion changes the stress on the optics typically by a rate similar to the static clamping stress, i.e. $0.004 \text{ N}/\text{mm}^2/\text{K}$ (Lemmen 2009). This causes a reduction of the modulation amplitude for U of $\lesssim 2 \cdot 10^{-5}/\text{K}$ (see Section 3.5.6).

Thermal dark current noise

Dark current typically doubles for every 7K temperature increase. For a typical dark current at room temperature of $0.5 \text{ e}^-/\text{s}$ and an operational temperature range of $\pm 20 \text{ K}$, the dark current at the highest temperatures is $\sim 4 \text{ e}^-/\text{s}$. The corresponding Poisson noise for a 1 s exposure is $\sim 2 \text{ e}^-/\text{s}$, which is negligible compared to the shot noise (see Section 3.6.4).

3.6.2 Non-normal incidence

The effect of non-normal incidence is twofold: the amount of retardance changes for both retarders, and instrumental polarization is created at all interfaces. The

corresponding errors are mainly static, but in the case of inhomogeneous illumination a dynamic component arises from the uncertainty about the exact angle of incidence within the instantaneous fields-of-view. Calculations are performed for a $\pm 15^\circ$ slit along $-Q$ with a pixel size of $0.25 \times 0.25^\circ$.

Fresnel rhomb at non-normal incidence

A Fresnel rhomb exploits the effect that a total internal reflection induces a phase shift between polarization in the plane of the reflection and perpendicular polarization. By carefully selecting the angle θ_0 of the reflecting surface, a quarter-wave retardance is obtained (for most materials with moderate reflective index n only after two reflections), according to (Keller 2002):

$$\delta(\theta) = 2 \arctan \left[\frac{\cos \theta \sqrt{n^2 \sin^2 \theta - 1}}{n \sin^2 \theta} \right] \frac{\lambda}{2\pi}. \quad (3.25)$$

Hence, the retardance of a Fresnel rhomb is intrinsically dependent on the angle of incidence.

If the angle of incidence is aligned with the plane of internal reflections, this angle –after refraction upon entering the rhomb– directly changes the angle of the total internal reflection. However, in the case that the slit direction is perpendicular to this plane, as is the case for SPEX, the angle of incidence on the tilted rhomb surface hardly changes. Decomposition of the angle of incidence into an angle α_0 parallel to the plane of reflections (along Q), and an angle β_0 perpendicular to the plane (along $-Q$) yields the following equation for the angle of the total internal reflection:

$$\theta(\alpha, \beta) = \arccos \left[\sin \theta_0 \sin \alpha + \cos \theta_0 \sqrt{\frac{1}{2} (\cos 2\alpha + \cos 2\beta)} \right], \quad (3.26)$$

with:

$$\sin \alpha_0 = n \sin \alpha, \quad (3.27)$$

$$\sin \beta_0 = n \sin \beta. \quad (3.28)$$

At the edge of the slit, i.e. $\alpha_0 = -0.125^\circ$ and $\beta_0 = 15.125^\circ$, the reduced quarter-wave retardance leads to a static reduction of the modulation amplitude for U of $\lesssim 10^{-4}$. The corresponding dynamic error in U is $\lesssim 10^{-5}$.

Widefield multiple-order retarder

A light wave entering the multiple-order retarder at a non-normal angle θ experiences a different retardance, partly because of the longer path through the crystal, and partly because the propagation direction is no longer perpendicular to the crystal's optic axis, which leads to a reduced effective birefringence. The impact of the

latter effect depends on the azimuthal angle ϕ of the incoming light with respect to the crystal axis. For $\phi = 0$, the absolute retardance decreases, because polarization along the extraordinary crystal axis is tilted towards the ordinary optical axis, whereas for $\phi = 90^\circ$, polarization is tilted from ordinary to extraordinary axis, so the absolute retardance increases because of the increased path length. In the intermediate case of a rectangular field-of-view along $\phi = 45^\circ$, as is the case for SPEX, the non-normal incidence effect almost vanishes. The multiple-order retardance at non-normal incidence is given by (Evans 1949):

$$\delta(\theta, \phi) = d \left[n_e \sqrt{1 - \frac{\sin^2 \theta \sin^2 \phi}{n_e^2} - \frac{\sin^2 \theta \cos^2 \phi}{n_o^2}} - n_o \sqrt{1 - \frac{\sin^2 \theta}{n_o^2}} \right]. \quad (3.29)$$

The main static effect is a spectral shift of the modulation pattern at non-normal incidence, which leaves no error after calibration. A static error does arise from the averaging over mutually shifted modulation patterns within an instantaneous field-of-view. It can be shown, using a calculation analogous to Eq. (3.24), that this smearing leads to reduced modulation amplitudes of:

$$A = \text{sinc} \frac{\pi}{\lambda} \Delta \delta, \quad (3.30)$$

where $\Delta \delta$ is the retardance change across a field-of-view element. At the edge of the slit, this static reduction is $\lesssim 3 \cdot 10^{-5}$.

The dynamic error in the angle of polarization, according to Eq. (3.22), propagates to the degree of polarization according to Eq. (3.23). For a single MgF_2 plate with $\delta = 25 \mu\text{m}$, these dynamic errors are $\Delta \phi_L \ll 0.9^\circ$ and $\Delta P_L \ll 3 \cdot 10^{-4}$ at the edge of the slit. The dynamic errors are upper limits, because they represent the worst case scenario that all rays entering a pixel come from the edge of the instantaneous field-of-view, with a worst case angle of linear polarization of $\phi_L = 22.5^\circ$, and a worst case degree of polarization of $P_L = 1$.

For the SPEX instrument described in this paper, the effect of non-normal incidence on the multiple-order retardance is smaller than the retardance change with temperature (see Section 3.6.1). Therefore, an athermal crystal combination was designed. However, in the case of a longer slit or a 2-dimensional field-of-view, it may be beneficial to minimize the retardance change at non-normal incidence by combining a positive ($\delta_1 > 0$) and a negative ($\delta_2 < 0$) crystal (Hale & Day 1988). The combined field-of-view behavior is given by:

$$\delta_{\text{tot}}(\theta, \phi) = \delta_1(\theta, \phi) \pm \delta_2 \left(\theta, \phi - \frac{\pi}{4} \pm \frac{\pi}{4} \right), \quad (3.31)$$

with \pm depending on the crystal axes being parallel or perpendicular, respectively. The multiple-order retardance at non-normal incidence is shown in Fig. 3.3 for the athermal set of Section 3.6.1, as well as for two other combinations of MgF_2 (positive birefringence) and Al_2O_3 (negative birefringence), optimized such as to have minimum retardance change at non-normal incidence. For a single retarder, the

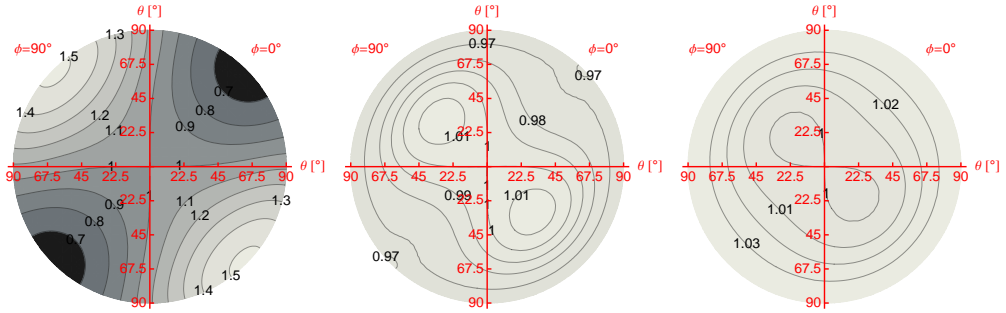


Figure 3.3: Normalized multiple-order retardance at non-normal incidence, for different combinations of MgF_2 and Al_2O_3 crystals. The center of the plots represents normal incidence, and the angle of incidence θ increases linearly with the radial distance. The azimuthal direction of incidence, with respect to the fast axis of the crystal combination, is denoted by ϕ . *Left:* Athermal combination (see Section 3.6.1). Crystal axes parallel. Thickness ratio $\text{MgF}_2:\text{Al}_2\text{O}_3$ of $d_r = 2.9 : 1$. *Center:* Widefield combination with crystal axes parallel. $d_r = 1 : 2.8$. *Right:* Widefield combination with crystal axes crossed. $d_r = 1 : 2.8$.

retardance across the field-of-view shows a distinct saddle shape (similar to the athermal combination in Fig. 3.3). This allows for two optimization options:

- The combination of a positive and a negative crystal with their crystal axes aligned (i.e. fast axes crossed) corresponds to adding up two saddles with opposite shapes. The result is a flat saddle, which has a particularly stable retardance at $\phi = 45^\circ$ with respect to the crystal axes, which is ideal for a long slit.
- A positive and a negative crystal with their crystal axes crossed (i.e. fast axes aligned) implies subtraction of two equally shaped saddles. The result is a flat, bowl shaped retardance, ideal for a 2-dimensional field-of-view.

Of the two widefield combinations, the best performance both in terms of angle of incidence and temperature is obtained with the crystal axes crossed, in the case of a $\pm 15^\circ$ slit. Its dynamic polarization errors due to angle of incidence are $\Delta\phi_L \ll 0.06^\circ$ and $\Delta P_L \ll 2 \cdot 10^{-5}$, but the thermal errors are $\Delta\phi_L \lesssim 1.7^\circ/\text{K}$ and $\Delta P_L \lesssim 6 \cdot 10^{-4}/\text{K}$.

Differential transmission

The transmission at an interface between two materials at non-normal incidence is different for polarization in the plane of incidence (denoted by p) than for perpen-

dicular polarization (s), according to the Fresnel equations:

$$T_s(\theta) = 1 - \left(\frac{\sin \theta_1 - \theta_2}{\sin \theta_1 + \theta_2} \right)^2, \quad (3.32)$$

$$T_p(\theta) = 1 - \left(\frac{\tan \theta_1 - \theta_2}{\tan \theta_1 + \theta_2} \right)^2, \quad (3.33)$$

$$(3.34)$$

combined with Snell's law:

$$\sin \theta = n_{1,2} \sin \theta_{1,2}, \quad (3.35)$$

where θ is the angle of incidence in air, and $n_{1,2}$ is the refractive index of the two materials. As a consequence, each interface acts as a partial polarizer, that can be described by Eq. (3.16). In the case of a slit along $-Q$, the differential transmission induces polarization along $-Q$.

Differential transmission at the entrance and exit surfaces of the quarter-wave retarder, and at the entrance of the multiple-order retarder, is modulated by the multiple-order retarder, and thus measured as instrumental polarization. The application of a magnesium fluoride anti-reflection coating reduces the differential transmission by $\sim 30\%$. The resulting instrumental polarization at the edge of a $\pm 15^\circ$ slit is $\sim 3 \cdot 10^{-3}$ per surface, i.e. $9 \cdot 10^{-3}$ in total. The total dynamic error in the instrumental polarization due to the inhomogeneous illumination is $\lesssim 9 \cdot 10^{-5}$.

3.6.3 Surface contamination

Contamination builds up on the optical surfaces over time, even in space, e.g. due to outgassing and venting (e.g. Green 2001, Schläppi et al. 2010). Assuming that the instrument is well designed, such that contamination inside the instrument is negligible, the first surface that is exposed to the environment will always collect a thin film. This changes the transmission properties, which for non-normal incidence also depends on the angle of polarization.

The polarization dependent transmission, taking into account multiple reflections and interference, in the case of ℓ thin layers (denoted by subscripts $j = 1, 2, \dots, \ell$) on top of a substrate ($j = 0$) in a medium (m) is described by Eq. (3.16) with (Macleod 2010):

$$c = \cos \left[\arg \left(\frac{t_p}{t_s} \right) \right]; s = \sin \left[\arg \left(\frac{t_p}{t_s} \right) \right], \quad (3.36)$$

and:

$$T_{s,p} = \frac{\eta_0}{\eta_m} |t_{s,p}|^2, \quad (3.37)$$

where $t_{s,p}$ is the complex transmission of the electric field vectors along s and p , given by:

$$t = \frac{2\eta_m}{\eta_m E_m + H_m}. \quad (3.38)$$

The polarization dependence enters with η , which is defined for polarization along s as:

$$\eta_{j,m} = n_{j,m} \cos \theta_{j,m}, \quad (3.39)$$

and for p as:

$$\eta_{j,m} = \frac{n_{j,m}}{\cos \theta_{j,m}}, \quad (3.40)$$

where θ_j is related to the angle of incidence θ_m in the medium via Snell's law:

$$n_m \sin \theta_m = n_j \sin \theta_j. \quad (3.41)$$

The normalized electric and magnetic fields at the front interface in Eq. (3.38) are given by:

$$\begin{pmatrix} E_m \\ H_m \end{pmatrix} = \mathbf{L} \begin{pmatrix} 1 \\ \eta_0 \end{pmatrix}, \quad (3.42)$$

respectively, where \mathbf{L} is the total characteristic matrix for all thin films, according to:

$$\mathbf{L} = \mathbf{L}_\ell \mathbf{L}_{\ell-1} \dots \mathbf{L}_1. \quad (3.43)$$

The characteristic matrix of each individual layer is described by:

$$\mathbf{L}_j = \begin{pmatrix} \cos \delta_j & \frac{i}{n_j} \sin \delta_j \\ i n_j \sin \delta_j & \cos \delta_j \end{pmatrix}, \quad (3.44)$$

where the phase delay δ_j as a function of the layer thickness d_j is given by:

$$\delta_j = \frac{2\pi}{\lambda} n_j d_j \cos \theta_j. \quad (3.45)$$

Several studies have derived the amount and type of contamination onboard a spacecraft, either by modeling the transmission loss in optical systems (Krijger et al. 2014, McMullin et al. 2002), or using in-situ (Wood et al. 2003) or on-ground measurements after return to Earth (Hemminger 1992). The studies involve a variety of spacecraft at different altitudes, leading to very different results. The platform envisioned for SPEX would be most similar to Envisat, which was investigated using the scan-angle dependent-degradation in SCIAMACHY, showing a silicone oil contamination layer with a thickness of 0.4 nm (Krijger et al. 2014). However, layer thicknesses in the order of ~ 10 nm as found in the other references can not be excluded.

Silicone oil, with a refractive index of $n \approx 1.45$, is often the main contaminant (Gelest 2012). In the case of a single-layer MgF_2 anti-reflection coating on the Fresnel rhomb, a 0.4 nm layer of oil changes the instrumental polarization at 15° angle of incidence by $\lesssim 2 \cdot 10^{-5}$, whereas for a 10 nm layer this is $\lesssim 6 \cdot 10^{-4}$. If the Fresnel rhomb is uncoated, these dynamic errors are smaller, namely $\lesssim 10^{-7}$ and $\lesssim 6 \cdot 10^{-5}$, respectively. The change in the quarter-wave retardance and the corresponding modulation amplitude reduction for U are negligible.

3.6.4 Detection errors

The polarimetric noise level is ideally limited by the total signal to noise ratio in a spectral demodulation frame, or any larger spectral band. A polarimetric noise of 10^{-n} requires a signal to noise ratio of 10^n , which requires the detection of at least 10^{2n} photons per modulation cycle according to Poisson statistics. In the end-to-end simulations in Section 3.7, a polarimetric noise of $2.5 \cdot 10^{-4}$ is tolerated in a 20 nm spectral band, that is sampled by 40 pixels with full-well depths of 10^5 electrons. On average, the spectral modulation pattern fills half of the full-well depth, so 8 co-addings are required to reach the signal to noise ratio of 4000. A typical readout noise of 10 electrons per pixel per co-adding is a minor effect compared to the photon noise. Assuming a total integration time of 1 second, a dark current of 0.5 electrons is typically collected per pixel. Dark current typically doubles for each 7 K temperature increase, so in the case of an operational temperature range of 40 K, the maximum dark current per pixel is 4 electrons. The corresponding dark current noise is 2 electrons, which is negligible compared to the photon noise of 4000 electrons.

In the end-to-end simulations in Section 3.7, it is assumed that detector non-linearity can be calibrated to within 10^{-3} . For fully polarized light, when the modulation pattern covers the entire full-well range, this induces spurious depolarization of $\lesssim 3 \cdot 10^{-4}$. Residual flat-fielding errors leave pixel-to-pixel variations in the gain. For relative gain errors of 10^{-3} , a polarimetric error of $4 \cdot 10^{-4}$ is induced, independent of the degree of linear polarization.

3.7 End-to-end simulation

Based on the analysis of error sources and their mathematical descriptions, as described in the previous sections, it is now possible to perform an end-to-end error propagation. In these Monte Carlo simulations, the error in a measured degree of linear polarization is composed of the following components:

- *Calibration errors.* The instrument calibration implies the measurement of fully polarized light at $0, 10, \dots, 170^\circ$, as well as unpolarized light. The calibration polarizer is mounted in a high-precision rotation stage, leaving a random angular error of $\pm 0.05^\circ$. The degree of linear polarization of the generated unpolarized light is uncertain at the $5 \cdot 10^{-4}$ level (see paper II (Rietjens et al. 2014)), and it can have any polarization angle. Each calibration measurement is subject to random detection errors, due to shot noise, readout noise, and residual non-linearity (see next item for details).
- *Detection errors.* The measurement of the light under study is also subject to random detection errors. Shot noise is the main contributor, with a total signal-to-noise ratio of 4000 over all pixels that comprise the 10-nm-wide spectral demodulation window. Read noise is a factor 20 smaller, and dark current noise is negligible. A random residual non-linearity is adopted such as to

reduce the highest intensities by $\sim 0.1\%$. Also, residual pixel-to-pixel gain variations of $\sim 0.1\%$ are adopted.

- *Instrument changes after calibration.* The instrument's response changes with temperature, it is dependent on the angle of incidence of the light, and it degrades over time due to surface contamination. For example, uncertainty in the temperature of ± 0.5 K causes uncertainty in the spectrograph focus, and hence in the modulation contrast. The retardance of the multiple-order retarder and stress birefringence also vary with temperature. Furthermore, in contrast to the homogeneous illumination that is applied during calibration, in real scenes it is uncertain from what exact angle inside the $0.25 \times 0.25^\circ$ instantaneous fields-of-view the light came. This causes uncertainty in the retardances of the quarter-wave retarder and the multiple-order retarder, and in the differential transmission at all interfaces. Contamination building up on the first surface changes the instrumental polarization at non-normal incidence. Since the amount of contamination is hard to estimate, a worst case scenario is adopted in the simulations, where the contamination can take on any thickness between 0 and 10 nm, on top of an uncoated Fresnel rhomb.

The effect of instrument changes alone, due to uncertainty in temperature, angle of incidence, and contamination, was demonstrated in Fig. 3.2, as the distribution of calibrated modulation amplitudes due to dynamic errors. The corresponding impact on polarization measurements is shown in Fig. 3.4, for unpolarized and fully linearly polarized input at 15° incidence. The baseline instrument is perfectly calibrated, before it is randomly perturbed 4000 times for changes in temperature, angle of incidence, and surface contamination, and subsequently employed for measurements without detection errors. Therefore, the obtained uncertainties are an absolute lower limit for the instrument's performance. The low errors for $I \rightarrow (Q, U)$ show that the instrument performance is not limited by uncertainty in the instrumental polarization. The uncertainty for fully polarized light is $\sim 5 \cdot 10^{-4}$, and it improves linearly with decreasing degree of polarization.

The impact of calibration errors alone on the polarimetric performance is assessed by simulating 4000 randomly perturbed calibrations. Each set of 19 calibration measurements (18 polarization angles and 1 unpolarized) is simulated as:

$$\mathbf{I}_{m \times 19} = \mathbf{O}_{m \times 4} \mathbf{S}^*_{4 \times 19}, \quad (3.46)$$

where the columns of matrix \mathbf{S}^* are filled with the Stokes vectors corresponding to the 19 supplied polarization states, including perturbations, and \mathbf{O} being the modulation matrix at the time of calibration (Sabatke et al. 2003). The measured intensities are randomly perturbed to \mathbf{I}^* afterwards to simulate detection errors. Subsequently, the modulation matrix is solved for, according to:

$$\mathbf{O}^* = \mathbf{I}^* \mathbf{S}^{-1}, \quad (3.47)$$

with \mathbf{S} containing the ideal input polarization states. For each of the 4000 simulated calibrations, the polarimetric impact is calculated by modulating the Stokes

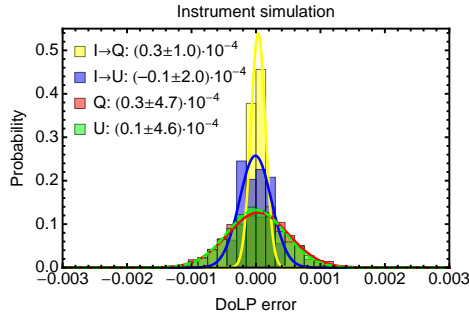


Figure 3.4: Error in determination of degree of linear polarization due to instrumental changes, for unpolarized (I) and fully polarized (Q , U) input. The distributions result from 4000 randomly perturbed instruments, according to the dynamic errors in Fig. 3.2.

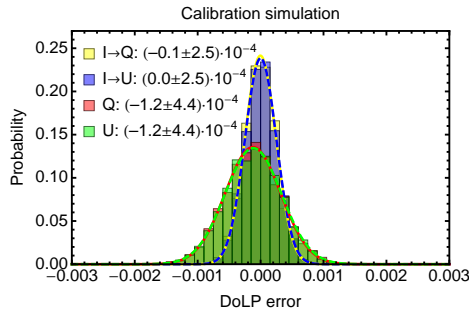


Figure 3.5: Error in determination of degree of linear polarization due to errors in the calibration, for unpolarized (I) and fully polarized (Q , U) input. The distributions result from 4000 randomly perturbed calibrations.

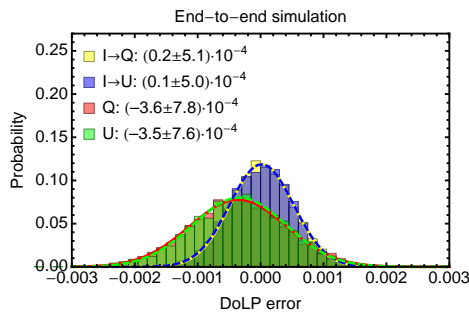


Figure 3.6: End-to-end simulation of errors in the determination of degree of linear polarization. The simulations are performed for unpolarized (I) and fully polarized (Q , U) input. The distributions result from 4000 randomly perturbed instruments, calibrations, and measurements.

vector under study using \mathbf{O} and demodulating using the inverse of \mathbf{O}^* . The resulting error due to imperfect calibration in the measured degree of linear polarization for unpolarized input, as well as fully polarized light at Q and U , is shown in Fig. 3.5.

On average, the Q and U errors appear slightly depolarizing, mainly due to detector non-linearity that reduces the modulation amplitudes. Note that the errors for 100% Q and U can be either positive or negative, because their baseline modulation amplitudes are well below 1 due to imperfections in the instrument. The widths of the error distributions are mainly determined by the random variations in the orientations of the calibration polarizer. Therefore, great care should be taken in the calibration setup to provide polarization at precise angles.

The errors for unpolarized light paradoxically mainly originate from the erroneous polarizer angles; the degree of polarization of the unpolarized calibration light has a minor effect. Its zero mean implies that imperfect calibration does not create spurious instrumental polarization.

Finally, end-to-end simulations are performed, including calibration errors, detection errors, and instrument changes after calibration. For each of the 4000 simulations, an instrument is constructed, including random misalignments, retardance offsets, and stress birefringence, which is described by modulation matrix \mathbf{O} . This instrument is calibrated like before, yielding \mathbf{O}^* . After calibration, random perturbations due to temperature, surface contamination and angle-of-incidence variations are included in \mathbf{O}^{**} to describe the instrument at the time of measurement. The Stokes vector under study is modulated using \mathbf{O}^{**} and demodulated using the inverse of \mathbf{O}^* , and measured including detection errors. The resulting error in the measured degree of linear polarization for unpolarized input, as well as fully polarized light at Q and U , is shown in Fig. 3.6.

The broadening of the error distributions compared to the case of calibration errors only is dominated by photon noise; the errors induced by temperature fluctuations and surface contamination are minor, as expected from Fig. 3.4; the effect of uncertainty in the angle of incidence is negligible. The probability of measuring degree of linear polarization with a calibrated SPEX satellite instrument with an error within ± 0.001 (± 0.002) is 86% (99.9%) for unpolarized light, and 76% (98%) for fully polarized light along either Q or U .

3.8 Conclusions

We presented a complete performance analysis for spectrally modulated linear polarimetry. An extensive overview of error sources is provided, and quantified in terms of their static impact on the polarimetry, and their dynamic errors after calibration. This enables the identification of the worst offenders, in particular shot noise, and the thermal stabilities of the spectrograph focus and the multiple-order retardance. The latter two effects can be athermalized in a passive way, using thermally compensating elements. We show that in-flight contamination of the first optical surface is likely a minor error source.

We provide mathematical descriptions of the errors in a general formalism for polarization modulation and demodulation, that allowed for the construction of a realistic instrument model. This model is finally employed to perform end-to-end Monte Carlo simulations of the combined performance of instrument and calibration. We find that the probability of measuring degree of linear polarization with an error within ± 0.001 (± 0.002) is 76% (99%) after calibration. This high accuracy and long-term stability is fully compliant with the requirement on the degree of linear polarization P_L of $0.001 + 0.005 \cdot P_L$ for atmospheric aerosol characterization from an orbiting platform, without the need for in-flight calibration.

Acknowledgements

This research was conducted within the framework of Prequalification ESA Programmes (PEP) and Mars Robotic Exploration Programme (MREP) grants from the Netherlands Space Office (NSO). GvH acknowledges Utrecht University for funding his research.

Chapter 4

Performance of spectrally modulated polarimetry II: Data reduction and absolute polarization calibration of a prototype SPEX satellite instrument

Spectral polarization modulation is a polarimetric technique that encodes the polarization state in a sinusoidal modulation in the intensity spectrum. A dual-beam version of this technique is implemented in SPEX, a prototype satellite instrument developed for aerosol characterization using multi-angle photopolarimetry, thereby providing snapshot measurements, with no moving or switching components. A complete end-to-end performance analysis for dual-beam spectrally modulated linear polarimetry was given in paper I of this series. In this second paper we present the data reduction techniques employed to extract the degree (P_L) and angle of linear polarization from SPEX measurements. Also, we present the absolute polarimetric calibration of SPEX, which shows a polarimetric sensitivity better than 10^{-4} and an absolute error smaller than $0.001 + 0.005 \cdot P_L$ after calibration of systematic differences between SPEX and a dedicated polarization stimulus. This makes SPEX, and spectral polarization modulation in general, a very promising concept for remote sensing and characterization of atmospheric aerosols, for which high polarimetric accuracy is required.

Rietjens, Van Harten, Bekkers et al. *Applied Optics*, To be submitted (2014)

4.1 Introduction

Highly accurate polarimetry is required for a number of demanding applications, both scientifically as well as commercially (Snik et al. 2014). Scientific examples include high contrast imaging for the detection of exoplanets and dust clouds, measuring solar and stellar magnetic field strengths, and characterization of dust in planetary atmospheres. The characterization of dust and cloud particles in the Earth's atmosphere is a priority for climate and air quality research. Commercial applications include contrast enhancement for target detection, food quality inspection, and human tissue characterization.

The polarimetric concept of choice is driven by the accuracy requirements of the application, and external constraints, e.g. in terms of mass, volume, complexity, and stability. Spectral polarization modulation is a type of channeled spectropolarimetry (Kudenov & Goldstein 2011) that is very suitable in cases where high polarimetric accuracy, instantaneous observations, and a moderate to high polarimetric spectral resolution are required (Nordsieck 1974, Oka & Kato 1999, Snik et al. 2009, van Harten et al. 2014c). A full theoretical analysis of the performance of polarimetry based on spectral linear polarization modulation has been presented in paper I of this series of two (van Harten et al. 2014b). This second paper is focussed on the SPEX instrument, a multi-angle linear spectropolarimeter that has incorporated spectral polarization modulation. In particular the data reduction techniques specifically employed for SPEX will be presented, as well as its absolute polarization calibration and overall performance. Performance limiting aspects will be discussed, and solutions for enhanced performance are presented.

This paper is organized as follows. In Section 4.2 we present the science case for the SPEX instrument, introduce spectral polarization modulation, and describe its implementation in the SPEX prototype instrument. Section 4.3 covers the data reduction pipeline that is used for extracting the polarimetric information in a SPEX measurement. In particular the demodulation algorithm is described in detail. The optical stimulus that was developed to calibrate the SPEX instrument is described in Section 4.4 as well as its characterization and zero-point measurement. Section 4.5 covers the calibration of SPEX with the aforementioned stimulus. The absolute polarimetric calibration results are presented, and compared with the measured stimulus output, as well as with repeated calibration measurements. Also the polarimetric sensitivity of SPEX is presented. The calibration results are further discussed in Section 4.6 and performance limiting aspects as well as directions potentially leading to enhanced performance are given.

4.2 SPEX instrument

4.2.1 Scientific background and requirements

An important application for high-accuracy polarimetry is the characterization of aerosols and dust suspended in the Earth's atmosphere, in terms of their micro-

physical properties such as, size, shape, and complex refractive index – indicative of chemical composition. By measuring the radiance and polarization of the scattered sunlight in a number of spectral bands under different scattering angles, one can disentangle these microphysical properties (Hansen & Travis 1974, Mishchenko & Travis 1997). Global characterization of atmospheric aerosols is essential to better understand the weather and climate of a planet (Haywood & Boucher 2000, Ramanathan et al. 2001, Mishchenko et al. 2004). The polarimetric requirement for aerosol characterization is that the absolute error in the degree of linear polarization P_L is smaller than $0.001 + 0.005 \cdot P_L$ (Mishchenko & Travis 1997, Hasekamp & Landgraf 2007).

The only multi-angle polarimeter that has successfully flown in space is the POLDER instrument onboard the PARASOL satellite, which has been operational from 2004 until 2013 (Tanré et al. 2011). Part of its mission time was spent in the NASA A-train, a suite of satellites flying in formation to perform simultaneous measurements of, e.g., aerosols, clouds, and atmospheric chemistry (L'Ecuyer & Jiang 2010). Currently, a number of polarimeters are being developed for application in space:

- Multi-Viewing Multi-Channel Multi-Polarization Imaging Mission (3MI) is a widefield 2D-imaging polarimeter selected for EUMETSAT Metop Second Generation satellites (Manolis et al. 2013). It is built upon the POLDER heritage, using rotating filter wheels for the polarimetry and spectral sampling. The accuracy of the polarimetry is $\sim 1\text{--}2\%$.
- Aerosol Polarimetry Sensor (APS), the satellite version of the airborne Research Scanning Polarimeter (RSP), unfortunately failed on launch in 2011 (Peralta et al. 2007). A single ground pixel is observed over a large along-track angular range using a scanning mirror. Stokes Q and U are analyzed in separate refractive telescopes, using Wollaston prisms, followed by dichroic beam-splitters. The instrument is equipped with an in-flight calibration system, and has a demonstrated accuracy of better than 0.002 (Persh et al. 2010).
- Multiangle SpectroPolarimetric Imager (MSPI) is a pushbroom scanner that employs photoelastic modulators to modulate linear polarization at 25 Hz (Diner et al. 2005, 2007). The modulation pattern on each pixel describes both I and Q (or I and U , depending on the analyzer orientation), so the degree of polarization is independent of transmission. The accuracy of the polarimetry is better than 0.003.
- Passive Aerosol Cloud Suite (PACS) is a 2D-imaging polarimeter using a fish-eye lens (Martins et al. 2013, Fernandez Borda & Martins 2013). A modified Philips prism splits the beam according to three polarization angles (0, 60, and 120°), that are imaged onto three independent cameras, providing snapshot measurements.

In this paper we present the SPEX instrument that is developed for aerosol and dust characterization from an orbiting or airborne platform. It is a multi-angle push-

broom spectropolarimeter that has implemented spectral polarization modulation for measuring the state of linear polarization. Spectral polarization modulation has a number of advantages compared to other state of the art polarimeters when application in space is considered: snapshot measurements (instantaneous recording of radiance and state of linear polarization), no moving or active modulation optics, athermal, and compact.

4.2.2 Spectral polarization modulation

The principle of spectral polarization modulation is that the degree $P_L(\lambda)$ and angle $\phi_L(\lambda)$ of linear polarization of the incoming light are encoded into a sinusoidal modulation of the spectrum (see also (Snik et al. 2009, van Harten et al. 2014b)). Light entering the instrument first passes through a set of dedicated optical components: an achromatic quarter-wave retarder (QWR), an athermal multiple-order retarder (MOR) oriented at 45° , and a polarizing beam-splitter at $0/90^\circ$. After the polarization analysis, a refractive telescope and spectrometer follow.

Incident light linearly polarized along the $\pm Q$ direction is unchanged by the QWR, while light polarized along the $\pm U$ direction will be transformed into circular polarization. In this way, linearly polarized light in an arbitrary direction will be spectrally modulated in polarization state after passing the MOR due to its very chromatic nature (the retardance of the MOR is inversely proportional to the wavelength). The polarizing beam-splitter transforms the polarization modulated spectrum into two complementary intensity modulated spectra, according to:

$$\begin{aligned} S_{\pm}(\lambda) &= I_0(\lambda) S_{N_{\pm}}(\lambda) \\ &= \frac{1}{2} I_0(\lambda) \left[1 \pm P_L(\lambda) \cos(\psi(\lambda)) \right], \\ \psi(\lambda) &\equiv \frac{2\pi\delta(\lambda)}{\lambda} + 2\phi_L(\lambda). \end{aligned} \tag{4.1}$$

Here, the modulation amplitude $P_L(\lambda)$, retardance $\delta(\lambda)$, and modulation phase $\phi_L(\lambda)$ are all functions of wavelength, and the \pm represents the two complementary spectra that exit the polarizing beam-splitter. Since the two modulated spectra have a mutual π phase shift, their sum yields the incident radiance spectrum at the spectrograph's intrinsic resolution. The polarimetric spectral resolution is roughly equal to the local modulation period, which is equal to $\lambda^2/\delta(\lambda)$. A single measurement thus provides both the radiance and the state of linear polarization.

In principle, each spectrum out of the polarizing beam-splitter contains the full radiance and polarization information. However, a dual-beam implementation is essential for accurate polarimetry, by preventing aliasing of absorption features in the intensity spectrum with the modulation waves (Craven & Kudenov 2010). We use the redundancy in the modulation to extract differential transmission between the beams from the data itself (see Section 4.3). This dynamic transmission correction ensures high polarimetric accuracy and long-term stability, and could possibly obviate the need for in-flight calibration (van Harten et al. 2014c).

4.2.3 SPEX prototype instrument

The SPEX prototype instrument (hereafter referred to as SPEX (Snik et al. 2008, van Harten et al. 2011)) is a linear spectropolarimeter that employs spectral polarization modulation in the visible part of the spectrum. Nine fixed viewing apertures allow multi-angle observations of the same ground pixel, which enables sampling of the scattering phase functions of dust and cloud particles while flying over it. The optical and mechanical design and a picture of the realized instrument are shown in Figs. 4.1a–c.

Each viewport has its own set of polarization modulation optics. During the calibrations and performance characterizations in this paper, three out of the nine viewports were filled with optics. In each polarization modulator, the QWR is implemented as a Fresnel rhomb made of radiation resistant BK7G18, as this is the first optical component and is therefore exposed to the maximum amount of radiation when operating in a space environment. The MOR consists of an athermal combination of sapphire (Al_2O_3) and magnesium fluoride (MgF_2), with thicknesses of 1.22 mm and 2.88 mm, respectively, and a total retardance of $\sim 24.4 \mu\text{m}$. The polarizing beam-splitter is implemented as a Wollaston prism made of α -BBO, because a thermo-mechanical analysis showed that glued calcite Wollaston prisms would not survive the non-operational temperature range. A single suprasil lenslet focuses the two polarized beams onto two separated slits ($1.4 \times 0.2 \text{ mm}$, which are part of a common slit plate) corresponding to a field of view (FoV) of $1^\circ \times 7^\circ$. The placement of the polarization modulation optics in front of the lenslet minimizes instrumental polarization.

The different viewing directions are oriented at 0° , $\pm 14^\circ$, $\pm 28^\circ$, $\pm 42^\circ$ and $\pm 56^\circ$ along the flight direction with respect to nadir. Each pair of complementary spectra per viewing direction is focussed via a beam combiner onto the common slit plate. This slit plate forms the entrance slit of the spectrometer, which consists of a spherical collimating mirror, a folding flat, a transmission grating, and finally the imaging optics. A volume phase holographic transmission grating (fused silica substrate, line spacing of 750 lines per mm) is used as the dispersive element in the optical path, for reasons of compactness. Light enters the slit with a focal ratio of $F/10$, and is demagnified by the imaging lenses (two identical fused silica aspheres and an F2G12 lens) into $F/3.3$ in order to have a good match with the detector and the required spectral resolution of $2 - 3 \text{ nm}$.

While the optical design was optimized for a detector with 512×512 pixels and $25 \mu\text{m}$ pixel size, for the prototype instrument a commercial detector was purchased: a QImaging Retiga4000R camera with KODAK KAI-4021 interline CCD, with 2048×2048 square pixels of $7.4 \mu\text{m}$ in size. A simulated image of the spectra at the focal plane of the commercial detector is shown in Fig. 4.1d. There are 9 pairs of modulated spectra, one pair per viewing direction (S_\pm), as can be seen from the clear-sky measurement in Fig. 4.1e. The height of each spectrum in the vertical direction corresponds with the 7° FoV in the across track direction. The image is curved in two directions due to the spectral smile and spatial distortion.

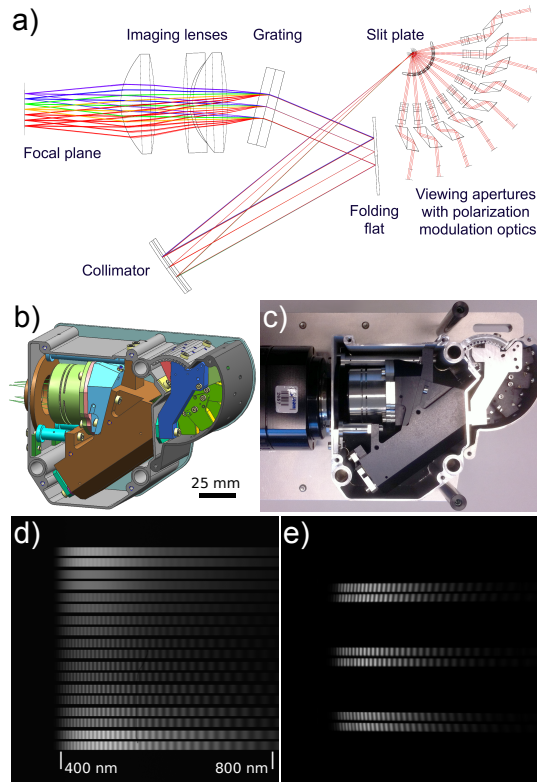


Figure 4.1: *a)* Optical design of the SPEX prototype showing the main optical components. *b)* Mechanical design drawing of the opto-mechanical unit of SPEX. The nine viewports are the green units on the right, the grating is mounted in the cyan compartment and the imaging lenses are embedded in the light green housing. The focal plane lies just outside the structure. *c)* Picture of the realization of SPEX showing the black anodized viewports on the right and the detector mounted to the structure on the left. *d)* Simulated focal plane image of a homogeneous scene (black surface, clear sky) as viewed by SPEX from space. The solar zenith angle is 60° . Polarization is clearly visible in most of the 9 times 2 spectra as a modulation of the intensity. *e)* Clear-sky image obtained with the SPEX prototype from the ground, showing a high degree of polarization in each of the three viewports that are equipped with polarization encoding optics.

4.3 Data reduction pipeline

4.3.1 Image processing

Each analysis of a given detector image starts with standard image processing steps.

First, a non-linearity correction is applied to the raw data, since non-linearity potentially leads to reduced maxima in the modulated spectrum, which results in

an underestimation of the modulation amplitude and thus of P_L . The non-linearity of the Retiga4000R was characterized by varying the integration time at constant illumination level. Quadratic fitting of the detector response as a function of exposure time showed an underestimation of the registered detector counts of $9\% \pm 1\%$ at full-well saturation. Consequently, signal levels above $\sim 70\%$ were avoided and a quadratic non-linearity correction was applied to the raw data. The uncertainty in the non-linearity correction leads to an estimated error in P_L of about $5 \cdot 10^{-4}$.

Second, a dark reference image taken at the same exposure time is subtracted. Dark subtraction is important since any offset added to a modulated spectrum effectively results in a reduced modulation amplitude and thus in an underestimation of P_L . However, in case both a reference measurement and a calibration or field measurement is taken at the same exposure time, both measurements suffer from the same underestimation, in which case the effect of the dark signal is fully compensated by the reference measurement (see Section 4.3.3). Furthermore, an uncorrected dark signal only leads to a relative polarimetric error: for unpolarized scenes, the polarimetric error due to a (residual) dark signal is zero. Therefore only a residual dark signal is expected to affect the P_L measurement, and most pronounced at high P_L . The dark signal of the Retiga4000R is typical 0.06% of the maximum signal in case of 16 co-additions and also contains accumulated read-out noise. The noise dominated residual dark (per pixel) is an order of magnitude less and due to averaging over a full modulation period, the resulting error in P_L is less than 10^{-4} in case of $P_L = 1$ and 5% average detector saturation level.

Third, a vertical smear correction is applied to each image. The detector shows vertical smear due to imperfect shielding of the dark interline columns, such that a fraction of the electrons keeps leaking from the illuminated columns into the dark shift registers during readout, leading to an offset that scales with the total signal in each detector column. This offset results in a polarimetric error similar to the effect of a dark signal. The vertical smear correction consists of subtracting a fixed profile from each detector row which is obtained by summing the signals in each detector column and scaling to the appropriate level. An integration time dependent scaling factor is used, which corresponds to $3 \cdot 10^{-6}$ for the integration times employed for most of the measurements in this work. The smear signal is typically a factor 2 larger than the dark signal, and therefore the error in P_L due to a residual smear signal is estimated to be of the order of 10^{-4} .

Flat-fielding of the image is important since variations in the pixel-to-pixel response lead to a noise-like pattern that can be interpreted as a modulation signal with a finite amplitude by the demodulation algorithm (see Section 4.3.3) even in case of fully unpolarized light. Flat-fielding can be achieved by dividing a measurement image by either a pixel response non-uniformity map of the detector, or by an image from a measurement in which SPEX is illuminated with unpolarized light ($P_L < 5 \cdot 10^{-4}$). In the present work, the latter option is used. The residual pixel-to-pixel gain variations are $\sim 10^{-3}$, causing polarimetric errors of $\sim 4 \cdot 10^{-4}$ (see paper I (van Harten et al. 2014b)).

A single detectable ghost at the illumination levels in the present work is present

in the spectral region below 400 nm and has no impact on the data reduction. Stray light is not explicitly corrected since a homogeneous illumination is used. In this case spectral stray light as well as spatial stray light within an S_+ or S_- band has a similar effect as a dark signal, which is compensated when using a reference measurement at the same illumination conditions. Cross-talk between the S_+ and S_- channels (maxima of S_+ filling minima of S_- and vice versa) is less than $2 \cdot 10^{-4}$.

To enable reliable extraction of two complementary spectra of a single viewport, spatial calibration measurements have been performed, using a stimulus that provides 0.6° FoV illumination. The illuminated traces on the detector have been used to map each pixel to a certain part of the FoV. Spectral calibration was performed by fitting the position of spectral lines from a Mercury Argon calibration source with a Gaussian line profile, and subsequent interpolation with a second-order polynomial in order to map each pixel to the correct wavelength. The widths of the fitted line profiles yield an average spectral resolution of ~ 2.6 nm.

4.3.2 Spectrum normalization

Prior to the demodulation of a modulated spectrum $S_{\pm}(\lambda)$ into a spectral amplitude and phase, this spectrum needs to be normalized by the radiance spectrum $I_0(\lambda)$. In order to obtain $I_0(\lambda)$, it is essential to correct for any transmission differences between $S_+(\lambda)$ and $S_-(\lambda)$. Differential transmission primarily arises from the different efficiency and transmission of the grating for s - and p -polarized light. The transmission correction is performed using one (or a combination) of the following methods:

- Using radiometric calibration data which converts detector binary units to physical units.
- Using a reference image obtained with an unpolarized source and dividing the measured spectra by the reference spectra.
- By applying a transmission correction algorithm on the measurement without relying on reference images or calibration. The algorithm is based on an iterative scheme that minimizes residual modulation in the sum spectrum ($S_+(\lambda) + S_-(\lambda)$). This procedure is explained in detail in (van Harten et al. 2014c).

The normalization procedure is visualized in Figs. 4.2a–d. The raw spectra $S_+(\lambda)$ and $S_-(\lambda)$ (Fig. 4.2a) exhibit differential transmission, for example on the red side of the spectrum where the modulation maxima of $S_+(\lambda)$ are noticeably higher than $S_-(\lambda)$. Division of $S_+(\lambda)$ by the transmission ratio curve of Fig. 4.2b yields the corrected spectra in Fig. 4.2c, as well as the smooth sum spectrum $I_0(\lambda) = S_+(\lambda) + S_-(\lambda)$. The normalized spectra $S_{N_{\pm}}$ are obtained by dividing $S_{\pm}(\lambda)$ by $I_0(\lambda)$. Since S_{N_+} and S_{N_-} are complementary, only S_{N_-} is plotted in Fig. 4.2d.

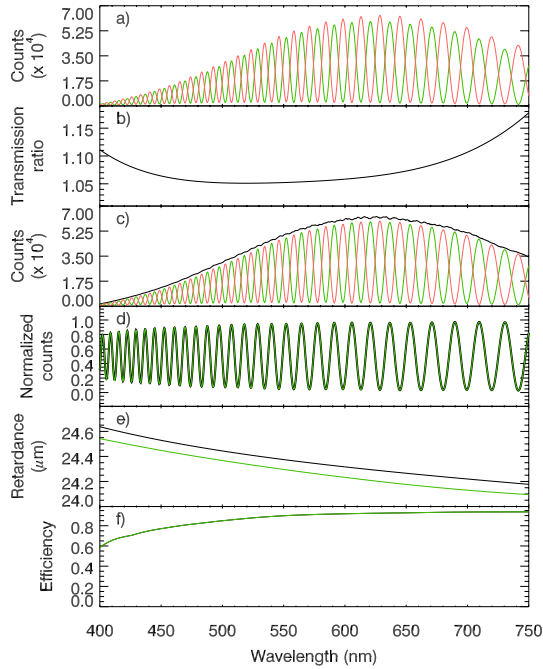


Figure 4.2: *a)* Dual spectra extracted from a SPEX lab measurement of fully polarized light: $S_+(\lambda)$ (red) and $S_-(\lambda)$ (green). *b)* Transmission ratio of $S_+(\lambda)$ with respect to $S_-(\lambda)$. *c)* Transmission corrected spectra of *a)*, and their sum spectrum (black). *d)* Normalized spectrum $S_{N-}(\lambda)$ (black), and the fit to Eq. (4.2) (green). *e)* Spectral retardance obtained from the fit to S_{N-} (green), and the theoretical retardance based on the nominal thicknesses of the crystal plates (black). *f)* Modulation efficiency obtained from the fit of S_{N-} .

4.3.3 Demodulation

The core of the demodulation process is the determination of the spectrally varying amplitude and phase of the normalized modulation pattern (see Fig. 4.2d). These parameters can be translated into a degree and angle of linear polarization once the maximum amplitude and absolute phase are calibrated.

The demodulation algorithm is based upon curve fitting in a moving spectral window, as opposed to e.g. Fourier analysis. The reason for this is mainly because, as a result of a grating as a dispersive element, the spectral sampling is equidistant in wavelength whereas the modulation period varies quadratically with wavelength. Moreover, using the curve fitting approach, one has full control over the fit function, to take into account non-ideal effects such as modulation pattern offsets and dispersion of the multiple-order retardance, or to allow for a linearly changing polarization at sub-window level.

Reference measurement

The first part of the demodulation process is aimed at determining the spectrally smooth multiple-order retardance $\delta(\lambda)$ and modulation efficiency $\epsilon_L(\lambda)$ through a set of calibration measurements.

Determination of the angle of linear polarization ϕ_L requires precise knowledge of $\delta(\lambda)$, because both are present in the argument of the cosine function in Eq. (4.1) and therefore one of the parameters needs to be constrained. To this end, a reference measurement is performed with a polarizer at a known angle ϕ_L , and the spectral retardance is determined by fitting the hence obtained normalized spectrum to a function of the form:

$$S_{N_{\pm}}(\lambda) = O(\lambda) \pm \frac{A(\lambda)}{2} \cos\left(\frac{2\pi\delta(\lambda)}{\lambda} + 2\phi_L\right), \quad (4.2)$$

where the offset $O(\lambda)$ is a free parameter to allow for non-idealities with respect to Eq. (4.1) that typically varies between 0.5 ± 0.005 , and $A(\lambda)$ is the modulation amplitude. The fit routine minimizes the least-squares difference between Eq. (4.2) and the normalized measured spectrum (Markwardt 2009). The functions $O(\lambda)$, $A(\lambda)$ and $\delta(\lambda)$ are all smooth functions of wavelength, so they can be approximated by a spline interpolation of ~ 15 independent points equidistantly distributed over the spectrum; the fit routine thus employs ~ 45 independent fit parameters. This approach is taken because it allows to constrain the retardance much better over the full spectrum than when using e.g. a moving window fit (see Section 4.3.3).

The retardance fit is plotted in Fig. 4.2e, together with the curve expected from the nominal plate thicknesses and the refractive indices of Al_2O_3 and MgF_2 as described by the Sellmeier equations (Ghosh 1998, Dodge 1984). The spectrally constant deviation of $\sim 0.4\%$ is attributed to a small difference in modeled and actual thicknesses of the crystal plates, since this difference is within the production tolerances. Note that a deviation from the nominal retardance does not cause polarimetric errors after calibration.

Besides the multiple-order retardance, this calibration also yields the efficiency $\epsilon_L(\lambda)$ with which $P_L(\lambda)$ is measured (see Fig. 4.2f), i.e. the modulation amplitude measured in case of fully linearly polarized incident light. The general shape of $\epsilon_L(\lambda)$ can be explained as follows. The efficiency is always smaller than 1, because the strong gradients in the modulation pattern are degraded by the slit function convolved with the point spread function and, to a lesser extent, finite sampling of the detector. This results in smearing of the modulation pattern, thereby reducing its amplitude. The deviation is largest at lower wavelengths, because of the higher modulation frequency. Furthermore, stray light adds an offset to the spectra and effectively reduces the modulation amplitude.

The measured $\epsilon_L(\lambda)$ is used to convert any observed modulation amplitude $A(\lambda)$ into a calibrated $P_L(\lambda)$ via:

$$P_L(\lambda) = A(\lambda) / \epsilon(\lambda). \quad (4.3)$$

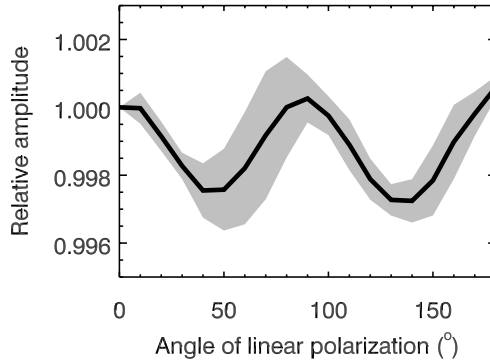


Figure 4.3: Relative modulation amplitude for fully polarized light with varying angle of linear polarization. The black line is the spectral average, while the grey area represents the 1σ variation.

Since deviations from perfect quarter-wave retardance of the QWR and small misalignments of the QWR and MOR with respect to each other and to the polarizing beam-splitter result in a reduced modulation amplitude that can be different for Stokes Q and U (van Harten et al. 2014b), the modulation amplitude needs to be measured as a function of angle of linear polarization. The normalized amplitude is plotted as a function of polarizer orientation in Fig. 4.3, which shows the spectral average as well as the 1σ variation across the spectrum. Clearly, the modulation amplitude variation is very small: on average the amplitude of Stokes Q is 0.002–0.003 higher than that of Stokes U . The magnitude and direction of this difference indicate a retardance deviation in the Fresnel rhomb, probably due to inherent stress birefringence (van Harten et al. 2014b). The magnitude of this difference is at least an order of magnitude larger than expected from deviations from quarter-wave retardance resulting from production tolerances. In a previous paper (van Harten et al. 2011) a much larger variation in the opposite direction was reported: the modulation efficiency for Stokes U was 0.01–0.015 higher than that of Stokes Q , which was attributed to a misalignment between the QWR and the MOR. The improved performance is attributed to an enhanced alignment after reintegration of the polarization optics that occurred prior to the measurements reported here. The variation of $\epsilon_L(\lambda)$ with angle of linear polarization and wavelength is taken into account when converting any observed modulation amplitude into a calibrated $P_L(\lambda)$.

Measurement demodulation

After having obtained the multiple-order retardance and modulation efficiency from the reference measurements, the spectral degree and angle of linear polarization of, e.g., a calibration or field measurement can be determined. To this end, the normalized spectrum $S_{N_-}(\lambda)$ is demodulated by calculating A and ϕ_L in a moving window, i.e. a spectral region equal to the local modulation periodicity. The width

of a spectral window $\Delta\lambda$ at wavelength λ is obtained from the spectral retardance using $\Delta\lambda \approx \lambda^2/\delta(\lambda)$. Note that, in contrast to the demodulation of the reference measurements, the polarization is not assumed to be spectrally smooth. The normalized spectrum within each spectral window is fitted with Eq. (4.2). The spectrally dependent retardance $\delta(\lambda)$ is supplied to the fit routine, while the free fit parameters $O(\lambda)$ and $\phi_L(\lambda)$ are assumed to be constant throughout a spectral window. The modulation amplitude $A(\lambda)$ is allowed to change linearly with wavelength within a spectral window, via $A(\lambda) = A_0 + c(\lambda - \lambda_0)$, where λ_0 represents the central wavelength of the spectral window. After a successful demodulation procedure, the modulation amplitude $A(\lambda)$ is divided by the measured efficiency $\epsilon_L(\lambda)$ from the reference measurement in order to obtain the degree of linear polarization $P_L(\lambda)$, according to Eq. (4.3).

An example of a measurement and demodulation of $\sim 10\%$ polarized light is shown in Fig. 4.4. The partial polarization is created with the calibration stimulus described in Section 4.4. Figure 4.4a shows the dual modulated spectra after transmission correction, along with the sum spectrum. Figure 4.4b shows one of the spectra after normalization, as well as the result of fitting Eq. (4.2) in a moving spectral window, as obtained during demodulation. The corresponding fit residuals, with a standard deviation of $\sigma = 7 \cdot 10^{-4}$, are shown in Fig. 4.4c. The residuals show artefacts of magnitude $< 1.5 \cdot 10^{-3}$ where variations in the intensity spectrum have a similar width as the local modulation period. At these spectral positions the transmission correction is most likely not optimal. Note however that the average residual over a modulation period is much less than 10^{-3} , which also applies for wavelengths above 700 nm, where the residuals are dominated by shot noise. The determined spectral modulation amplitude and the degree of linear polarization after correction for the measurement efficiency are displayed in Fig. 4.4d. Note that the ± 0.01 -wiggle in the polarization spectrum is real: it is caused by an anti-reflection coating, which is verified by an independent polarimeter (see Section 4.4.3).

4.4 Polarization calibration stimulus

4.4.1 Optical design

For absolute polarimetric calibration of the SPEX prototype, an efficiency correction obtained from a measurement with fully linearly polarized light is not necessarily sufficient, since zero-point effects (e.g. instrumental polarization or spurious signals that mimic a polarization signal) can cause deviation from linearity at small degrees of linear polarization. Therefore, and in order to determine the sensitivity of SPEX, a dedicated polarization stimulus is developed that can produce light with a well defined state of linear polarization in the range $0 \leq P_L \lesssim 0.5$. The accuracy and reproducibility of this stimulus must be better than the required calibration levels. The requirements defined for this stimulus are as follows:

- The stimulus shall generate white light (400–750 nm) with a degree of linear

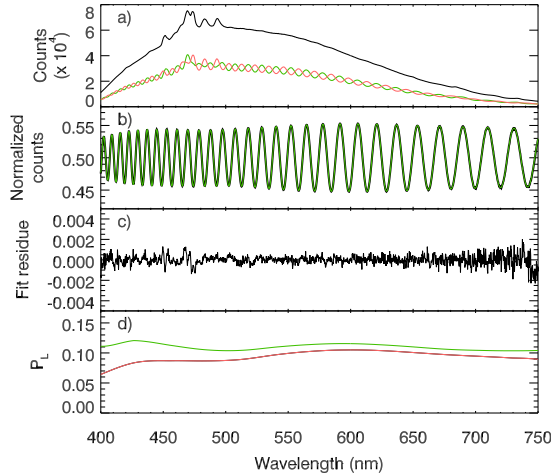


Figure 4.4: *a)* Dual spectra extracted from a SPEX lab measurement with partially polarized light: transmission corrected $S_+(\lambda)$ (red) and $S_-(\lambda)$ (green), and their sum spectrum (black). *b)* Normalized spectrum $S_{N-}(\lambda)$ (black), and the fit to Eq. (4.2) (green). *c)* Residuals of the fit in *b)*. *d)* Modulation amplitude obtained from the fit of S_{N-} (red), and the degree of linear polarization P_L after efficiency correction (green).

polarization of $0 \leq P_L \lesssim 0.5$ that can be set with an accuracy better than $0.001 + 0.005 \cdot P_L$.

- The stimulus shall provide light at the exit pupil over a field range larger than the 7° FoV of SPEX.
- The exit pupil of the stimulus shall be larger than the 1.1 mm diameter entrance pupil of SPEX.

A schematic of the stimulus that was developed according to these requirements is shown in Fig. 4.5. The stimulus consists of an unpolarized light source, a set of tiltable glass plates to introduce polarization, and a lens in order to create sufficient FoV illumination of 10° , and at the same time an oversized exit pupil (3.5 mm diameter). We have adopted an approach to use as few components as possible, since these can all introduce polarization at non-zero angles of incidence. Moreover, the very slow optical system limits the angles of incidence on optical components, thereby minimizing polarization that is not introduced by the glass plates, and maximizing the alignment tolerances of the stimulus components and of SPEX with respect to the stimulus. This approach is similar to Mahler & Chipman (2011), with the main differences that an integrating sphere is used as light source instead of a light pipe and depolarizer, and instead of a half-wave plate a cradle is used to change the angle of linear polarization.

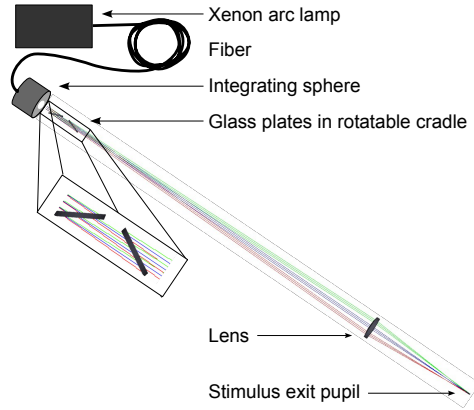


Figure 4.5: Schematic layout of the polarization calibration stimulus. The distance from integrating sphere to exit pupil is 175 cm.

4.4.2 Depolarization and partial polarization

The calibration stimulus first thoroughly depolarizes the light source, before a controllable partial linear polarization state is created. Thorough depolarization is needed because lamp polarization and fluctuations therein will otherwise leak through the setup since the stimulus is only a partial polarizer. Also, the ability of the stimulus to generate light with very low degree of polarization will enable the zero-point calibration of SPEX. To achieve a very low level of polarization, the output of a Xenon light source is coupled into an integrating sphere using an optical fiber. The output of the Xenon light source is typically polarized by a few percent. The integrating sphere is expected to depolarize the light by a factor of < 0.005 (McClain et al. 1994). The output of the integrating sphere is therefore expected to be unpolarized to within 10^{-4} .

Two glass plates are used to reintroduce polarization in a controllable fashion. The glass plates are tilted in opposite directions to counteract displacement of the beam, to increase the maximum P_L that can be created, and to reduce sensitivity to tilt-errors and to oblique rays in the beam (an angle of incidence error of $+\Delta\phi$ on the first glass plate becomes $-\Delta\phi$ on the second plate). The range in obtainable P_L increases with the refractive index of the glass. Also, calculations show that the sensitivity to tilt errors at a given $P_L \gtrsim 0.20$ is lower when using high-refractive index glass at small angles compared to using lower index glass at larger tilt angles, mainly because the derivative of P_L versus tilt angle increases with the tilt angle. Therefore, Schott P-SF57 with a high refractive index of ~ 1.85 has been selected. The glass plates are mounted onto a rotating cradle setup, which rotates the glass plates around the optical axis, in order to set the angle of linear polarization.

The glass plates are coated on one side with anti-reflection coating, in order to prevent multiple internal reflections that lead to a less predictable polarization

due to interference effects and a dependence of the polarization on the number of reflections and hence on beam-shift. The coating is applied on the exit surfaces, such that most of the reflected light will be reflected on the first surface and therefore never enter the glass plates. The manufacturer's specification of the coating was a spectrally averaged reflectance of less than 0.5%. The maximum degree of linear polarization that the stimulus can achieve is about 47%, corresponding to glass plate angles of 70° . Beyond this angle part of the beam will be vignetted due to the reduced effective width of the glass plates. Special care has been taken to align the rotation axes of both glass plates perpendicular to the rotation axis of the gimbals mount, and to align the rotation axis of the gimbals mount with the optical axis of the stimulus. The alignment accuracy in both cases is measured to be better than 0.08° . This translates into a static error in the degree of linear polarization that scales with the glass plate angles, up to an error of $< 3 \cdot 10^{-3}$ at glass plate angles of 70° . The precision of the tilt motors is $1/60^\circ$, which translates into a dynamic uncertainty of $7 \cdot 10^{-4}$ at worst case glass plate angles of 70° . Stress birefringence in the glass plates and the lens could comprise the state of polarization at the exit pupil. In a worst cases scenario, a stress birefringence of 4 nm/cm is aligned in all three components (with a total thickness of 2 cm) at 45° to the rotation angle of the glass plates. This results in a relative reduction of P_L by $4 \cdot 10^{-3}$ at 400 nm. Stokes V is increased to about 5% when $P_L = 0.5$, but since SPEX is insensitive to Stokes V this can be neglected.

4.4.3 Output characterization

Verification polarimeter

Although the state of linear polarization of the emergent beam as a function of glass plate tilt angle can be calculated using the Fresnel equations, it was found that the limited knowledge of the anti-reflection coating causes uncertainties in the polarization larger than the required accuracy, up to 0.05 at large glass plate angles. Also possible stress birefringence can cause uncertainties in the state of linear polarization. Therefore, the polarization stimulus was experimentally verified by measuring the state of linear polarization of the stimulus output using a verification polarimeter. This verification polarimeter consists of a rotating linear polarizer in front of a $400 \mu\text{m}$ fiber and collimator, that is positioned at the exit pupil of the stimulus. Since the intensity of the light source can vary several percents over the timescale of a measurement, a second fiber collimator is placed near the integrating sphere in order to monitor intensity variations. Light collected by the two fibers is channeled to two synchronized spectrometers (Avantes AvaSpec). Upon normalizing the polarizer measurements by the lamp monitoring channel, the intensity stability is $\sim 10^{-4}$.

The measurement sequence consists of rotating the polarizer over 360° in steps of 10° and measuring the resulting spectra. A sine-wave with a period of 180° is obtained, and the ratio of the modulation amplitude and the mean value gives P_L . Also a sine-component with a period of 360° is fitted to the data in order to account for

a possible beam wobble due to slight misalignments or small transmission variations over the clear aperture of the polarizer. Note that the 360° component is orthogonal to the 180° and thus does not interfere with the determination of P_L , but it does substantially improve the fit of the measured response.

The extinction ratio of the rotating polarizer is better than 10^3 across the spectrum, so the corresponding error for the stimulus polarization range of $P_L < 0.5$ is smaller than 10^{-3} , which is within the requirements. The zero-point of the stimulus as measured with the verification polarimeter is $\sim (4 \pm 2) \cdot 10^{-4}$, where the error bar describes the standard deviation of multiple measurements. Two independent measurement techniques using SPEX yield $2 \cdot 10^{-4}$ for the zero-point (see Sections 4.4.3 and 4.5.1). Since there is no ground truth, we adopt $4 \cdot 10^{-4}$ as the total uncertainty of the verification polarimeter, as the sum of the systematic zero-point difference of $2 \cdot 10^{-4}$ and the random error of $2 \cdot 10^{-4}$.

Zero-point measurement using SPEX

Knowledge of the stimulus zero-point allows the assessment of systematic errors of the verification polarimeter, which in turn improves the calibration of the stimulus itself. Therefore, an independent method for determining the zero-point of the stimulus is needed to verify the by design very low degree of polarization at zero glass plate tilt angle. Also, the verification polarimeter measurement and uncertainty of $\sim 4 \cdot 10^{-4}$ is larger than the anticipated zero-point. Hence, a more accurate determination of the zero-point allows constraining the zero-point capability of SPEX even better.

An independent, indirect measurement of the stimulus zero-point is performed using SPEX data, by analyzing the angle instead of the degree of linear polarization as a function of glass plate tilt angle. At zero glass plate tilt angle, the angle of linear polarization is that of the zero-point polarization of the source, including instrumental polarization inside SPEX. For increasing tilt angles, the angle of linear polarization rapidly converges to the direction of the polarization that is induced by the glass plates, namely perpendicular to the tilt axis (0°). The faster the convergence towards $\phi_L = 0^\circ$, the lower the instrumental polarization of the stimulus is. This method obviously only works when ϕ_L of the instrumental polarization is not equal to the direction of polarization that is induced by the glass plates. A simple solution in that case is to rotate the glass plates by 90° around the optical axis. By assuming a spectrally constant ϕ_L during demodulation of SPEX data as a function of glass plate tilt angle, and by employing the full spectrum fit described in Section 4.3.3, the angle of linear polarization can be determined with high accuracy even at very low degrees of linear polarization.

The extracted ϕ_L is plotted for several glass plate tilt angles in Fig. 4.6a for the central 4° of the FoV. The results show indeed a rapid convergence of ϕ_L towards 0° at increasing glass plate angles. The angle of linear polarization cannot be reliably extracted from measurements taken at glass plate tilt angles below $\sim 4^\circ$, i.e. for $P_L \lesssim 10^{-3}$. Note that the convergence is faster at the central part of the FoV

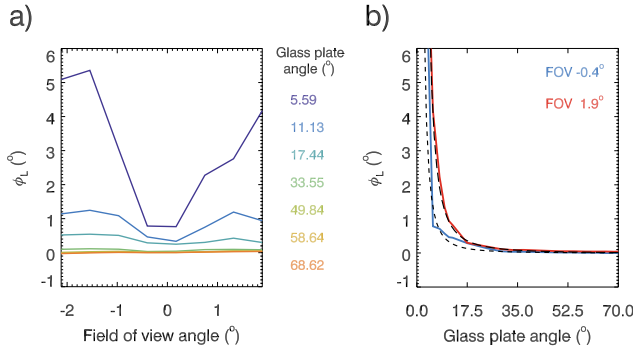


Figure 4.6: *a)* Measured angle of linear polarization as a function of FoV angle plotted for several glass plate tilt angles. *b)* Measured angle of linear polarization as a function of glass plate tilt angle plotted for two FoV angles. The dotted lines represent the results of a modeled calculation.

(corresponding to normal incidence) compared to the outer parts.

To quantify the degree of linear polarization at zero glass plate angle, a model calculation based on the Fresnel equations is fitted to the data, as shown in Fig. 4.6b for FoV angles of -0.4° and 1.9° . The fits indicate a stimulus zero-point polarization of $P_L = (2 \pm 0.3) \cdot 10^{-4}$ with $\phi_L \sim 40^\circ$ at (nearly) normal incidence, and a zero-point polarization $P_L = (6 \pm 0.3) \cdot 10^{-4}$ with $\phi_L \sim 63^\circ$ at a FoV angle of 1.9° . We have performed calculations using the Fresnel equations to put these numbers into perspective. For a FoV angle of 1.9° , the angle of incidence on the glass plates is 0.67° , which results in an instrumental polarization of the stimulus of $\sim 0.7 \cdot 10^{-4}$. For the same FoV angle, the instrumental polarization by two refractions at the (uncoated) entrance and exit interfaces of the Fresnel rhomb and the first interface of the sapphire crystal is $\sim 3 \cdot 10^{-4}$. The observed increase of P_L with FoV angle can thus be explained by a dominant contribution due to instrumental polarization of SPEX, and a smaller contribution of instrumental polarization of the stimulus. Also note that instrumental polarization of SPEX is induced in the direction parallel to the glass plate tilt angle (90°), which can explain the larger ϕ_L at a FoV-angle of 1.9° compared to -0.4° .

4.5 SPEX polarimetric calibration

4.5.1 Absolute polarimetric accuracy

The absolute polarimetric calibration of SPEX has been performed by aligning the exit pupil of the stimulus with the entrance pupil of SPEX, and taking measurements at different glass plate tilt angles while the angle of linear polarization was kept at 0° . Alignment of SPEX with the optical axis of the stimulus is achieved by searching

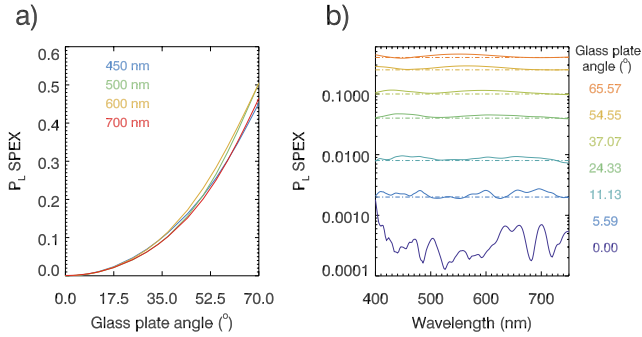


Figure 4.7: *a)* Degree of linear polarization P_L measured with SPEX as a function of the tilt angles of the two glass plates, plotted for four wavelengths. *b)* P_L measured with SPEX as a function of wavelength, plotted for several glass plate angles. The dashed lines indicate the calculated P_L of the stimulus when using the Fresnel equations and a spectrally constant reflection coefficient of 0.005 at one surface of the glass plates.

for edges in terms of signal level for horizontal and vertical pupil alignment and rotational orientation. It was found that pupil overlap in the direction of the optical axis was not critical due to the relatively long focal length of the imaging lens. This allowed an alignment tolerance of ~ 0.5 mm between the position of the exit pupil of the stimulus and the entrance pupil of SPEX.

Glass plate angles are chosen such that the P_L of the stimulus (approximately) takes the following values: 0.0, 0.0001, 0.001, 0.002, 0.004, 0.006, 0.008, 0.01, 0.02, 0.04, 0.06, 0.08, 0.1, 0.15, 0.20, 0.25, 0.30, 0.35, 0.40. The corresponding glass plate angles are calculated using the Fresnel equations, thereby assuming a spectrally flat reflection coefficient of 0.005 on a single side, yielding the values: 0° , 1.25° , 3.95° , 5.59° , 7.89° , 9.65° , 11.13° , 12.42° , 17.44° , 24.33° , 29.41° , 33.55° , 37.07° , 44.21° , 49.84° , 54.55° , 58.64° , 62.27° , 65.57° . These tilt angles are used in each measurement sequence.

The results of the absolute polarimetric calibration of the central part of the FoV of the central viewport are shown in Fig. 4.7. The degree of linear polarization varies from almost 0 to 0.5 with increasing glass plate tilt angles. The noise on P_L as well as the zero-point polarization measured by SPEX is below $1 \cdot 10^{-3}$. Since the demodulation algorithm will always fit a sine-wave with a non-zero amplitude to noisy data, flattening of the spectrum by a better flat-fielding is likely to reduce the apparent noise at very low P_L . Due to the anti-reflection coating on the glass plates, a spectral variation in P_L is observed with a relative size of $\sim 0.1 \cdot P_L$ (best seen for $P_L > 0.01$ in Fig. 4.7b), which is moving towards shorter wavelengths with increasing glass plate angles. This shows the necessity of using a verification polarimeter.

The measurement results of Fig. 4.7 are compared with the stimulus calibration results by resampling both datasets on a 10 nm grid with 10 nm averaging window. The resampled datasets are subtracted from each other and this difference is plotted

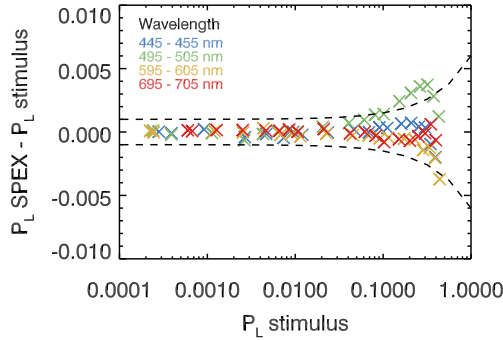


Figure 4.8: Difference between the degree of linear polarization P_L as measured with SPEX and the stimulus P_L plotted as a function of the stimulus P_L . The dashed line indicates the accuracy requirement of the stimulus, which is equal to the requirement for aerosol characterization in the Earth atmosphere.

in Fig. 4.8. These results are representative for the results obtained with other viewing apertures illuminated and for other parts of the FoV, as will be shown below. For the measurement sequence of Fig. 4.7 the difference between SPEX and the stimulus calibration results is at most ± 0.004 . For comparison, the accuracy requirement of the stimulus, which coincides with the requirement for an aerosol characterization instrument, is indicated. From Fig. 4.8 it can be seen that the error in P_L is compliant with this requirement for most of the P_L range and plotted wavelengths. The points corresponding to 500 nm are an exception, which show a clear structure as a function of the stimulus P_L .

This structure of the difference in P_L with stimulus P_L , as well as its spectral structure, is unclear at the moment. However, these results are reproducible within ± 0.003 over the FoV of all three viewports and for different calibration measurements, as shown in Fig. 4.9. Here, results from the center 6° of the FoV are plotted in order to avoid complications within 0.5° from the edge of the FoV as a result of the spatial resolution of the instrument of $\sim 1^\circ$. Because of the reproducibility of the polarimetric calibration, the observed average difference with the stimulus P_L can be used as a calibration of SPEX. If such a calibration is employed, the P_L differences between SPEX and the stimulus are reduced and smaller than 0.003 for all wavelengths over the full P_L range of the stimulus, see Fig. 4.10. This means that, once the origin of the discrepancy in Fig. 4.8 is understood, the polarimetric accuracy of SPEX will be better than ± 0.003 , which implies that SPEX can be fully compliant with the polarimetric requirement for aerosol characterization.

4.5.2 Polarimetric sensitivity

The ability of SPEX to discriminate between two signals with a small polarization difference is investigated by making small changes in the glass plate tilt angles.

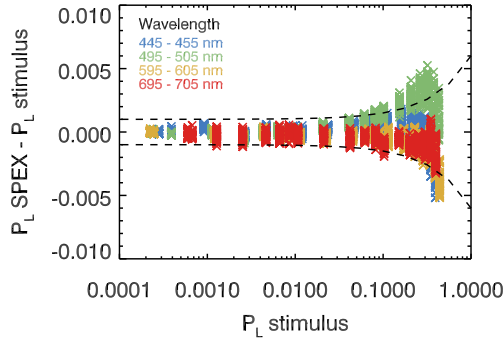


Figure 4.9: Difference between the degree of linear polarization P_L as measured with SPEX and the stimulus P_L plotted as a function of the stimulus P_L . Data from five measurement sequences, covering all three viewports, as well as the center 6° of the FoV (plotted in steps of 0.67°) is included. The dashed line is the same as in Fig. 4.8.

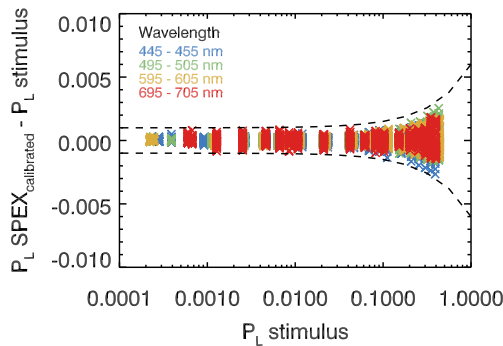


Figure 4.10: Difference between the degree of linear polarization as measured with SPEX and the stimulus plotted as a function of the measured degree of linear polarization of the stimulus when all datasets of Fig. 4.9 are calibrated with the average P_L difference. The dashed line is the same as in Fig. 4.8.

A sequence of measurements has been performed at angles between 36.907° and 37.241° in steps of 0.0166° . These glass plate angles correspond to a polarization range of $2 \cdot 10^{-3}$ around $P_L \approx 0.1$, and incremental polarization of $1 \cdot 10^{-4}$. The results of these measurements are plotted in Fig. 4.11 for four different wavelengths. A clear increase in degree of linear polarization with increasing glass plate angle is observed for all four plotted wavelengths, even though the increase is as small as $2 \cdot 10^{-3}$ over the total angular range of 0.34° . The measured P_L values are fitted with a linear model for each wavelength. The peak-to-peak difference between the measured P_L values and the linear fit is less than $7 \cdot 10^{-4}$, while the typical standard deviation of the data is of the order of 10^{-4} and shot noise limited.

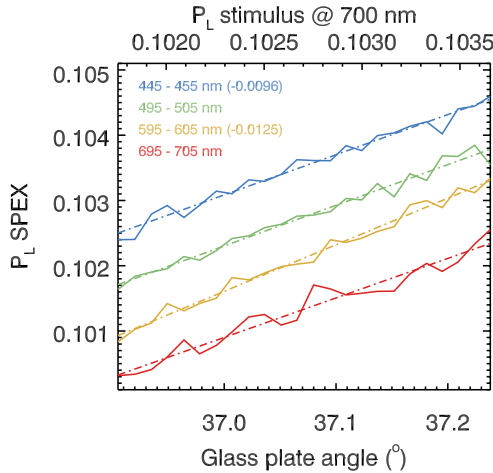


Figure 4.11: The polarimetric sensitivity of SPEX as the measured P_L as a function of a very small range of glass plate tilt angles for several wavelength bands. The dash-dotted lines are linear fits to the measurements. The P_L of two wavelength bands (450 and 600 nm) is offset for better visibility.

4.6 Discussion

The polarimetric calibration results show an agreement between SPEX and the stimulus (i.e. the verification polarimeter) of better than 0.005. However, the difference between SPEX and the stimulus shows a clear structure, both spectrally and as a function of P_L (see Figs. 4.8 and 4.9) that is not yet understood. At this point, three possibilities exist with respect to these results:

- The observed difference in P_L is largely caused by the verification polarimeter. In this case the performance of the verification polarimeter needs to be improved, which will be addressed below.
- The observed difference in P_L is largely caused by a different sampling of the two polarimeters, e.g. due to different pupil size, error in the pupil alignments or acceptance angle of the stimulus output.
- The observed difference in P_L is largely caused by SPEX. In this case SPEX can be calibrated to the results of the verification polarimeter, since the observed differences are stable and reproducible. The resulting accuracy that can be reached is better than 0.003 as shown in Fig. 4.10.

In order to improve the performance of the verification polarimeter, systematic errors due to a potential polarization sensitivity of the spectrograph and fiber must be further reduced. Differential transmission for different polarization directions, e.g. by the spectrograph slit (Jones & Richards 1954) or diffraction grating (Hessel

Et Oliner 1965), changes the modulation pattern created by the rotating polarizer, and is therefore interpreted as a change in polarization. Optical fibers are known to scramble polarization, in particular when the fibers are long and bended (Eftimov et al. 1991), as in the present stimulus. This will reduce the effect of a potential polarization sensitivity of the spectrograph. Adding polarization scramblers between rotating polarizer and optical fiber and/or between optical fiber and spectrograph, might further reduce this sensitivity.

For improving the equality of the sampling of the stimulus of both polarimeters, the entrance pupil of SPEX could be exactly replicated in the verification polarimeter. The 1.1 mm pupil of SPEX can be approximated by a 1 mm fiber, or more accurately using a 1.1 mm pinhole in front of a 1.5 mm fiber. These large diameter fibers also yield a higher signal to noise ratio, thereby obviating the need for a fiber launcher. The polarization properties of the off-the-shelf fiber launcher are unknown, and the anti-reflection coating on it could potentially cause wavelength dependency in the polarization, which is observed in Fig. 4.8.

Two important aspects that could deteriorate the polarimetric accuracy not addressed in this paper are temperature and stray light. In SPEX, the MOR is designed to minimize the change in retardance with temperature in the spectral range of the instrument. Also, small changes in the retardance only lead to a shift in the modulation pattern (which could be used as a temperature sensor if the angle of linear polarization is known from geometry, e.g. in case of (single) scattering events) and do not affect the measurement of P_L . A more pronounced temperature effect can occur when spectrograph focus changes with temperature, because this changes the optical smearing of the modulation pattern and thereby the polarimetric efficiency ϵ_L , see van Harten et al. (2014b). Either the spectrograph must be designed to be athermal, or ϵ_L must be calibrated as a function of temperature. In the latter case, application of the correct ϵ_L requires accurate knowledge of the temperature of the instrument.

Stray light (excluding ghosts) has a similar effect as the dark and vertical smear signal discussed in Section 4.3.1 with the important difference that it depends strongly on the observed scene. In the presented work, the use of an integrating sphere ensures a spatially homogeneous scene, in which case stray light effects are largely compensated by the reference measurement. However, in case of inhomogeneous scenes it is anticipated that a stray light correction algorithm must be employed in order to maintain the high polarimetric accuracy presented in this paper (van Harten et al. 2014b).

Overall, these results not only show the high polarimetric accuracy but also the robustness of the spectral modulation concept. E.g. reference measurements need not to be taken with the same light source or at similar exposure times as calibration or field measurements for yielding highly accurate results. Also, polarimetric calibration results are consistent over different viewports, over the FoV of SPEX and between calibration measurements taken weeks apart. This makes spectral polarization modulation a promising concept for high-accuracy polarimetry and applications that demand high robustness and self-calibratability.

4.7 Conclusions

We have presented the SPEX instrument that employs spectral polarization modulation for achieving very high polarimetric accuracy. The instrument has been polarimetrically calibrated using a dedicated optical stimulus that can supply light with a state of linear polarization that is known within $0.001 + 0.005 \cdot P_L$. It was shown that the stimulus zero-point is at the level of $2 \cdot 10^{-4}$ at normal incidence. The agreement between measurements of P_L with SPEX and a verification polarimeter are shown to be better than 0.005 for all three viewports and over the center 6° of the FoV. When the average systematic (and reproducible) difference between SPEX and the verification polarimeter is used as a calibration, the accuracy of SPEX can become better than $0.001 + 0.005 \cdot P_L$, which is required, among others, for aerosol characterization instruments. The polarimetric sensitivity that can be achieved with SPEX is better than 10^{-4} . This paper therefore shows that spectral polarization modulation has the potential to enable instruments that are suited for aerosol related climate and air quality research, for which the high polarimetric accuracy requirement is currently the main technological challenge.

Acknowledgements

This work was funded by the Netherlands Space Office (NSO) under the Mars Robotic Exploration Programme. The SPEX prototype is developed with two grants from the NSO (PEP61707DS and PEP61830SI) by a Dutch consortium consisting of SRON, Leiden University, cosine measurement systems, Dutch Space, MECON, NOVA Astron, and TNO. GvH acknowledges Utrecht University for funding his research.

Chapter 5

Atmospheric aerosol characterization with a ground-based SPEX spectropolarimetric instrument

Characterization of atmospheric aerosols is important for understanding their impact on health and climate. A wealth of aerosol parameters can be retrieved from multi-angle, multi-wavelength radiance and polarization measurements of the clear sky. We developed a ground-based SPEX instrument (groundSPEX) for accurate spectropolarimetry, based on the passive, robust, athermal and snapshot spectral polarization modulation technique, and hence ideal for field deployment. It samples the scattering phase function in the principal plane in an automated fashion, using a motorized pan/tilt unit and automatic exposure time detection. Extensive radiometric and polarimetric calibrations were performed, yielding values for both random noise and systematic uncertainties. The absolute polarimetric accuracy at low degrees of polarization is established to be $\sim 5 \cdot 10^{-3}$. About 70 measurement sequences have been performed throughout four clear-sky days at Cabauw, the Netherlands. Several aerosol parameters were retrieved: aerosol optical thickness, effective radius, and complex refractive index for fine and coarse mode. The results are in good agreement with the co-located AERONET products, with a correlation coefficient of $\rho = 0.932$ for the total aerosol optical thickness at 550 nm.

Van Harten, De Boer, Rietjens et al. *Atmospheric Measurement Techniques Discussions*, 7, 5741–5768 (2014)

5.1 Introduction

Atmospheric aerosols, also known as particulate matter, are particles or droplets suspended in the air. Some types are naturally occurring, such as pollen, spores, sea salt, desert dust and volcanic ash, others are mostly anthropogenic, such as sulfates, nitrates, soot, smoke and ashes from combustion or forest fires, or ammonia salts from agriculture.

Studying aerosols and their spatial and temporal distribution is of great importance because of their impact on health and climate. Exposure to fine particulate air pollution triggers asthma attacks, can lead to lung diseases, and is associated with natural-cause mortality (Beelen et al. 2014). Health effects are usually worse for smaller particles, because they can penetrate deeper into the lungs. Since anthropogenic aerosols are generally smaller than their natural counterparts, air-polluted areas are not only dangerous because of the larger amount of particles. The toxicity is also dependent on the particles' shape (sharpness, surface area) and chemical composition.

The influence of aerosols on the climate by means of radiative forcing is still very uncertain (IPCC 2013). Forcing mechanisms include the direct and indirect aerosol effect. The direct effect is the scattering or absorption of sunlight by aerosols, which overall has a strong cooling effect. However, particular aerosols like black carbon can make a positive radiative forcing. The indirect aerosol effect means that aerosols, being cloud condensation nuclei, stimulate the formation of clouds, which scatter incoming sunlight back into space. Moreover, the droplets in these clouds tend to be smaller, resulting in an even higher albedo and less efficient precipitation, which implies longer life times. The lack of knowledge about atmospheric aerosol load, properties, and their interaction with clouds, makes the input for and verification of climate models and atmospheric chemistry transport models uncertain.

Atmospheric aerosol measurements from the ground are either performed in-situ or as remote sensing. The most prevalent in-situ measurement method is:

- *Particulate matter (PM) monitoring.* Air is sucked through sampling heads that let particles pass which have a diameter smaller than e.g. 10 or 2.5 micrometer (referred to as PM10 and PM2.5, respectively). The accumulated particles are manually weighed (reference method) or quantified using their attenuation of beta radiation (automated method) (e.g. McMurry 2000). The chemical composition can be determined through lab analysis.

Remote sensing of aerosols often involves the following techniques:

- *Lidar.* A laser pulse is sent into the atmosphere, after which the arrival times and intensities of the backscatter are measured. This results in altitude profiles of the aerosol extinction coefficient. The employment of multiple wavelengths provides the Ångström exponent, an indicator for particle size. An optional depolarization measurement provides information on the aerosol type (e.g. Murayama et al. 1999).

- *Direct sun measurements.* The extinction of the direct solar beam is measured, and translated into an aerosol optical thickness (AOT). The wavelength dependence of the AOT is an indicator for particle size distribution (O'Neill et al. 2003). Regular instrument calibrations on high mountains provide the top-of-atmosphere irradiance (Holben et al. 1998).
- *Diffuse sky measurements.* Sunlight scattered in the atmosphere is measured at multiple angles and wavelengths, and compared with radiative transfer calculations in model atmospheres. A variety of aerosol parameters can be retrieved, e.g. optical thickness, size distribution and complex refractive index, indicative of chemical composition (e.g. Dubovik & King 2000). The added value of polarization measurements has been shown for satellite geometry by Mishchenko & Travis (1997), Mishchenko et al. (2004), Hasekamp & Landgraf (2007), and for ground-based geometry by Boesche et al. (2006), Li et al. (2009). The advantage of using this method is that it provides fast and cost-effective measurements of various important aerosol parameters for climate and health studies, that may be related directly to both other ground-based measurements as well as aerosol optical thickness retrieved from satellite data.

With our groundSPEX instrument, we aim at performing multi-angle multi-wavelength diffuse sky radiometry and polarimetry with sub-percent absolute polarimetric accuracy. We describe the instrument design and calibration, including the radiometric and polarimetric performance. We present clear-sky measurements and the retrieved aerosol parameters, and compare those to the co-located AERONET products.

5.2 Measurements

5.2.1 GroundSPEX instrument

The measurements are performed with a dedicated ground-based version of the SPEX instrument for satellite-based atmospheric aerosol characterization (van Harten et al. 2011). This instrument measures the spectral radiance and linear polarization of skylight using spectral polarization modulation. In this technique, a carefully selected combination of birefringent crystals with a total retardance of δ encodes the degree (P_L) and angle (ϕ_L) of linear polarization as the amplitude and phase (ψ) of a carrier wave in the intensity spectrum I_0 (see Fig. 5.1), according to (Snik et al. 2009):

$$S_{\pm}(\lambda) = \frac{1}{2} I_0(\lambda) \left[1 \pm P_L(\lambda) \cos(\psi(\lambda)) \right], \quad (5.1a)$$

$$\psi(\lambda) \equiv \frac{2\pi\delta(\lambda)}{\lambda} + 2\phi_L(\lambda). \quad (5.1b)$$

This modulation technique enables snapshot polarimetry at high accuracy, using a robust instrument with no moving parts, ideal for field deployment.

The spectral carrier wave is created using the following static train of optics:

- *Achromatic quarter-wave retarder with fast axis at 0° (horizontal).* Incoming linear polarization at 45° is converted into circular polarization, and vice versa. In this way, the instrument is turned into a full linear polarimeter, while becoming insensitive to circular polarization. An off-the-shelf N-BK7 Fresnel rhomb from Thorlabs is used, with a maximum retardance deviation of 2% across the visible wavelength range. Calibration of misalignment and retardance deviation is described in Section 5.2.2.
- *Multiple-order retarder with fast axis at 45° .* The ellipticity of the incoming polarization is modulated in a strongly wavelength dependent way using birefringent crystals. A subtractive combination of 1.63 mm quartz and 3.83 mm magnesium fluoride creates ~ 43 modulation periods within 400–900 nm, with the size of a period ranging from ~ 5 –25 nm from the blue to the red end, respectively. For this crystal combination, manufactured by B. Halle, the thermal dependence of the retardance of the individual crystals largely cancels out: for a temperature range of ± 20 K the measurement of the angle of linear polarization is stabilized to within $\pm 1.5^\circ$. Section 5.2.2 shows that this has a negligible impact on the degree of linear polarization, our main observable.
- *Polarizing beam-splitter, splitting linear polarization at 0 and 90° .* This analyzer turns the ellipticity modulation into a sinusoidal spectral intensity modulation, according to Eq. (5.1a). Each beam out of the polarizing beam-splitter carries the full linear polarization information, but their modulations are exactly out of phase (see Fig. 5.1). In this way, the sum of the two beams yields the unmodulated intensity spectrum I_0 at full resolution. The redundancy in the both spectrally and spatially modulated polarization is used for a post-facto differential transmission correction (van Harten et al. 2014c). This correction typically decreases the associated error in the degree of linear polarization by an order of magnitude. Moreover, this quasi beam-exchange technique strongly reduces the polarimetric errors due to uncorrected dark signal. The polarizing beam-splitter is a calcite Foster prism from Melles Griot, with an extinction ratio of 10^{-5} .

The two beams out of the polarizing beam-splitter are focussed onto $550 \mu\text{m}$ fibers by 35 mm focal length lenses, yielding a field-of-view of 0.9° , with an entrance aperture of 1 cm^2 . The fibers are fed into two synchronized spectrographs from Avantes, both equipped with a 3648 pixels, 16 bits CCD detector, 600 lines/mm reflection grating, and a $25 \mu\text{m}$ entrance slit, resulting in a wavelength range of 360–910 nm at 0.8 nm resolution, using an order-sorting filter. The optics and spectrographs are positioned in an IP66 weatherproof camera housing from 2B Security, together with the laptop that is controlling the spectrograph and motorized pan/tilt mount. The laptop can connect to a computer network using LAN or WiFi, after which a remote desktop connection can be established to control the instrument from anywhere. A fused silica entrance window behind a 15 cm long entrance tube protects the optics and electronics from rain, and provides straylight baffling. The IP66 pan/tilt mount

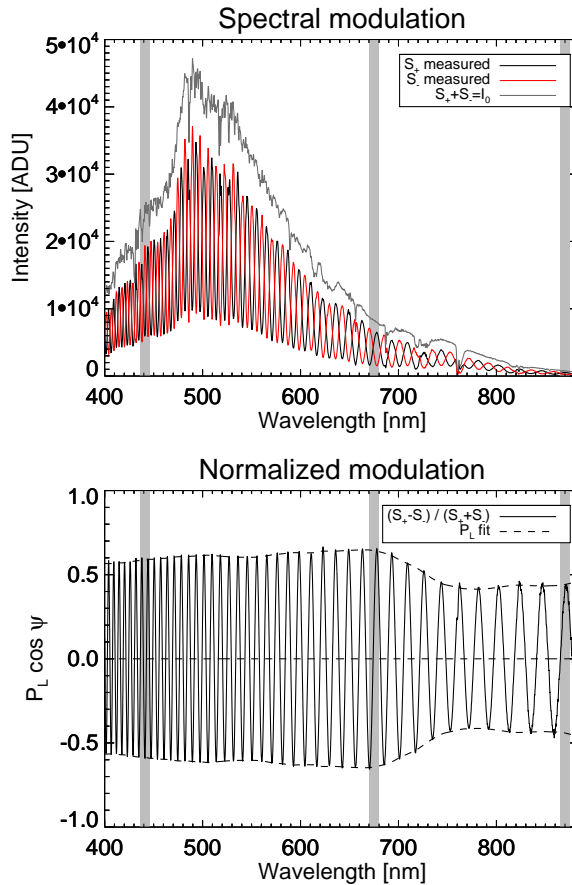


Figure 5.1: *Top.* The groundSPEX instrument measures the two perpendicularly modulated spectra S_+ and S_- simultaneously. The degree (P_L) and angle ($\phi_L(\psi)$) of linear polarization are encoded as the relative amplitude and phase of the modulation pattern, respectively. The sum of the two modulated spectra is the intensity spectrum I_0 at full resolution. *Bottom.* Curve fits of $P_L \cos \psi$ to the normalized modulation in a moving window provide the spectral polarization information. Note the decrease in polarization at 550 nm and above 700 nm, due to the increase in the albedo of grass, called green bump and red edge, respectively. Note also that the strong Oxygen A absorption band around 765 nm is clearly visible in the intensity spectrum (top plot), whereas it has no impact on the normalized modulation pattern (bottom plot). The grey vertical bands indicate the wavelength bins that have been used for retrieving the aerosol parameters, matching the spectral bands of the co-located AERONET sun photometer, viz. 441, 675 and 870 nm, all with a full width at half maximum of 10 nm.

from 2B Security rotates at a speed of $50^\circ/\text{s}$ in the azimuth and $20^\circ/\text{s}$ in the altitude

direction, with electronic position accuracies of 0.01° and 0.006° , respectively.

The instrument control software is able to autonomously execute a measurement sequence upon receiving a user-supplied list with pan and tilt angles. Per pointing, the spectrograph first records a trial spectrum at a very short exposure time (10 ms), that is subsequently extrapolated to determine the exposure time for a desired intensity value. Typical exposure times are 50 – 200 ms, and 50 spectra are averaged for a signal to noise ratio of > 370 per pixel to enable spectral line polarimetry with a sensitivity of at least $2.7 \cdot 10^{-3}$, so the measurement cadence is about 10 seconds. Note that this paper does not deal with line polarimetry, but with continuum polarimetry in 10 nm wide bands, resulting in a polarimetric noise of only 10^{-4} .

5.2.2 Calibrations

Several calibrations need to be performed before the data can be fed into the aerosol retrieval algorithm. Moreover, a careful quantification of the measurement errors and their statistics is crucial to obtain reliable error bars on the retrieved aerosol parameters.

Wavelength calibration

The wavelength calibration of the spectrographs is performed using a mercury/argon line lamp, fiber-connected to the spectrographs. Nine spectral lines have been identified across the spectrum, and a third-order polynomial relates each detector pixel to a wavelength. The root-mean-square deviation between the theoretical line wavelengths and the calibrated values is 0.01 nm. The spectra of one spectrograph are matched to the wavelengths of the other spectrograph using linear interpolation.

Detector dark signal

The instrument is usually exposed to direct sunlight, and the detector is uncooled, so a careful dark current subtraction is important. The dark current cannot be measured during a measurement sequence, because the instrument is not equipped with a mechanical shutter. Therefore, the dark current was characterized offline as a function of exposure time and temperature, using the built-in temperature sensor. A typical detector temperature range during a day is 20–40 °C. It was found that the bias strongly decreases with increasing temperature (from 1000 to 400 analog-to-digital units (ADU)), for shorter exposure times the dark current increases linearly with exposure time, and at a higher rate for higher temperatures, but for exposure times above 100 ms the increase with exposure time gets strongly suppressed, with this non-linearity being worse for higher temperatures. For each pixel, a 4th-degree 2-dimensional polynomial was fitted to the dark calibration measurements, providing a continuous correction model (see Fig. 5.2). The root-mean-square deviation between the model and the calibration measurements is 9 ADU for each pixel. Although these residuals are centered around zero, it is not random noise; it shows

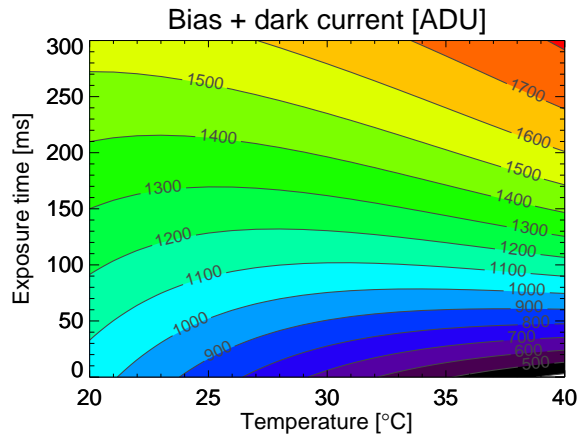


Figure 5.2: Calibration model of bias and dark current as a function of exposure time and temperature. The variable exposure time and direct exposure to weather results in a dark range of about 1000 ADU (out of a maximum of 65536).

dependencies on temperature and exposure time. This is presumably a side-effect of the calibration method: the exposure time was repeatedly increased from 1 to 1000 ms, while the temperature was varied between 10 and 45 °C in a non-linear way. There may have been a lag between the temperature at the detector and the thermometer, particularly at fast temperature changes. After calibration, the effect of temperature gradients is counteracted with the use of optical black detector pixels. The average value of those 13 pixels at the time of measurement, compared to their average value at the time of calibration, is added to the dark model as a dynamic correction. Pixel-to-pixel variations of the dark current calibration residuals seem random, with a standard deviation of 6 ADU.

Differential transmission

The next calibration step is a correction for the differential transmission for the two optical paths. Alignment differences lead to a slowly spectrally varying differential transmission of 0.8–1.2, an issue with the order-sorting filter in one of the spectrographs creates transmission spikes of $\pm 10\%$ at 603 and 622 nm, and differences in the detector chips cause a differential spectral fringe pattern with an amplitude of 5%. It is important to note that a flatfield spectrum needs to be measured with strictly unpolarized light; in case of polarization, the corresponding modulation pattern will be introduced into every single measurement during flatfielding, thereby creating spurious polarization. Light sources are typically polarized at the $\sim 5\%$ level, therefore an unpolarized sky spectrum was used as flatfield. To that end, the polarization of skylight was measured throughout the principal plane in steps of 1°,

and the least polarized spectrum ($P_L < 10^{-3}$) has been selected. Residual differential transmission is dynamically corrected for by the demodulation algorithm as described by van Harten et al. (2014c). They show that the eventual error in the degree of linear polarization due to differential transmission is smaller than 10^{-4} .

Polarimetric calibration

Calibration of the polarization measurements is performed by inserting a rotatable polarizer in the entrance tube of the instrument. The thus measured spectral polarization describes the spectral efficiency ϵ of the polarimetry, which is ~ 0.95 for wavelengths longer than 600 nm. At shorter wavelengths the efficiency gradually decreases to ~ 0.85 at 400 nm, because the contrast of the faster modulation gets washed out by the spectrograph slit function. The efficiency not only depends on the wavelength, but also on the angle of linear polarization of the incident light. In case the quarter-wave retarder is not exactly a quarter-wave, polarization at 45° will partly leak through the multiple-order retarder without being modulated. The maximum spectral retardance deviation of 2% for the Fresnel rhomb leads to a decrease in modulation amplitude of $5 \cdot 10^{-4}$, which is barely measurable. Misalignments of the quarter-wave retarder and multiple-order retarder decrease the modulation amplitudes for both polarization at 0 and 45° , but not by the same amount. For example, realistic misalignments of $\pm 2^\circ$ cause a differential modulation efficiency of 2%. Therefore, the polarization calibration measurements are performed for polarizer orientations of 0, 10, . . . , 170° . Based on the angle of linear polarization of a sky measurement, the corresponding spectral efficiency is constructed by interpolation of the calibration measurements.

The uncertainty in the polarization measurements is composed of systematic uncertainty and random noise. Potential sources of systematic uncertainties are imperfect dark signal subtraction and instrument changes with temperature. Using the equations in van Harten et al. (2014c) for the propagation of uncorrected dark current, for typical intensities in the three spectral bands as shown in Fig. 5.1, the relative polarimetric uncertainties due to dark signal are 0.1%, 0.2% and 2.3% at 441, 675 and 870 nm, respectively. Note that the calibration measurement for the polarimetric efficiency is also affected by the same amount. The athermal multiple-order retarder yields a thermal stability in the angle of linear polarization of $\pm 1.5^\circ$ over a ± 20 K temperature range. The corresponding uncertainty in the degree of linear polarization, through the dependency of the polarimetric efficiency correction on the angle of linear polarization, is negligible. Spectrograph defocus due to temperature changes leads to a loss of spectral resolution, thereby directly impacting the modulation contrast, just like the spectrograph slit function. A typical spot degradation of 1 pixel per 20 K for an $f/4$ aluminum spectrograph results in a reduction of the modulation amplitude of 2% in the blue, where the modulation period is ~ 6 nm, whereas in the red the efficiency decreases by only 0.1% because the modulation period is 4 times larger. The vast majority of the measurements were taken within 5 K of the efficiency calibration measurements, leading to thermal uncertainties in

the polarimetric efficiency of 0.5%, 0.1% and 0.03% at 441, 675 and 870 nm, respectively. The total root-sum-squared relative systematic polarimetric uncertainties at the aforementioned wavelengths are 0.5%, 0.3% and 3.2%, respectively. In the blue the polarization error is dominated by thermal spectrograph defocus, whereas in the red the main error source is residual dark signal. A complete error analysis for spectrally modulated polarization measurements, including measurements of the temperature sensitivity of the polarization, will be presented in forthcoming papers (van Harten et al. 2014b, Rietjens et al. 2014).

The random noise in the polarization is determined by fitting each polarization curve as a function of scattering angle θ for tens of principal plane scans to an empirical function by Dahlberg (2010), given by:

$$P_L(\theta) = \frac{\sin^2(\beta_1\theta + \beta_2)}{1 + \cos^2(\beta_1\theta + \beta_2) + 2\beta_3/(1 - \beta_3)}. \quad (5.2)$$

The free parameters β_1 and β_2 allow for a possible pointing error, as well as a shift of the maximum polarization to a scattering angle different than 90° , which is often observed (e.g. Boesche et al. 2006). The atmospheric depolarization factor β_3 determines the maximum degree of linear polarization. The best fit values for β are not used, but they are needed to leave no systematic fit residuals in order to get a reliable value for the random noise in the degree of linear polarization. The root-mean-square of the residuals of all fits together quantifies the absolute random polarimetric noise, which is 0.004, 0.006 and 0.006 at 441, 675 and 870 nm, respectively. These values are an order of magnitude larger than photon noise and random instrumental errors like detector readout noise and pointing instability, so it is believed to be dominated by sky variations like very thin inhomogeneously distributed cirrus that is not visible to the naked eye.

As an independent verification of the polarimetric calibration, the polarization at 870 nm of the aforementioned principal plane scans is compared with the co-located AERONET CIMEL sun photometer, equipped with polarization filters at different orientations. For 93% of the data the difference between the instruments is within their combined root-sum-squared error bar, for an uncertainty of 0.01 for the sun photometer (Li et al. 2009). This hints at an overestimation of the groundSPEX error bar, for example because the particular temperatures and exposure times are associated with a smaller than average residual dark current.

A summary of the polarimetric calibration is given in Table 5.1.

Radiometric calibration

The radiance measurements are calibrated against the co-located AERONET CIMEL sun photometer, using the same tens of principal plane scans that were used for the polarimetric calibration. The measurements were not strictly synchronized; on average they were performed within 11 minutes of each other, and within 1.7° scattering angle. However, the stable sky conditions and smooth variation of radiance with time and scattering angle allow us to linearly interpolate the two AERONET scans

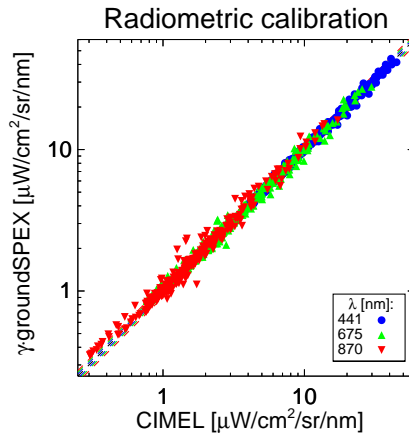


Figure 5.3: Correlation between sky radiances measured with groundSPEX and the CIMEL sun photometer used for the calibration of the gain $\gamma(\lambda)$ of groundSPEX. The dashed lines indicate the combined systematic and random error bars. Note the double logarithmic scale, so the errors scale with intensity.

closest in time to the time of the groundSPEX measurement, followed by a linear interpolation to groundSPEX' scattering angles. For each scan there is a perfect linear relationship between AERONET and groundSPEX, but the gain $\gamma(\lambda)$ that relates groundSPEX radiances in ADU/ms to CIMEL radiances in $\mu\text{W}/\text{cm}^2/\text{sr}/\text{nm}$ changes significantly from scan to scan. The origin of this phenomena is unknown, it is not correlated with time or temperature, and it can not be explained by residual dark signal or scattering angle dependent straylight. Therefore, the standard deviation of all the best fit values for γ translates into a relative systematic intensity uncertainty of 2.8%, 4.5% and 5.7% at 441, 675 and 870 nm, respectively. The standard deviation of the residuals for all these fits combined gives the relative random intensity noise of 2.6%, 4.6% and 7.6%, respectively. The gain itself is found by fitting the data of all scans together, yielding values for $\gamma(\lambda)$ of 0.0429, 0.0229 and 0.1107, respectively. The deviations between the instruments clearly scale with intensity, therefore a weighted least squares fit is applied, where the weights are given by the inverse radiances squared. The result of the radiometric calibration is shown in Fig. 5.3, where the dashed lines represent the total root-sum-squared systematic and random error.

A summary of the radiometric calibration is given in Table 5.1.

Pointing calibration

The absolute pointing is calibrated by putting the sun at the center of the field-of-view at different times during the day, after inserting a neutral density filter to

avoid overexposure. The standard deviation of the hence obtained absolute pan and tilt angles is 0.2° , yielding a total pointing accuracy of 0.3° . The electronic pointing errors are negligible compared to this calibration accuracy.

Table 5.1: Summary of the polarimetric and radiometric calibrations.

Measurement	Systematic error			Random error			
	λ [nm]	441	675	870	441	675	870
Polarization (P_L)		$0.005 P_L$	$0.003 P_L$	$0.032 P_L$	0.004	0.006	0.006
Radiance (I)		$0.028 I$	$0.045 I$	$0.057 I$	$0.026 I$	$0.046 I$	$0.076 I$

5.2.3 Observations

Several atmospheric scattering measurements were performed with the ground-SPEX instrument at the Cabauw Experimental Site for Atmospheric Research (CE-SAR Observatory) in the Netherlands (51.971° N, 4.927° E), also known as Cabauw (<http://www.cesar-observatory.nl>). This site, located in a rural environment with mainly grassland within a radius of 10 km, but in between extended urban areas, hosts a large variety of instrumentation, e.g. for research of the atmospheric boundary layer, clouds, aerosols, greenhouse gases, the Baseline Surface Radiation Network (BSRN), and the AERosol RObotic NETwork (AERONET) (Apituley et al. 2008, Holben et al. 1998).

Throughout four mostly cloudless days in 2013, viz. July 7, 8 and 9, and September 5, the instrument sampled the intensity and polarization at 360–910 nm in the principal plane, defined by the instrument, zenith and the sun. Each principal plane scan consisted of 8 to 25 viewing zenith angles between 60 and -60° . Angles closer to the horizon were avoided because the plane-parallel model atmosphere in the aerosol retrieval algorithm is not valid at larger zenith angles, and the contribution of the limitedly known albedo increases close to the horizon, as well as the variability of the scene. The groundSPEX instrument cannot measure within 6° from the sun, because of straylight and overexposure.

Cloud-screening has been performed using the co-located total sky imager (TSI) that records an image of the entire sky every minute. Since the sky was clear for most of the time, any changes because of clouds drifting in or cirrus appearing were clearly visible. Principal plane scans were only considered acceptable if the entire principal plane is clear during the entire scan. The daily average relative humidities were $\sim 70\%$.

5.3 Aerosol retrieval

The atmospheric aerosol properties are retrieved from the scattered radiance and degree of linear polarization at 441, 675 and 870 nm, using the inversion algorithm

described by Di Noia et al. (2014). This algorithm performs an iterative retrieval of a set of aerosol parameters (aerosol column concentration, effective radius, and complex refractive index for fine and coarse mode) along with the surface albedo, using Phillips-Tikhonov regularization. The forward model is described by Hasekamp & Landgraf (2005). The initial guess is provided by a neural network, trained using representative simulated data (Di Noia et al. 2014). The distinction between systematic and random errors in the radiance and polarization measurements (see Section 5.2.2) allows us to assess the impact of measurement errors on retrieved aerosol parameters. We showed in Section 5.2 that systematic polarization errors are caused by bias drift and temperature, resulting in an increase or decrease in the degree of linear polarization for all wavelengths at the same time. The systematic uncertainty in the radiances also has the same sign for all wavelengths, but is not related to the sign of the polarization error. Therefore, the propagation of systematic errors has been calculated by performing the aerosol retrieval for 9 scenarios: radiance without systematic error, radiance minus systematic error, and radiance plus systematic error, all in combination with polarization without and with positive and negative systematic error. The propagation of random errors is captured in the retrieval error covariance matrix, which is calculated as part of the iterative inversion process. The size of the random measurement errors is similar to (radiometry) or smaller than (polarimetry) the systematic uncertainty. Moreover, ~ 100 data points are fitted during the retrieval for one principal plane measurement (radiance and polarization at 3 wavelengths at ~ 15 scattering angles, see Fig. 5.4), so the random errors will average out by a factor of $\sqrt{100} = 10$, whereas the systematic errors move entire datasets up or down. Therefore, the impact of random errors on the retrieved aerosol parameters is assumed to be negligible compared to systematic uncertainties.

5.4 Results

The measured spectral radiance and degree of linear polarization as a function of scattering angle for one principal plane scan is shown in Fig. 5.4, together with the retrieval algorithm best fit. The error bars represent the total uncertainty in the measurements, viz. the root-sum-squared systematic and random errors. The fit has a reduced chi-squared of 0.57, and yields an aerosol optical thickness (AOT) at 550 nm of $0.228^{+0.013}_{-0.018}$ (see Fig. 5.5).

July 9 shows both the lowest and highest AOT of our dataset, as well as the steepest AOT change in time. Therefore, the AOT time series of July 9 is shown in Fig. 5.5, together with the AERONET direct sun AOT, calculated using the Beer-Lambert-Bouguer law (Holben et al. 1998). The error bars on the groundSPEX measurements represent the systematic errors as the lowest and highest retrieved AOT for the 9 input scenarios as described in Section 5.3. The AERONET level 1.5 data are cloud-screened and calibrated, but post-calibration has not been applied, hence the AOT error bar of ± 0.02 (Eck et al. 1999). The ability of groundSPEX

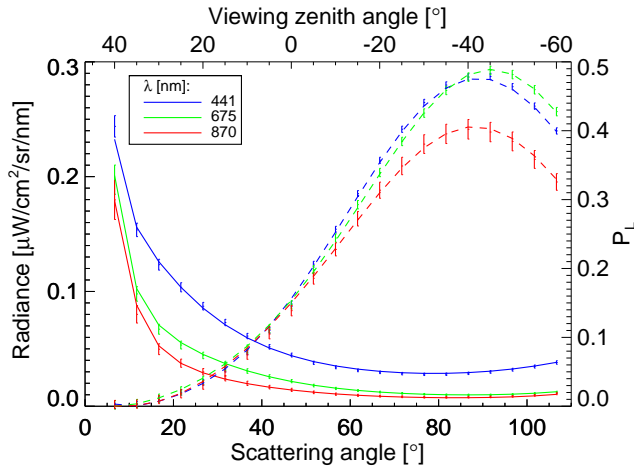


Figure 5.4: Measurements (displayed as vertical error bars) and retrieval algorithm best fit of spectral radiance (solid curves) and degree of linear polarization (dashed curves) as a function of scattering angle in the principal plane. The mean solar zenith angle was 46.66° , with a drift of $< 0.03^\circ$ during the measurements. CESAR Observatory, July 9, 2013, 14:55 UTC.

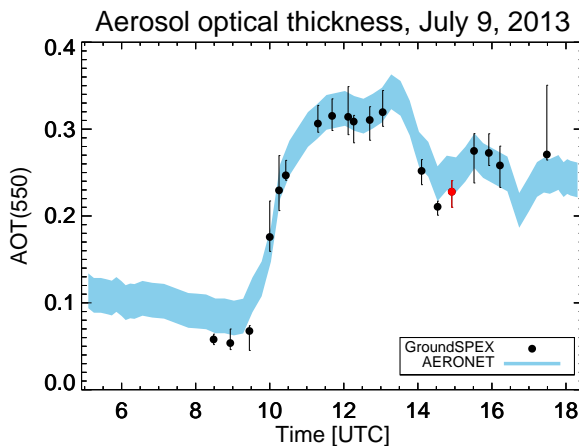


Figure 5.5: Aerosol optical thickness at 550 nm during the day of July 9, 2013, at Cabauw, the Netherlands. GroundSPEX diffuse sky measurements are compared with AERONET direct sun measurements. The red data point at 14:55 UTC is retrieved from the measurements displayed in Fig. 5.4.

to accurately measure AOT, often considered the main aerosol parameter, is clear, even in the rapidly changing atmospheric conditions around 10:00 UTC, even without directly observing the sun.

A comparison between groundSPEX and AERONET of retrieved aerosol parameters for the entire dataset is shown in Fig. 5.6. The AERONET AOT in the upper plot is the total AOT retrieved from direct sun measurements at multiple wavelengths, interpolated to 550 nm (so that includes the data from Fig. 5.5). A least squares fit yields a regression line of $\text{groundSPEX} = 0.005 + 0.893 \text{AERONET}$, with a Pearson correlation coefficient of $\rho = 0.932$.

The AOT of the fine and coarse mode measured with AERONET are retrieved using the Spectral Deconvolution Algorithm (SDA) (O'Neill et al. 2001, 2003), that employs the spectral shape of the direct sun AOT. These AOT retrievals are performed at 500 nm, resulting in a slight overestimation of ~ 0.01 compared to groundSPEX at 550 nm. The error bars on the SDA fine and coarse mode AOT are provided with the retrieval results of AERONET.

The effective radius of the fine and coarse mode, as well as the spectrally averaged total complex refractive index as determined by AERONET, are retrieved with the inversion algorithm by Dubovik & King (2000) that accounts for non-spherical particles (Dubovik et al. 2006), using both direct sun and diffuse sky measurements. The errors in the effective radii are unknown. The errors in the total refractive index are 0.04 for the real part and 50% for the imaginary part (Dubovik et al. 2000). For groundSPEX, the total refractive index is the AOT-weighted sum of the retrieved spectrally flat fine and coarse mode refractive indices.

All error bars shown for groundSPEX are the result of systematic measurement uncertainties, for reasons explained in Section 5.3. Only retrievals with a reduced chi-squared smaller than 10 are presented. The absolute chi-squared values do not translate directly into a probability that the data matches the model, due to systematic errors in the data and the model, however, the relative values can still be used as a measure for goodness of fit. To get a feel for the meaning of the absolute and relative chi-squared values, the results in Fig. 5.6 are color coded based on the chi-squared of the retrievals. For a fair comparison between the different parameters, the plotted range for each aerosol parameter is the total range of possible values.

5.5 Discussion

It is important to make a clear distinction between the AERONET direct sun total AOT, and the other AERONET products. The AERONET measurement of direct sun AOT is straightforward and reliable, and it is therefore crucial that the groundSPEX total AOT does not differ significantly. Any other AERONET products involve inverse modelling, so there is no absolute ground truth. Moreover, both the data and the error bars, as well as the inversion algorithms are different for both instruments. The AERONET products are derived from radiance measurements, whereas groundSPEX employs both radiometry and accurate polarimetry. This makes it difficult to

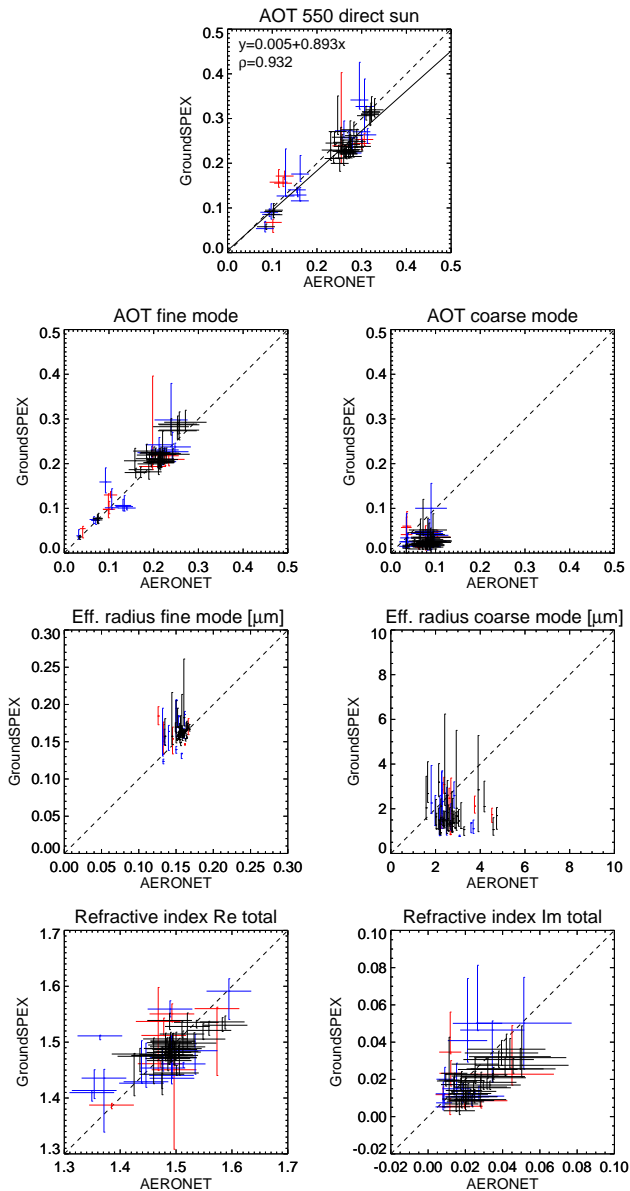


Figure 5.6: Aerosol parameters retrieved with the groundSPEX instrument, compared to AERONET. The different colors correspond to different goodness-of-fit values of the retrieval: $5 \leq \chi^2 \leq 10$ (red), $2 \leq \chi^2 \leq 5$ (blue), $\chi^2 \leq 2$ (black). The dashed lines indicate the groundSPEX = AERONET scenario. The measurements were performed on July 7, 8 and 9, and September 5, 2013, at Cabauw, the Netherlands.

interpret discrepancies, so we will limit ourselves here to a qualitative comparison. Applying the groundSPEX aerosol retrieval algorithm to AERONET data would be an interesting future project, to start disentangling the effects of instrument and data reduction (Pust et al. 2011).

Overall there is a very good agreement between groundSPEX and AERONET for all parameters. In particular, the important and widely measured parameter of total AOT matches the AERONET direct sun measurement over a large range of values, and exhibits relatively small error bars compared to the other aerosol parameters. This results in a correlation coefficient of $\rho = 0.932$, even though groundSPEX is not able to measure within 6° of the sun. The measured range of coarse mode AOT and effective radii is quite limited, so future observations under various atmospheric conditions are needed. The measurements of complex refractive index, that is an indicator of chemical composition, are consistent with AERONET, albeit with slightly larger error bars.

5.6 Conclusions and Outlook

We have developed the groundSPEX instrument, an automated sky-scanning spectropolarimeter. An extensive error analysis has been performed, resulting in random and systematic error bars for radiometry and polarimetry. About 70 measurement sequences of the clear sky have been performed throughout four days in 2013 at the CESAR Observatory in the Netherlands. Important aerosol parameters have been retrieved, such as optical thickness, size distribution and complex refractive index. The results are in good agreement with the co-located AERONET products; for instance, the total aerosol optical thickness at 550 nm exhibits a correlation coefficient of $\rho = 0.932$.

The main advantage of groundSPEX compared to AERONET is the measurement of both radiance and linear polarization across the entire visible spectrum (400–900 nm). The passive spectral polarization modulation technique leads to a robust instrument, with a high polarimetric accuracy of $\sim 5 \cdot 10^{-3}$, at low cost, suitable for deployment in a measurement network. Moreover, the use of diffuse sky measurements and inversions, and the instrument's ability to point in any direction, potentially enables measuring in partially cloudy sky conditions.

GroundSPEX will continue to be employed on a regular basis at the CESAR Observatory as a fast instrument to retrieve optical and microphysical properties of aerosols that are important for climate and health studies. We will build a dataset that will be used to study aerosol parameters in relation to other ground-based measurements as well as satellite measurements. In addition, groundSPEX will provide a valuable and much needed link between ground-based aerosol measurements and data retrieved by satellite instruments, such as GOME-2, MISR, MODIS and OMI, or -hopefully- an airborne or satellite-based version of SPEX itself.

Acknowledgements

The CESAR Observatory is operated by the Royal Netherlands Meteorological Institute (KNMI). The authors thank Marcel Brinkenberg and Alfons Driever (KNMI) for support during the observations. The total sky images were provided by Henk Klein Baltink (KNMI). GvH acknowledges Utrecht University for funding his research. The groundSPEX instrument was developed for the National Institute for Public Health and the Environment (RIVM).

Chapter 6

Spectral line polarimetry with a channeled polarimeter

Channeled spectropolarimetry or spectral polarization modulation is an accurate technique for measuring the continuum polarization in one shot with no moving parts. We show how a dual-beam implementation also enables spectral line polarimetry at the intrinsic resolution, as in a classic beam-splitting polarimeter. Recording redundant polarization information in the two spectrally modulated beams of a polarizing beam-splitter even provides the possibility to perform a post-facto differential transmission correction that improves the accuracy of the spectral line polarimetry. We perform an error analysis to compare the accuracy of spectral line polarimetry to continuum polarimetry, degraded by residual dark signal and differential transmission, as well as to quantify the impact of the transmission correction. We demonstrate the new techniques with a blue sky polarization measurement around the Oxygen A absorption band using the groundSPEX instrument, yielding a polarization in the deepest part of the band of 0.160 ± 0.010 , significantly different from the polarization in the continuum of 0.2284 ± 0.0004 . The presented methods are applicable to any dual-beam channeled polarimeter, including implementations for snapshot imaging polarimetry.

Van Harten, Snik, Rietjens et al. *Applied Optics*, 53, 4187–4194 (2014)

6.1 Introduction

Channeled polarimetry is an emerging technique for passive snapshot spectro- or imaging polarimetry, in which the incoming polarization state is amplitude modulated onto spectral or spatial carrier waves, respectively Kudenov & Goldstein (2011).

In channeled spectropolarimetry (e.g. Nordsieck 1974, Oka & Kato 1999) the spectral modulation is created using a pair of multiple-order (tens of waves) retarders, one at 0° and one at 45° with respect to the analyzer, which introduces highly chromatic phase retardations. This results in three superimposed sinusoidal wave patterns after an analyzer, like in a Lyot filter Lyot (1933). For purely linear polarimetry the crosstalk from circular polarization is minimized, and the spectral resolution is maximized, by replacing the first multiple-order retarder by an achromatic quarter-wave retarder, yielding only one sinusoidal spectral modulation with an amplitude and phase proportional to the degree and the angle of linear polarization, respectively Snik et al. (2009).

Channeled imaging polarimetry can be performed with monochromatic light using wedged retarders Oka & Kaneko (2003) or polarizing beam-splitters like Savart plates Oka & Saito (2006), or with white light using broadband polarization gratings acting as diffractive Savart plates Kudenov et al. (2011).

More advanced configurations have been developed, such as a hyperspectral channeled polarimeter based on Nomarski prisms Kudenov & Dereniak (2012), and a channeled spectropolarimeter with a combination of spectral and spatial carrier waves for optimum resolution and sensitivity, using wedged multiple-order retarders Sparks et al. (2012). A Mueller matrix channeled spectropolarimeter and an imaging version have been described by Hagen et al. (2007) and Kudenov et al. (2012), respectively.

Conventional polarimeters perform the modulation of the polarization in the temporal or spatial domain. An example of a ground-based instrument using temporal modulation, also known as division of time polarimetry, is the all-sky polarimeter based on liquid crystal variable retarders (LCVRs) by Pust & Shaw (2006), where the polarization is reconstructed from sequential modulation measurements on one detector. Spatial modulation, or division of amplitude polarimetry, is used in the FUBIS-POLAR instrument that measures linear polarization at $0, 45, 90$ and 135° simultaneously on 4 separate spectrographs Boesche et al. (2006). Channeled polarimetry has several advantages over these conventional modulation techniques:

- **Snapshot:** the snapshot functionality renders it insensitive to temporal variations, which is particularly useful for science cases with a rapidly moving or variable source, instrument (e.g. remote sensing in low Earth orbit) or medium (e.g. atmospheric seeing).
- **Passive:** the absence of mechanically moving or electronically switching components prevents beam wobble, vibration, and risk of failure.
- **Small:** the core component is small because of the absence of many light paths and motorized stages.

- Accurate: we show that a dual-beam channeled spectropolarimeter achieves significantly higher polarimetric accuracy than a conventional spatial modulator.

The main issue in channeled polarimetry is spurious polarization in case frequencies in the intensity spectrum alias with the modulation frequencies. For example, an atmospheric absorption band could be indistinguishable from a spectrally modulated polarized component. This problem is greatly reduced by using a polarizing beam-splitter as an analyzer. The modulation of the two output beams is exactly out of phase, such that their sum is the unmodulated intensity spectrum, with the additional benefit that this spectrum is at the spectrograph's full resolution Snik et al. (2009), Craven & Kudenov (2010).

The resolution of the polarization data product is usually lower because multiple samples per modulation period are required for an accurate determination of its amplitude and phase. Moreover, the modulation period scales with $1/\lambda^2$, so the red end of the polarization spectrum automatically yields a lower resolution. Channeled spectropolarimetry has therefore been used for measuring polarization in the continuum.

However, we show that it is also possible to measure polarization structure at the intrinsic resolution, provided that the angle of polarization varies smoothly with wavelength. Once the spectral phase of the modulation pattern has been determined, the carrier wave can be divided out in both beams after the analyzer, such that the polarization can be spatially demodulated like in a conventional beam-splitting polarimeter. Moreover, we present a new technique for deriving the differential transmission from the both spectrally and spatially modulated measurements, which can then be corrected for to improve both the continuum and line polarimetry.

An excellent application for channeled spectropolarimetry, based on its aforementioned properties, is the remote characterization of atmospheric aerosols by measuring the intensity and polarization of scattered sunlight. This is of great importance because of the impact of aerosols on health (e.g. Beelen et al. 2014) and climate (e.g. IPCC 2013). Sensitivity studies have shown that accurate microscopic and macroscopic aerosol characterization requires multi-viewing-angle, multi-wavelength radiometry and polarimetry Mishchenko et al. (2004), Hasekamp & Landgraf (2007). Typical values are 30 viewing angles, 5 spectral bands in the visible, a radiometric accuracy of 2%, and an accuracy for linear polarimetry of better than 0.005. Circular polarization only occurs at multiple scattering and is orders of magnitude smaller than linear polarization, so it is ignored in atmospheric aerosol research Kawata (1978).

Scattering measurements in the continuum provide aerosol properties that are integrated over the vertical column. However, altitude information is also important, e.g. for studying aerosol transport, strong interaction with clouds can only occur if they are at the same height, and inhaling of possibly toxic aerosols is usually done at ground level. Moreover, feeding the model atmosphere with the actual vertical profile leads to more accurate aerosol retrievals. It has been shown that polarimetry

in atmospheric absorption bands enables aerosol vertical profiling Stammes et al. (1994), Boesche et al. (2008), Stam et al. (1999). The Oxygen A band at 758–769 nm is a strong absorption band, so sunlight that travels a shorter path length through the atmosphere is more likely to survive. Hence there will be less multiple scattering, and a relatively large contribution of scattering high up in the atmosphere when looking above the sun. Therefore, polarization in the O₂A band provides information on the aerosol vertical distribution.

We show that with a dual-beam spectral modulator, polarization features can be measured at the full spectral resolution of the spectrometer, after applying a correction for the beam transmission ratio, which is retrieved from the continuum polarization measure from the same data. This method also applies to channeled imaging polarimetry, provided that the angle of polarization changes slowly across the image.

6.2 Method

6.2.1 Continuum polarimetry

The groundSPEX instrument van Harten et al. (2014a), a ground-based version of the SPEX for satellite-based atmospheric aerosol characterization van Harten et al. (2011), employs spectral modulation for linear polarimetry. The degree P_L and angle ϕ_L of linear polarization are encoded in the intensity spectrum $I_0(\lambda)$ as Snik et al. (2009):

$$\begin{aligned} S_{\pm}(\lambda) &= \frac{1}{2} I_0(\lambda) t_{\pm}(\lambda) \left[1 \pm P_L(\lambda) \cos(\psi(\lambda)) \right], \\ \psi(\lambda) &\equiv \frac{2\pi\delta(\lambda)}{\lambda} + 2\phi_L(\lambda). \end{aligned} \quad (6.1)$$

The carrier wave is created with an achromatic quarter-wave retarder at 0°, a multiple-order retarder at 45° ($\delta \approx 25\,000$ nm for ~ 30 modulation periods within 400–800 nm), and a polarizing beam-splitter analyzing linear polarization at 0 and 90°. Each spectrum after the analyzer contains the full linear polarization information encoded in the amplitude and phase of the modulation. Since the S_+ and S_- spectra are exactly out of phase, the sum of the spectra yields the unmodulated incoming spectrum $I_0(\lambda)$ at the spectrograph's resolution (see Fig. 6.1), provided that the transmission of the beams is equal, i.e. $t_+(\lambda) = t_-(\lambda)$. In case of uncalibrated differential transmission the sum-spectrum shows residual modulation. As a matter of fact, the redundant modulation allows us to extract the actual $t_-/t_+(\lambda)$ from the measured spectra themselves, along with the polarization information (see Section 6.2.3).

After normalizing the modulated spectra by $I_0(\lambda)$, a least-squares fit to Eq. (6.1) is performed in a moving window containing one modulation period that is centered at each wavelength sequentially, providing at each wavelength the amplitude and the phase of the modulation, and hence the spectral degree and angle of linear

polarization. Further details on the data reduction pipeline will be presented in a forthcoming paper Rietjens et al. (2014). The spectral resolution of the polarization products is usually an order of magnitude lower than the spectrograph's native resolution, because multiple spectral samples per modulation period are needed to accurately determine the modulation's amplitude and phase.

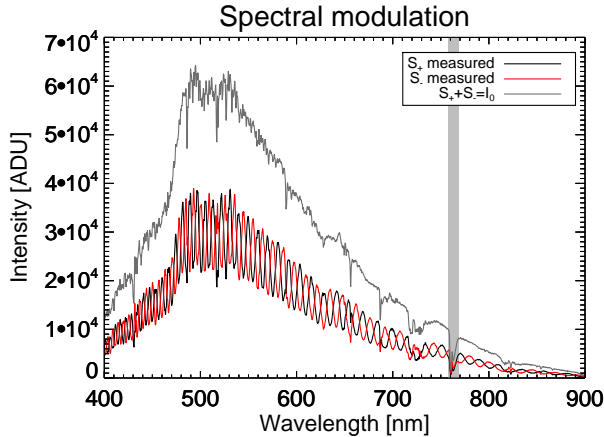


Figure 6.1: Measurement of clear sky polarization with the groundSPEX instrument. Continuum polarization is encoded as the amplitude and phase of the sinusoidal modulation. The sum of the two beams out of the polarizing beam-splitting analyzer is the unmodulated intensity spectrum at the intrinsic resolution. The O_2A absorption band at 760 nm, indicated with the grey band, is clearly visible. The measurement was performed at 4:19 p.m. UTC on July 8, 2013, at the CESAR Observatory, the Netherlands (52.0° N, 4.9° E). The instrument is pointed at zenith, and the solar zenith angle is 59.2° .

6.2.2 Spectral line polarimetry

In applications suitable for channeled spectropolarimetry, the angle of polarization is varying slowly with wavelength. For example, the angle of skylight polarization is mainly determined by the scattering geometry. This allows us to accurately determine the modulation phase $\psi(\lambda)$ through fitting the overall data, and consecutively demodulate the degree of polarization at full spectral resolution, since:

$$\frac{S_+(\lambda) - S_-(\lambda)}{S_+(\lambda) + S_-(\lambda)} = P_L(\lambda) \cos \psi(\lambda), \quad (6.2)$$

provided that $t_+ = t_-$ (see Fig. 6.2). The accuracy of this now purely spatially (de)modulated polarization, albeit at a reduced efficiency of $\cos \psi(\lambda)$, is usually limited by transmission differences (e.g. Snik & Keller 2013, Tyo et al. 2006). Even carefully radiometrically calibrated satellite remote sensing instruments suffer from

differential transmission due to in-flight degradation (e.g. Bermudo et al. 2004). We use the redundancy in the dual-beam modulation to determine $t_-/t_+(\lambda)$ from the data (see Section 6.2.3), to increase the accuracy of the line polarimetry, as well as of the continuum polarimetry through a more accurate sum-spectrum $I_0(\lambda)$.

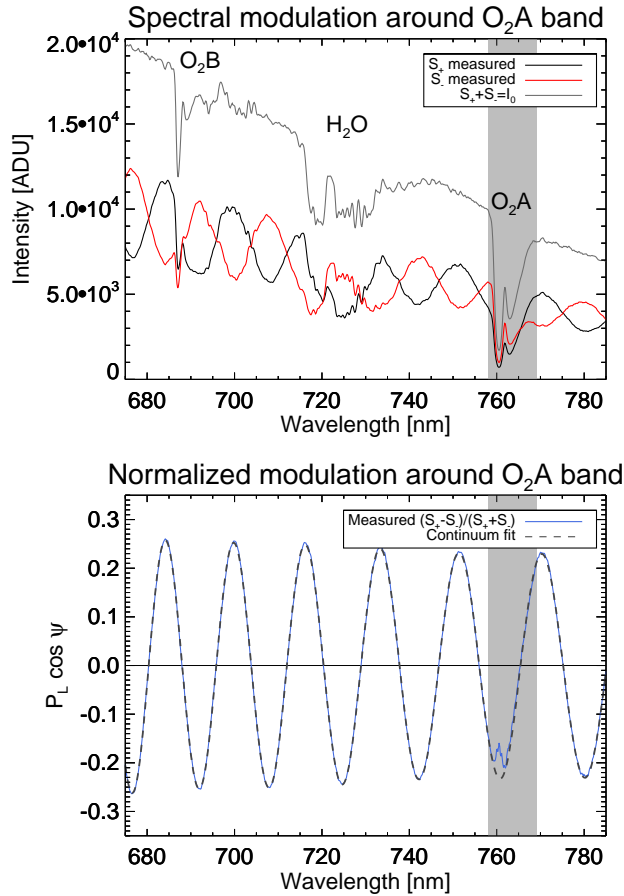


Figure 6.2: Measurement of clear sky polarization with the groundSPEX instrument. *Top.* Same as Fig. 6.1, zoomed in around O_2A band. *Bottom.* The amplitude of the normalized modulation describes the continuum polarization. The phase is the angle of linear polarization, which is known to be constant for scattering polarization. The polarization in the deepest part of the O_2A band is seen to be smaller by ~ 0.07 .

The main limiting factor for line polarimetry is the spectrally varying polarimetric efficiency of $\cos \psi(\lambda)$ (see Eq. (6.2) and Fig. 6.2). At wavelengths where the efficiency is 0 it is impossible to determine the polarization, and in general we have to correct the measurement by a factor $1/\cos \psi$, thereby amplifying measurement errors. This

effect is not extremely restrictive though: if one would allow for an efficiency of 0.5, still 67% of the spectrum can be used at full resolution, and a minimum efficiency of 0.25 translates into 84% of the spectrum. If optimum efficiency in a certain spectral line is required, one could rotate the polarimeter around the optical axis, thereby 'scanning' the line through the modulation pattern. If this is not possible, an alternative solution for the case of atmospheric scattering polarization would be to point at a different sky patch under the same scattering angle, but with the desired $\psi(\lambda)$. If the instrument or platform does not allow for dedicated pointings, but the azimuthal geometry is more or less fixed, e.g., it is continuously scanning the principal plane (defined by the instrument, the target and the sun) one could optimize the retardance δ of the multiple-order-retarder, such that the O₂A band (or any other spectral line) is in a modulation maximum or minimum.

This technique for high-resolution polarization demodulation can be applied to any channeled polarimeter, including imaging and full-Stokes versions. The only requirement is that the phase of the modulation(s) is stable enough to be determined from the continuum polarization. For full-Stokes this not only implies that the angle of linear polarization is stable, but also the amount of circular versus linear polarization. For linear polarimetry this automatically holds true if the circular polarization is orders of magnitude lower, which is often the case (e.g. Kawata 1978), and vice versa.

6.2.3 Transmission correction

The accuracy of the spectral line polarimetry depends on the calibration of the differential transmission. In fact, the redundant spectral and spatial modulation in a dual-beam channeled polarimeter allows for a post-facto extraction of the actual differential transmission $t(\lambda) \equiv t_-/t_+(\lambda)$. The key is the fact that the sum of the modulated beams shows residual modulation in the case that $t \neq 1$. As a consequence, the normalized modulation (Eq. (6.2)) that is ideally centered around 0 will then be offset. This offset can be traced back to the value of $t(\lambda)$. The normalized modulation average is given by:

$$\begin{aligned} \alpha(\lambda) &= \frac{1}{2\pi} \int_0^{2\pi} \frac{S_+(\lambda) - S_-(\lambda)}{S_+(\lambda) + S_-(\lambda)} d\psi \\ &= \frac{(1+t) - 4t/\sqrt{(1+t)^2 - P_L^2(1-t)^2}}{(1-t)}. \end{aligned} \quad (6.3)$$

Even though we cannot solve for $t(\lambda)$ directly, because $P_L(\lambda)$ is unknown, it is still solvable in an iterative way: after determining $\alpha(\lambda)$, the differential transmission $t(\lambda)$ is calculated assuming $P_L = 0$, i.e.:

$$\alpha(\lambda) \approx \alpha(\lambda) \Big|_{P_L=0} = \frac{1-t(\lambda)}{1+t(\lambda)}. \quad (6.4)$$

The measured spectrum $S_-(\lambda)$ is then corrected by dividing it by the thus obtained $t(\lambda)$, after which the process repeats. The deviation between the iterated function

and the $t(\lambda)$ is largest for $P_L = 1$, when:

$$\alpha(\lambda) \Big|_{P_L=1} = \frac{1 - \sqrt{t(\lambda)}}{1 + \sqrt{t(\lambda)}}, \quad (6.5)$$

so, worst case, at each iteration we find the square root of the actual corrected differential transmission value. Hence, after n iterations the corrected t approaches unity at least to within $\sqrt[n]{t}$. For example, in only 3 iterations a differential transmission of $t = 0.95$ is corrected to at least 0.994, which decreases the error in the line polarization by an order of magnitude, as explained in Section 6.3. The correction algorithm is stopped after 3 iterations, because at this point the corrected $\alpha(\lambda)$ is closer to 0 than the true α is known, because of imperfections in the data such as residual dark signal, noise or uneven spectral sampling across a modulation period. A residual offset in the normalized modulation is fitted along with the spectral window fit for the degree and angle of linear polarization. This powerful correction algorithm is not only vital for accurate line polarimetry, but continuum polarimetry also benefits due to the increased accuracy of the determined unmodulated intensity spectrum $I_0(\lambda)$ as the sum of the two modulated spectra. A more complete error analysis for both line and continuum polarimetry is performed in Section 6.3.

Note that residual dark signal can also offset the normalized modulation. Even though it is a fair assumption that the offset is mainly caused by differential transmission, particularly in the continuum, which is where the differential transmission correction technique applies, the effect of residual dark current on the correction quality will be investigated in Section 6.3.1.

6.3 Error analysis

It is important to realize that the propagation of measurement errors is different for the pixel to pixel calculation of the polarization than for the continuum polarimetry.

First of all, in spectral line polarimetry errors in $\psi(\lambda)$ propagate to the polarization measurement, because of the correction for the limited efficiency (see Eq. (6.2)). If polarization is modulated with $\cos(\psi)$ and demodulated with $\cos(\psi + \Delta\psi)$, a scaling error of the size of the ratio of the two cosines is introduced. Note that this ratio strongly depends on the phase ψ itself, such that at a modulation maximum or minimum a shift in the correction wave has almost no effect, but closer to the zero efficiency points this error is greatly amplified. Within $\pm\pi/4$ from a modulation maximum or minimum, where we would like to perform line polarimetry because the efficiency is rather high with at least 70%, the ratio is fairly linear. For example, at $\psi = \pi/4$ an uncertainty of 1° in the angle of polarization ϕ_L , which is realistic in the vicinity of an absorption band, translates into a relative polarization error of 0.037, i.e. an absolute error of almost 0.01 at $P_L = 0.25$.

In addition to a differential transmission, the measured spectra can suffer from a residual dark signal, composed of a systematic bias drift Δd and random variations

σd_{\pm} for each pixel, due to shot noise and readout noise, i.e.:

$$S'_{\pm}(\lambda) = S_{\pm}(\lambda) + \Delta d + \sigma d_{\pm}(\lambda). \quad (6.6)$$

The bias drift, which is mainly caused by temperature changes, is assumed equal for both spectra, because the spectra are usually measured on the same detector, or on two identical detectors. In the following error analysis, the spectral line polarization is calculated according to:

$$P'_{L, \text{line}} = \left. \frac{S'_+ - S'_-}{S'_+ + S'_-} \right|_{\psi=0}, \quad (6.7)$$

and the continuum polarization is described by:

$$P'_{L, \text{cont}} = \frac{1}{2} \left(\left. \frac{S'_+ - S'_-}{S'_+ + S'_-} \right|_{\psi=0} - \left. \frac{S'_+ - S'_-}{S'_+ + S'_-} \right|_{\psi=\pi} \right). \quad (6.8)$$

Note that the line polarimetry is assumed to be performed at maximum efficiency, and therefore the presented line performance represents a best case scenario. Also note the use of the direct calculation of the modulation amplitude in Eq. (6.8) for reproducibility; in reality all samples inside a spectral window are used for the determination of the continuum polarization (except for those in a polarized spectral line), and random noise will therefore have a less prominent influence than for line polarimetry.

Spectral line polarization is much more susceptible to residual dark current than the continuum for the following reasons:

- The signal in absorption lines is lower, so the dark is relatively higher.
- Measurement noise, including noise in the dark current, largely averages out when fitting spectrally modulated continuum polarization across a sampled period, whereas in line polarimetry we see the noise in each pixel. Therefore, for continuum polarimetry we set $\sigma d_{\pm} = 0$.
- Residual dark offsets the spectra much more than it affects the modulation amplitude. In fact, for unpolarized light there is no modulation at all, so the continuum polarization is free from dark errors.

The polarization error due to all these effects combined, in the absence of differential transmission ($t = 1$), is compared for line and continuum polarization in Fig. 6.3, as the difference between the perturbed polarization according to Eq. (6.7) or Eq. (6.8) and the true polarization ($\Delta d = \sigma d_+ = \sigma d_- = 0$). The realistic perturbation values in analog to digital units (ADU) are $\Delta d = 9$, $\sigma d_+ = -\sigma d_- = -6$ and $s_0 \equiv t_+ I_0 = 1500$ for the absorption line, and $d = 9$, $\sigma d_+ = \sigma d_- = 0$ and $s_0 = 8000$ for the continuum right outside the line, corresponding to the O₂A absorption band measurement in Figs. 6.1 and 6.2.

The error in the continuum polarization goes to 0 for $P_L = 0$, because in that case there is just no spectral modulation pattern (the amplitude is 0). Since line polarization cannot make use of this spectral patterning, the instantaneous pixel values are directly translated into polarization, leaving it an order of magnitude more susceptible to dark errors. For a clean comparison of the two modulation techniques, Fig. 6.3 also shows continuum polarimetry with the intensities and dark errors as for the line polarimetry. The remaining performance difference stems from the fact that for line polarimetry there is an additive term ($\sigma d_+ - \sigma d_-$) in both the nominator and denominator in Eq. (6.7), whereas for continuum polarimetry that term cancels out in the nominator, thanks to the double difference technique in Eq. (6.8). That makes the continuum polarization error go to 0 for $P_L = 0$, and yields an overall smaller susceptibility to dark current for channeled polarimetry.

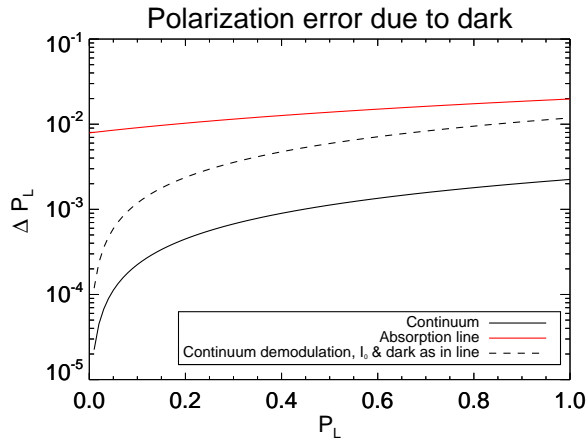


Figure 6.3: Absolute error in the polarization measurement due to uncorrected dark signal, as a function of the degree of polarization. Spectral modulation of continuum polarization is at least an order of magnitude less susceptible to residual dark current than the classic spatial modulation, as applied in spectral lines.

The effect of differential transmission alone ($\Delta d = \sigma d_+ = \sigma d_- = 0$) is shown in Fig. 6.4. The polarimetric errors are plotted for a realistic value of $t = 0.95$, as well as for $t = 0.9998$ which would be achievable using the differential transmission correction algorithm (see Section 6.2.3). The figure shows that this new technique yields an improvement of two orders of magnitude for line polarimetry and even more for continuum polarimetry. Note that it is impossible to achieve the aforementioned corrected differential transmission value by flat-fielding alone. Flat-fielding can become challenging beyond the 0.999 level, because the source has to be unpolarized in order not to introduce a spurious polarization modulation pattern. Moreover, dynamic effects like post-calibration degradation or viewing angle dependent stray light, require a post-processing correction, where the differential transmission is

deduced from the measured spectra themselves.

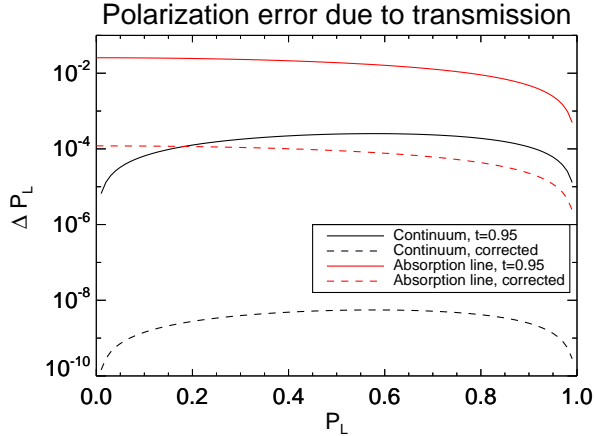


Figure 6.4: Absolute error in the polarization measurement due to differential transmission in the two beams out of the polarizing beam-splitter, as a function of the degree of polarization. The transmission correction algorithm of Section 6.2.3 decreases the polarization error by two orders of magnitude for spectral line polarimetry, and even more for continuum polarimetry.

6.3.1 Transmission correction with residual dark signal

Encouraged by the performance of the correction algorithm for differential transmission (see Fig. 6.4), numerical calculations of the impact of residual dark on the correction have been performed. For reasonable residual dark and differential transmission values, the transmission correction always improves the accuracy of the polarization measurement. However, in case of residual dark, the corrected t converges to a value different than 1. For the aforementioned case of $t = 0.95$ and a residual dark current of $\Delta d = 9$ at a signal of $s_0 = 8000$ ADU, the deviation from 1 of the corrected t is between $1 \cdot 10^{-4}$ and $2 \cdot 10^{-4}$, depending on the degree of polarization. The corresponding total impact of the imperfect differential transmission correction due to the residual dark current, and the dark itself, is shown in Fig. 6.5. The transmission correction performance is most noticeable for line polarimetry at lower degrees of polarization, where the error decreases from ~ 0.03 to ~ 0.01 .

6.4 Application of line polarimetry to the O₂A absorption band

We measured the scattering polarization of a clear sky in the O₂A absorption band with one of our SPEX instruments (see Figs. 6.1 and 6.2). This groundSPEX in-

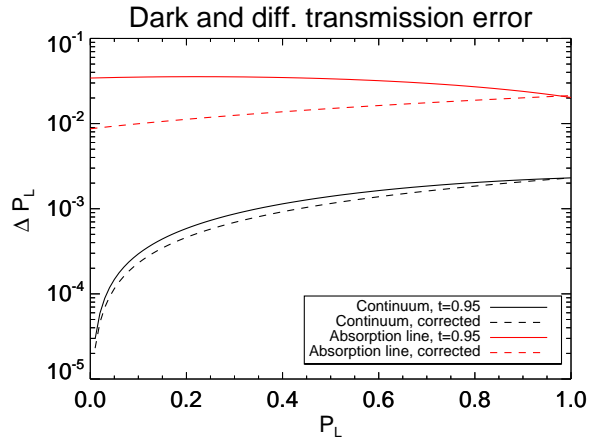


Figure 6.5: Absolute error in the polarization due to the combination of residual dark current and the corresponding imperfectly corrected differential transmission, as a function of the degree of polarization. The parameter values are adopted from the O_2A absorption band measurement in Figs. 6.1 and 6.2.

strument is a dedicated ground-based spectropolarimeter for aerosol measurements, based on spectral modulation van Harten et al. (2014a). It is mounted on a motorized altazimuth mount, and employs two synchronized fiber-fed spectrographs at 360–910 nm with a resolution of ~ 0.8 nm. The measurement was performed on July 8, 2013, at the Cabauw Experimental Site for Atmospheric Research (CESAR) in the Netherlands, also known as Cabauw (<http://www.cesar-observatory.nl>). The instrument pointed at zenith, and the solar zenith angle was 59.2° .

When fitting the continuum modulation, the O_2A band itself is excluded, in order to get more realistic fits for the amplitude to enable a better comparison between continuum and line polarization. Moreover, since the modulation in the band is distorted, it may lead to erroneous values for the phase, which leads to errors in the efficiency correction. The determined continuum polarization (using the spectral modulation) and line polarization (using pixel to pixel demodulation) are shown in Fig. 6.6. The error bars include the imperfect transmission correction due to residual dark signal, as well as the dark signal itself, taking into account the wavelength dependent intensity and polarization, i.e. the error bars in the deepest part of the line are adopted from Fig. 6.5. For line polarimetry the error due to the uncertainty of 1° in the modulation phase is quadratically added. Outside the absorption band the results of continuum and line polarimetry are consistent. In the deepest part of the O_2A band we find a polarization of 0.160 ± 0.010 , significantly different from the 0.2284 ± 0.0004 in the continuum. For comparison, the (erroneous) values we find without applying the transmission correction are 0.136 ± 0.035 and 0.2277 ± 0.0007 . Hence, the transmission correction reduces the error in the line polarization by

0.024 and the error in the continuum polarization by $7 \cdot 10^{-4}$, and the corresponding uncertainties decrease as well.

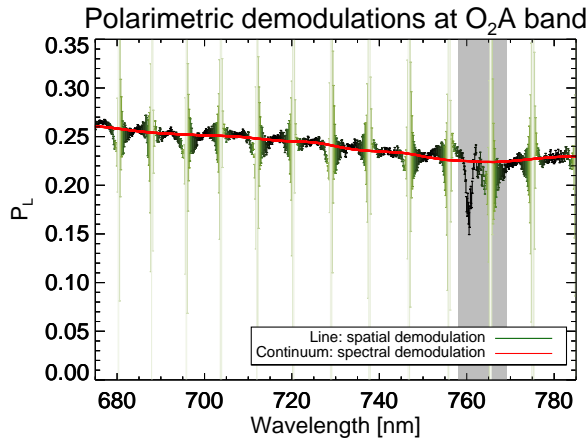


Figure 6.6: Measured clear sky polarization in the Oxygen A absorption band, and in the continuum around it, with a dual-beam channeled spectropolarimeter (groundSPEX). The raw spectrally modulated measurements are shown in Figs. 6.1 and 6.2. Polarization in the deepest parts of the band is significantly different from the continuum. The color of the line polarization is scaled with the polarimetric efficiency for better visibility.

Due to the high optical thickness in the absorption band, the light that reaches the instrument is scattered relatively high up in the atmosphere and underwent relatively few scattering events, to minimize the path length through the atmosphere and the probability of extinction. In the common case where the aerosols are located in the boundary layer, this leads to a higher polarization in the absorption band, as seen by Aben et al. (1999), Boesche et al. (2008). However, the measured depolarization implies that part of the aerosols are at high altitudes, as measured and interpreted by Stammes et al. (1994), Boesche et al. (2008), Stam et al. (1999). Lidar vertical profiles Apituley et al. (2009) confirm that the aerosols were divided into two bands, one at 2 km altitude and one at 3 – 5 km, and there is no cirrus at the time and location of measurement. In fact, longer term satellite observations with e.g. CALIOP onboard CALIPSO Vaughan et al. (2004), MODIS onboard Aqua and Terra Remer et al. (2005), GOME-2 onboard MetOp-A and MetOp-B de Graaf et al. (2005) and OMI onboard Aura Levelt et al. (2006) show the higher aerosols drifting in from wildfires in Canada.

Note that the polarization only deviates at extremely high optical thickness. The less deep parts of the band, as well as the entire H₂O band at ~ 725 nm that is less optically thick, do not show a significant change in polarization, an effect that was already noticeable in the normalized modulation (see Fig. 6.2). The deeper parts of the O₂B band at ~ 690 nm happen to coincide with a zero-crossing of the modu-

lation (see Fig. 6.2), so there is no efficient measurement available, unfortunately. The measured polarization spectrum shows close resemblance with the measurement by Stammes et al. (1994) at a higher spectral resolution of 0.3 nm, in terms of continuum polarization, O₂A band polarization, and the absence of differential polarization in the H₂O and O₂B bands. However, simulations by Pust & Shaw (2012) and measurements by Aben et al. (1999), who both obtain much stronger differential polarization in the O₂A band, albeit an increase instead of a decrease in polarization, do show polarization signatures in the H₂O and O₂B bands. This implies that an even higher aerosol optical thickness at higher altitudes would lead to depolarization in weaker spectral bands as well.

The error in the continuum polarimetry is so low that photon noise is not negligible anymore. Per measurement 50 spectra are averaged, and about 20 pixels describe one modulation period around the O₂A band, therefore the uncertainty in the continuum polarization due to photon noise is $\sim 2 \cdot 10^{-4}$. The line polarization accuracy is currently limited by the uncertainty in the dark current. Not only the dark itself, but also the resulting error in the transmission correction propagates to the polarimetric error. Currently the dark spectra are calibrated offline for a range of exposure times and temperatures, and a number of optically masked pixels indicate the actual dark signal at the time of measurement. Switching to a cooled detector would strongly decrease this error source, leaving an error of $\sim 10^{-3}$ in line polarization (Fig. 6.3 drops by an order of magnitude for a residual dark of 1 ± 1 ADU).

6.5 Conclusions

We successfully measured line polarization with a spectral polarization modulator. This is possible because the dual-beam implementation allows for a demodulation of the polarization at the full spectral resolution. Several observing strategies are proposed to circumvent the wavelength dependency of the efficiency of the line polarimetry. We employed the redundancy in the both spectrally and spatially modulated polarization to derive the differential transmission and correct for it in post-processing. This reduces the line polarization error from 0.034 to 0.010 for our groundSPEX instrument. The remaining error is dominated by the uncertainty in the residual dark. The same instrument with a cooled detector would be able to measure both continuum and line polarization with an uncertainty of $\lesssim 10^{-3}$. The polarization of skylight in the Oxygen A band compared to the continuum provides important information on the vertical distribution of atmospheric aerosols. This altitude information is complementary to aerosol characterization using accurate continuum polarimetry, and is now complimentary with a dual-beam spectral modulator like SPEX, in contrast to filter-based polarimeters. The presented techniques of full resolution polarimetry and differential transmission correction are applicable to any kind of dual-beam channeled polarimeter, including imaging and full-Stokes versions.

Acknowledgements

GvH acknowledges Utrecht University for funding his research. The groundSPEX instrument was developed for the National Institute for Public Health and the Environment (RIVM). The CESAR Observatory is operated by the Royal Netherlands Meteorological Institute (KNMI). We gratefully acknowledge Piet Stammes for stimulating discussions and valuable comments on an earlier version of the manuscript. We thank the anonymous reviewers for their helpful comments.

Bibliography

- Aben, I., Helderma, F., Stam, D. M., & Stammes, P. 1999, *Geophysical Research Letters*, 26, 591 (cited on pages 40, 127, and 128)
- Alenin, A. S. & Tyo, J. S. 2014, *Journal of the Optical Society of America A*, 31, 1013 (cited on pages 24 and 49)
- Anderson, J. O., Thundiyl, J. G., & Stolbach, A. 2011, *Journal of Medical Toxicology*, 8, 166 (cited on page 6)
- Apituley, A., Russchenberg, H., van der Marel, H., et al. 2008, in *IEEE International Geoscience and Remote Sensing Symposium, IGARSS 2008*, July 8-11, 2008, Boston, Massachusetts, USA, Proceedings, 903–906 (cited on page 107)
- Apituley, A., Wilson, K. M., Potma, C., Volten, H., & de Graaf, M. 2009, in *Proceedings of the 8th International Symposium on Tropospheric Profiling*, ed. A. Apituley, H. W. J. Russchenberg, & W. A. A. Monna (cited on page 127)
- Bagnulo, S., Landolfi, M., Landstreet, J. D., et al. 2009, *Publications of the Astronomical Society of the Pacific*, 121, 993 (cited on pages 19 and 46)
- Basilevsky, A. T. & Head, J. W. 2003, *Reports on Progress in Physics*, 66, 1699 (cited on page 2)
- Baur, T. 2005, A new type of beam splitting polarizer cube (cited on page 58)
- Beckers, J. M. 1971, *Applied Optics*, 10, 973 (cited on page 59)
- Beelen, R., Raaschou-Nielsen, O., & Stafoggia, M., e. a. 2014, *The Lancet*, 383, 785 (cited on pages 98 and 117)
- Bermudo, F., Fougny, B., & Bret Dibat, T. 2004, in *ESA Special Publication, Vol. 554, 5th International Conference on Space Optics*, ed. B. Warmbein, 129–135 (cited on page 120)
- Boesche, E., Stammes, P., Preusker, R., et al. 2008, *Applied Optics*, 47, 3467 (cited on pages 118 and 127)
- Boesche, E., Stammes, P., Ruhtz, T., Preusker, R., & Fischer, J. 2006, *Applied Optics*, 45, 8790 (cited on pages 99, 105, and 116)
- Buczkowski, S., Martins, J., Fernandez-Borda, R., Cieslak, D., & Hall, J. 2013, *AGU Fall Meeting Abstracts*, F126 (cited on page 19)

- Cairns, B., Russell, E. E., LaVeigne, J. D., & Tennant, P. M. W. 2003, in *Society of Photo-Optical Instrumentation Engineers (SPIE) Conference Series*, Vol. 5158, *Polarization Science and Remote Sensing*, ed. J. A. Shaw & J. S. Tyo, 33–44 (cited on page 18)
- Coffeen, D. L. & Gehrels, T. 1969, *Astronomical Journal*, 74, 433 (cited on page 2)
- Collett, E. 2005, *Field Guide to Polarization (SPIE)* (cited on page 11)
- Craven, J. & Kudenov, M. W. 2010, *Optical Engineering*, 49, 053602 (cited on pages 46, 49, 76, and 117)
- Dahlberg, A. R. 2010, Master's thesis, Montana State University (cited on page 105)
- de Graaf, M., Stammes, P., Torres, O., & Koelemeijer, R. B. A. 2005, *Journal of Geophysical Research*, 110, 1201 (cited on page 127)
- de Juan Ovelar, M., Snik, F., & Keller, C. U. 2011, in *Society of Photo-Optical Instrumentation Engineers (SPIE) Conference Series*, Vol. 8160, *Society of Photo-Optical Instrumentation Engineers (SPIE) Conference Series* (cited on pages 20, 24, and 47)
- del Toro Iniesta, J. C. & Collados, M. 2000, *Applied Optics*, 39, 1637 (cited on pages 17, 24, 50, and 51)
- Di Noia, A., Hasekamp, O. P., van Harten, G., et al. 2014, *Atmospheric Measurement Techniques Discussions*, 7, 9047 (cited on page 108)
- Diner, D. J., Beckert, J. C., Reilly, T. H., et al. 1998, *IEEE Transactions on Geoscience and Remote Sensing*, 36, 1072 (cited on page 14)
- Diner, D. J., Chipman, R. A., Beaudry, N. A., et al. 2005, in *Society of Photo-Optical Instrumentation Engineers (SPIE) Conference Series*, Vol. 5659, *Enabling Sensor and Platform Technologies for Spaceborne Remote Sensing*, ed. G. J. Komar, J. Wang, & T. Kimura, 88–96 (cited on page 75)
- Diner, D. J., Davis, A., Hancock, B., et al. 2010, *Applied Optics*, 49, 2929 (cited on page 18)
- Diner, D. J., Davis, A., Hancock, B., et al. 2007, *Applied Optics*, 46, 8428 (cited on page 75)
- Dodge, M. J. 1984, *Applied Optics*, 23, 1980 (cited on page 82)
- Dollfus, A. 1966, in *Caltech-JPL Lunar and Planetary Conference*, ed. H. Brown, G. J. Stanley, D. O. Muhleman, & G. Münch, 187 (cited on page 2)
- Dollfus, A. & Coffeen, D. L. 1970, *Astronomy and Astrophysics*, 8, 251 (cited on page 2)
- Dong, H., Tang, M., & Gong, Y. 2012, *Optics Express*, 20, 26649 (cited on page 47)
- Dubovik, O. & King, M. D. 2000, *Journal of Geophysical Research*, 105, 20673 (cited on pages 99 and 110)
- Dubovik, O., Sinyuk, A., Lapyonok, T., et al. 2006, *Journal of Geophysical Research*, 111, 11208 (cited on pages 12 and 110)

- Dubovik, O., Smirnov, A., Holben, B. N., et al. 2000, *Journal of Geophysical Research*, 105, 9791 (cited on pages 14 and 110)
- EASA. 2013, *EASA Safety Information Bulletin*, Tech. Rep. 2010-17R5, European Aviation Safety Agency (cited on page 6)
- Eck, T. F., Holben, B. N., Reid, J. S., et al. 1999, *Journal of Geophysical Research*, 104, 31333 (cited on page 108)
- Eftimov, T., Kortenski, T., & Dimitrov, D. 1991, *Journal of Modern Optics*, 38, 519 (cited on page 94)
- Evans, J. W. 1949, *Journal of the Optical Society of America (1917-1983)*, 39, 229 (cited on page 64)
- Fernandez Borda, R. A. & Martins, J. 2013, *AGU Fall Meeting Abstracts* (cited on page 75)
- Frecker, J. E. & Serkowski, K. 1976, *Applied Optics*, 15, 605 (cited on page 59)
- Gelest. 2012, *Silicone fluids: stable, inert media*, Tech. rep., Gelest, Inc. (cited on page 67)
- Ghosh, G. 1998, *Handbook of Optical Constants of Solids: Handbook of Thermo-Optic Coefficients of Optical Materials with Applications*, *Handbook of optical constants of solids* (Elsevier Science) (cited on pages 61 and 82)
- Green, D. B. 2001, *Satellite Contamination and Materials Outgassing Knowledgebase - An Interactive Database Reference*, Tech. Rep. M-1010, Physical Sciences, Inc. (cited on page 66)
- Hagen, N., Oka, K., & Dereniak, E. L. 2007, *Optics Letters*, 32, 2100 (cited on page 116)
- Hagolle, O., Goloub, P., Deschamps, P.-Y., et al. 1999, *IEEE Transactions on Geoscience and Remote Sensing*, 37, 1550 (cited on page 18)
- Hale, P. D. & Day, G. W. 1988, *Applied Optics*, 27, 5146 (cited on pages 61 and 64)
- Hansen, J., Lacic, A., Ruedy, R., & Sato, M. 1993, *National Geographic Research and Exploration*, 9, 142 (cited on page 4)
- Hansen, J., Rossow, W., Carlson, B., et al. 1995, *Climatic Change*, 31, 247 (cited on page 15)
- Hansen, J. E. 1971, *Journal of Atmospheric Sciences*, 28, 120 (cited on page 2)
- Hansen, J. E. & Hovenier, J. W. 1974, *Journal of Atmospheric Sciences*, 31, 1137 (cited on pages 2, 3, and 46)
- Hansen, J. E. & Travis, L. D. 1974, *Space Science Reviews*, 16, 527 (cited on pages 14 and 75)
- Hasekamp, O. P. 2010, *Atmospheric Measurement Techniques*, 3, 839 (cited on pages 14, 15, and 16)
- Hasekamp, O. P. & Landgraf, J. 2002, *Journal of Quantitative Spectroscopy and Radiative Transfer*, 75, 221 (cited on page 12)

- Hasekamp, O. P. & Landgraf, J. 2005, *Journal of Geophysical Research*, 110, 4203 (cited on pages 12, 40, and 108)
- Hasekamp, O. P. & Landgraf, J. 2007, *Applied Optics*, 46, 3332 (cited on pages 14, 15, 29, 46, 47, 75, 99, and 117)
- Haywood, J. & Boucher, O. 2000, *Reviews of Geophysics*, 38, 513 (cited on page 75)
- Hecht, E. 2002, *Optics*, 4th edn. (Addison-Wesley) (cited on page 9)
- Hemminger, C. S. 1992, Surface contamination on LDEF exposed materials, Tech. Rep. TR-92(2935)-11, The Aerospace Corporation (cited on page 67)
- Hessel, A. & Oliner, A. A. 1965, *Applied Optics*, 4, 1275 (cited on page 93)
- Holben, B. N., Eck, T. F., Slutsker, I., et al. 1998, *Remote Sensing of Environment*, 66, 1 (cited on pages 7, 99, 107, and 108)
- Hovenier, J. W. 1971, *Astronomy and Astrophysics*, 13, 7 (cited on page 2)
- Ichimoto, K., Suematsu, Y., Shimizu, T., et al. 2007, in *Astronomical Society of the Pacific Conference Series*, Vol. 369, *New Solar Physics with Solar-B Mission*, ed. K. Shibata, S. Nagata, & T. Sakurai, 39–42 (cited on page 20)
- IPCC. 2007, in *Climate Change 2007: The Physical Science Basis. Contribution of Working Group I to the Fourth Assessment Report of the Intergovernmental Panel on Climate Change*, ed. S. Solomon, D. Qin, M. Manning, Z. Chen, M. Marquis, K. B. Averyt, M. Tignor, & H. L. Miller (Cambridge University Press, Cambridge, United Kingdom and New York, NY, USA) (cited on pages 29 and 42)
- IPCC. 2013, in *Climate Change 2013: The Physical Science Basis. Contribution of Working Group I to the Fifth Assessment Report of the Intergovernmental Panel on Climate Change.*, ed. T. F. Stocker, D. Qin, G.-K. Plattner, M. Tignor, S. K. Allen, J. Boschung, A. Nauels, Y. Xia, V. Bex, & P. M. Midgley (Cambridge, United Kingdom and New York, NY, USA: Cambridge University Press) (cited on pages 5, 98, and 117)
- Jeppesen, M. A. 1958, *Journal of the Optical Society of America*, 48, 629 (cited on page 60)
- Jones, R. V. & Richards, J. C. S. 1954, *Proceedings of the Royal Society of London. Series A, Mathematical and Physical Sciences*, 225, 122 (cited on page 93)
- Karalidi, T., Stam, D. M., & Hovenier, J. W. 2012, *Astronomy and Astrophysics*, 548, A90 (cited on page 2)
- Kaufman, Y. J., Koren, I., Remer, L. A., Rosenfeld, D., & Rudich, Y. 2005, *Proceedings of the National Academy of Science*, 102, 11207 (cited on page 4)
- Kawata, Y. 1978, *Icarus*, 33, 217 (cited on pages 11, 117, and 121)
- Keller, C. U. 2002, in *Astrophysical Spectropolarimetry*, ed. J. Trujillo-Bueno, F. Moreno-Insertis, & F. Sánchez, 303–354 (cited on pages 19 and 63)
- Keller, C. U., Schmid, H. M., Venema, L. B., et al. 2010, in *Society of Photo-Optical Instrumentation Engineers (SPIE) Conference Series*, Vol. 7735, *Society of Photo-Optical Instrumentation Engineers (SPIE) Conference Series* (cited on page 46)

- Keller, C. U. & Snik, F. 2009, in *Astronomical Society of the Pacific Conference Series*, Vol. 405, *Solar Polarization 5: In Honor of Jan Stenflo*, ed. S. V. Berdyugina, K. N. Nagendra, & R. Ramelli, 371–382 (cited on page 47)
- Knobelspiesse, K., Cairns, B., Redemann, J., Bergstrom, R. W., & Stohl, A. 2011, *Atmospheric Chemistry & Physics*, 11, 6245 (cited on page 14)
- Knollenberg, R. G. & Hunten, D. M. 1980, *Journal of Geophysical Research*, 85, 8039 (cited on page 2)
- Krijger, J. M., Snel, R., van Harten, G., Rietjens, J. H. H., & Aben, I. 2014, *Atmospheric Measurement Techniques Discussions*, 7, 1213 (cited on page 67)
- Kudenov, M. W. & Dereniak, E. L. 2012, *Optics Express*, 20, 17973 (cited on page 116)
- Kudenov, M. W., Escuti, M. J., Dereniak, E. L., & Oka, K. 2011, *Applied Optics*, 50, 2283 (cited on page 116)
- Kudenov, M. W., Escuti, M. J., Hagen, N., Dereniak, E. L., & Oka, K. 2012, *Optics Letters*, 37, 1367 (cited on page 116)
- Kudenov, M. W. & Goldstein, D. H. 2011, in *Polarized Light*, 3rd edn., ed. D. H. Goldstein (CRC Press), 401–433 (cited on pages 25, 46, 74, and 116)
- Kudenov, M. W., Hagen, N. A., Dereniak, E. L., & Gerhart, G. R. 2007, *Optics Express*, 15, 12792 (cited on page 47)
- L'Ecuyer, T. S. & Jiang, J. H. 2010, *Physics Today*, 63, 36 (cited on page 75)
- Lemmen, M. H. J. 2009, *SPEX breadboard thermo mechanical analysis and design*, Tech. Rep. TNO-PEP-SPEXBB-RP-003, TNO (cited on pages 60 and 62)
- Levelt, P. F., van den Oord, G. H. J., Dobber, M. R., et al. 2006, *IEEE Transactions on Geoscience and Remote Sensing*, 44, 1093 (cited on page 127)
- Li, Z., Goloub, P., Dubovik, O., et al. 2009, *Journal of Quantitative Spectroscopy and Radiative Transfer*, 110, 1954 (cited on pages 14, 99, and 105)
- Lide, D. R., ed. 2005, *Thermal and physical properties of pure metals*, *CRC Handbook of Chemistry and Physics*, Internet Version 2005 (CRC Press) (cited on page 62)
- Lyt, B. 1929, *Annales de l'Observatoire de Paris, Section de Meudon*, 8 (cited on page 2)
- Lyt, B. 1933, *Comptes Rendus de l'Académie des Sciences*, 197, 1593 (cited on page 116)
- Macleod, H. A. 2010, *Thin-film optical filters*, 4th edn., *Series in Optics and Optoelectronics* (CRC Press) (cited on page 66)
- Mahler, A.-B. & Chipman, R. A. 2011, *Applied Optics*, 50, 1726 (cited on pages 56 and 85)
- Mahler, A.-B., Diner, D. J., & Chipman, R. A. 2011a, *Applied Optics*, 50, 2080 (cited on pages 24 and 47)
- Mahler, A.-B., McClain, S., & Chipman, R. 2011b, *Applied Optics*, 50, 755 (cited on page 61)

- Manolis, I., Grabarnik, S., Caron, J., et al. 2013, in Society of Photo-Optical Instrumentation Engineers (SPIE) Conference Series, Vol. 8889, Society of Photo-Optical Instrumentation Engineers (SPIE) Conference Series (cited on page 75)
- Markwardt, C. B. 2009, in Astronomical Society of the Pacific Conference Series, Vol. 411, Astronomical Data Analysis Software and Systems XVIII, ed. D. A. Bohlender, D. Durand, & P. Dowler, 251–254 (cited on page 82)
- Marov, M. I., Lystsev, V. E., Lebedev, V. N., Lukashevich, N. L., & Shari, V. P. 1980, *Icarus*, 44, 608 (cited on page 2)
- Martins, J., Fernandez-Borda, R., Remer, L. A., et al. 2013, AGU Fall Meeting Abstracts (cited on page 75)
- Martonchik, J. V., Diner, D. J., Kahn, R. A., et al. 1998, *IEEE Transactions on Geoscience and Remote Sensing*, 36, 1212 (cited on page 14)
- McClain, S. C., Bartlett, C. L., Pezzaniti, J. L., & Chipman, R. A. 1994, in Society of Photo-Optical Instrumentation Engineers (SPIE) Conference Series, Vol. 2260, Stray Radiation in Optical Systems III, ed. R. P. Breault, 140–144 (cited on page 86)
- McCormick, R. A. & Ludwig, J. H. 1967, *Science*, 156, 1358 (cited on page 4)
- McMullin, D. R., Judge, D. L., Hilchenbach, M., et al. 2002, *ISSI Scientific Reports Series*, 2, 135 (cited on page 67)
- McMurry, P. H. 2000, *Atmospheric Environment*, 34, 1959 (cited on page 98)
- Mie, G. 1908, *Annalen der Physik*, 330, 377 (cited on page 8)
- Mishchenko, M. I., Cairns, B., Hansen, J. E., et al. 2004, *Journal of Quantitative Spectroscopy and Radiative Transfer*, 88, 149 (cited on pages 15, 16, 75, 99, and 117)
- Mishchenko, M. I., Hovenier, J. W., & Travis, L. D., eds. 2000, *Light Scattering by Nonspherical Particles* (Academic Press) (cited on page 8)
- Mishchenko, M. I. & Travis, L. D. 1997, *Journal of Geophysical Research*, 102, 16989 (cited on pages 10, 14, 29, 46, 47, 75, and 99)
- Mu, T., Zhang, C., Jia, C., et al. 2013, *Optics Communications*, 294, 88 (cited on page 47)
- Murayama, T., Okamoto, H., Kaneyasu, N., Kamataki, H., & Miura, K. 1999, *Journal of Geophysical Research*, 104, 31781 (cited on pages 7 and 98)
- Nordsieck, K. H. 1974, *Publications of the Astronomical Society of the Pacific*, 86, 324 (cited on pages 46, 74, and 116)
- Oka, K. & Kaneko, T. 2003, *Optics Express*, 11, 1510 (cited on page 116)
- Oka, K. & Kato, T. 1999, *Optics Letters*, 24, 1475 (cited on pages 46, 49, 74, and 116)
- Oka, K. & Saito, N. 2006, in Society of Photo-Optical Instrumentation Engineers (SPIE) Conference Series, Vol. 6295, Society of Photo-Optical Instrumentation Engineers (SPIE) Conference Series (cited on page 116)

- Okabe, H., Hayakawa, M., Matoba, J., Naito, H., & Oka, K. 2009, *Review of Scientific Instruments*, 80, 083104 (cited on page 47)
- O'Neill, N. T., Dubovik, O., & Eck, T. F. 2001, *Applied Optics*, 40, 2368 (cited on page 110)
- O'Neill, N. T., Eck, T. F., Smirnov, A., Holben, B. N., & Thulasiraman, S. 2003, *Journal of Geophysical Research*, 108, 4559 (cited on pages 99 and 110)
- Peralta, R. J., Nardell, C., Cairns, B., et al. 2007, in *Society of Photo-Optical Instrumentation Engineers (SPIE) Conference Series*, Vol. 6786, *Society of Photo-Optical Instrumentation Engineers (SPIE) Conference Series* (cited on page 75)
- Persh, S., Shaham, Y. J., Benami, O., et al. 2010, in *Society of Photo-Optical Instrumentation Engineers (SPIE) Conference Series*, Vol. 7807, *Society of Photo-Optical Instrumentation Engineers (SPIE) Conference Series* (cited on page 75)
- Pust, N. J., Dahlberg, A. R., Thomas, M. J., & Shaw, J. A. 2011, *Optics Express*, 19, 18602 (cited on page 112)
- Pust, N. J. & Shaw, J. A. 2006, *Applied Optics*, 45, 5470 (cited on page 116)
- Pust, N. J. & Shaw, J. A. 2008, *Applied Optics*, 47, 190 (cited on page 14)
- Pust, N. J. & Shaw, J. A. 2012, *Optics Express*, 20, 15559 (cited on page 128)
- Ragent, B. & Blamont, J. 1980, *Journal of Geophysical Research*, 85, 8089 (cited on page 2)
- Ramanathan, V. & Carmichael, G. 2008, *Nature Geoscience*, 1, 221 (cited on page 4)
- Ramanathan, V., Crutzen, P. J., Kiehl, J. T., & Rosenfeld, D. 2001, *Science*, 294, 2119 (cited on page 75)
- Ramos, A. A. & Collados, M. 2008, *Applied Optics*, 47, 2541 (cited on page 47)
- Rasool, S. I. & de Bergh, C. 1970, *Nature*, 226, 1037 (cited on page 2)
- Remer, L. A., Kaufman, Y. J., Tanré, D., et al. 2005, *Journal of Atmospheric Sciences*, 62, 947 (cited on pages 14 and 127)
- Rietjens, J. H. H., van Harten, G., Bekkers, D., et al. 2014, To be submitted (cited on pages 47, 49, 53, 56, 68, 105, and 119)
- Rodenhuis, M., Snik, F., van Harten, G., Hoeijmakers, J., & Keller, C. U. 2014, in *Society of Photo-Optical Instrumentation Engineers (SPIE) Conference Series*, Vol. 9099, *Society of Photo-Optical Instrumentation Engineers (SPIE) Conference Series* (cited on page 25)
- Sabatke, D., Locke, A. M., Dereniak, E. L., & McMillan, R. W. 2003, *Optics Express*, 11, 2940 (cited on pages 53 and 69)
- Salomonson, V. V., Barnes, W. L., Maymon, P. W., Montgomery, H. E., & Ostrow, H. 1989, *IEEE Transactions on Geoscience and Remote Sensing*, 27, 145 (cited on page 14)
- Schaap, M., Apituley, A., Timmermans, R. M. A., Koelemeijer, R. B. A., & de Leeuw, G. 2009, *Atmospheric Chemistry & Physics*, 9, 909 (cited on page 7)

- Schläppi, B., Altwegg, K., Balsiger, H., et al. 2010, *Journal of Geophysical Research: Space Physics*, 115, A12313 (cited on page 66)
- Schott. 2011, *Optical Glass – Description of Properties* (cited on page 59)
- Schott. 2013, *Optical Glass – Data Sheets Inquiry Glass* (cited on page 60)
- Schwartz, S. E. 2004, *Journal of the Air & Waste Management Association*, 54, 1351 (cited on page 15)
- Semel, M., Donati, J.-F., & Rees, D. E. 1993, *Astronomy and Astrophysics*, 278, 231 (cited on pages 19 and 46)
- Snik, F., Craven-Jones, J., Escuti, M., et al. 2014, in *Proceedings of SPIE, Vol. 9099, Polarization: Measurement, Analysis, and Remote Sensing XI* (cited on pages 46 and 74)
- Snik, F., Karalidi, T., Keller, C., et al. 2008, in *Society of Photo-Optical Instrumentation Engineers (SPIE) Conference Series, Vol. 7010, Society of Photo-Optical Instrumentation Engineers (SPIE) Conference Series* (cited on pages 20 and 77)
- Snik, F., Karalidi, T., & Keller, C. U. 2009, *Applied Optics*, 48, 1337 (cited on pages 19, 30, 46, 47, 49, 61, 74, 76, 99, 116, 117, and 118)
- Snik, F. & Keller, C. U. 2013, in *Planets, Stars and Stellar Systems. Volume 2: Astronomical Techniques, Software and Data*, ed. T. D. Oswalt & H. E. Bond (Springer), 175–221 (cited on pages 20, 29, 46, and 119)
- Snik, F., Rietjens, J. H. H., van Harten, G., et al. 2010, in *Society of Photo-Optical Instrumentation Engineers (SPIE) Conference Series, Vol. 7731, Society of Photo-Optical Instrumentation Engineers (SPIE) Conference Series* (cited on pages 32, 33, and 37)
- Snik, F., van Harten, G., Navarro, R., et al. 2012, in *Society of Photo-Optical Instrumentation Engineers (SPIE) Conference Series, Vol. 8446, Society of Photo-Optical Instrumentation Engineers (SPIE) Conference Series* (cited on page 25)
- Sparks, W., Germer, T. A., MacKenty, J. W., & Snik, F. 2012, *Applied Optics*, 51, 5495 (cited on pages 25, 46, 49, and 116)
- Stam, D. M., De Haan, J. F., Hovenier, J. W., & Stammes, P. 1999, *Journal of Geophysical Research*, 104, 16843 (cited on pages 40, 118, and 127)
- Stam, D. M., Laan, E., Snik, F., et al. 2008, *LPI Contributions*, 1447, 9078 (cited on page 32)
- Stammes, P., Kuik, F., & de Haan, J. F. 1994, in *Proceedings of the Progress in Electromagnetics Research Symposium [CD-ROM]* (cited on pages 118, 127, and 128)
- Sterzik, M. F., Bagnulo, S., & Palle, E. 2012, *Nature*, 483, 64 (cited on page 2)
- Taniguchi, A., Oka, K., Okabe, H., & Hayakawa, M. 2006, *Optics Letters*, 31, 3279 (cited on page 47)
- Tanré, D., Bréon, F. M., Deuzé, J. L., et al. 2011, *Atmospheric Measurement Techniques*, 4, 1383 (cited on pages 14, 15, and 75)

- Tomczyk, S., Casini, R., de Wijn, A. G., & Nelson, P. G. 2010, *Applied Optics*, 49, 3580 (cited on page 25)
- Twomey, S. 1977, *Journal of Atmospheric Sciences*, 34, 1149 (cited on page 4)
- Tyo, J. S. 2002, *Applied Optics*, 41, 619 (cited on pages 24, 47, and 50)
- Tyo, J. S., Goldstein, D. L., Chenault, D. B., & Shaw, J. A. 2006, *Applied Optics*, 45, 5453 (cited on pages 46 and 119)
- van Harten, G., de Boer, J., Rietjens, J. H. H., et al. 2014a, *Atmospheric Measurement Techniques Discussions*, 7, 5741 (cited on pages 118 and 126)
- van Harten, G., Rietjens, J. H. H., Snik, F., Smit, J. M., & Keller, C. U. 2014b, To be submitted (cited on pages 74, 76, 79, 83, 94, and 105)
- van Harten, G., Snik, F., Rietjens, J. H. H., et al. 2011, in *Society of Photo-Optical Instrumentation Engineers (SPIE) Conference Series*, Vol. 8160, *Society of Photo-Optical Instrumentation Engineers (SPIE) Conference Series* (cited on pages 77, 83, 99, and 118)
- van Harten, G., Snik, F., Rietjens, J. H. H., Smit, J. M., & Keller, C. U. 2014c, *Applied Optics*, 53, 4187 (cited on pages 46, 49, 74, 76, 80, 100, and 104)
- Vaughan, M. A., Young, S. A., Winker, D. M., et al. 2004, in *Society of Photo-Optical Instrumentation Engineers (SPIE) Conference Series*, Vol. 5575, *Laser Radar Techniques for Atmospheric Sensing*, ed. U. N. Singh, 16–30 (cited on page 127)
- Waquet, F., Cornet, C., Deuzé, J.-L., et al. 2013, *Atmospheric Measurement Techniques*, 6, 991 (cited on page 15)
- Wood, B. E., Uy, O. M., Green, B. D., et al. 2003, in *ESA Special Publication*, Vol. 540, *Materials in a Space Environment*, ed. K. Fletcher, 503–508 (cited on page 67)
- Wu, W.-D., Wang, Z.-B., Wang, H.-L., & Zhang, S. 2009, *Optoelectronics Letters*, 5, 202 (cited on page 58)
- Zallat, J., S, A., & Stoll, M. P. 2006, *Journal of Optics A: Pure and Applied Optics*, 8, 807 (cited on page 47)

Samenvatting

Fijn stof en hun effecten

Het nauwkeurig in kaart brengen van fijn stof in de lucht, zoals zand en zeezout, maar ook roet uit dieselmotoren en fabrieken, is belangrijk vanwege hun effecten op volksgezondheid en klimaat.

Deeltjes kleiner dan 10 micrometer (10 keer zo klein als de diameter van een haar) kunnen bij het inademen in de longen terechtkomen. Hoe fijner het stof hoe dieper het kan doordringen in de luchtwegen, tot in het bloed waar het hart- en vaatziekten kan veroorzaken. De schadelijkheid hangt ook af van de chemische samenstelling van het fijn stof; roet is bijzonder schadelijk, terwijl zeezout onschuldig is. Verhoogde fijn stof concentraties leiden tot acute klachten, met name bij mensen met astma en COPD, maar ook langdurige blootstelling aan concentraties die binnen de Europese normen vallen, vermindert de levensverwachting met gemiddeld een jaar.

Fijn stof heeft ook een grote, maar tegelijkertijd erg onzekere invloed op het klimaat. Zoals CO₂ de straling van de zon vasthoudt in de atmosfeer, en daarmee zorgt voor opwarming van de aarde, zo reflecteert fijn stof het zonlicht vooral terug de ruimte in, en heeft daarmee een afkoelende werking. Bovendien kan waterdamp aan fijn stof blijven plakken, en daarmee druppeltjes en wolken vormen, die op hun beurt nog meer zonlicht reflecteren. De precieze mate van afkoeling en wolkenvorming is erg onzeker, en hangt af van de hoeveelheid fijn stof, de grootte van de deeltjes, en hun chemische samenstelling. Om de onzekerheid te verkleinen zijn frequente, wereldwijde fijn stof metingen nodig, met een aanzienlijk hogere nauwkeurigheid dan de huidige meetapparatuur.

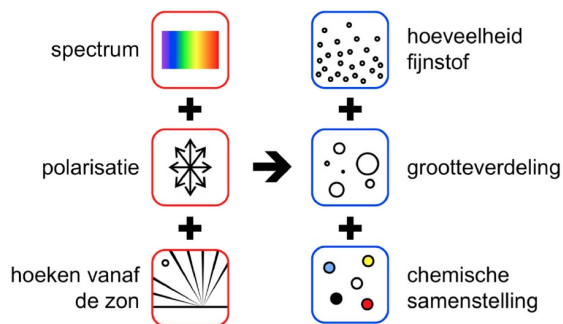
Fijn stof meten

De meeste fijn stof metingen in Nederland worden verricht door het Rijksinstituut voor Volksgezondheid en Milieu (RIVM, <http://www.lml.rivm.nl>), om te controleren of de luchtkwaliteit voldoet aan de Europese normen. Op zo'n 60 locaties verspreid over het land staan meethutten die lucht aanzuigen en deeltjes kleiner dan 10 en 2,5 micrometer eruit filteren. Die worden vervolgens gewogen, en eventueel in een laboratorium geanalyseerd op chemische samenstelling. Het voordeel van

deze manier van meten is dat het een directe meting geeft van de fijn stof concentratie en grootte op grond niveau, daar waar het wordt ingeademd, maar de dekking is erg beperkt, en de chemische analyse is een arbeidsintensief proces en wordt daardoor zelden uitgevoerd.

Het is ook mogelijk om de hoeveelheid fijn stof in de lucht op afstand te meten, zonder het te vangen. Zogenaamde zonfotometers kijken hiervoor op gezette tijden rechtstreeks naar de zon, en hoe meer stof er in de lucht zit, hoe meer de zon gedimd wordt. Door deze meting door verschillende kleurfilters uit te voeren kan een schatting gemaakt worden van de grootte van de deeltjes, doordat kleine deeltjes vooral blauw zonlicht wegfilteren door het in alle richtingen te verstrooien, terwijl grotere deeltjes de kleuren meer gelijkmatig verstrooien. Dit is duidelijk te zien als je wegwijkt van de zon, zodat je alleen maar verstrooid licht ziet: de luchtmoleculen die nog 1000 keer kleiner zijn dan fijn stof zorgen voor een strak blauwe hemel, terwijl witte wolken bestaan uit druppeltjes die groter zijn dan fijn stof. Fijn stof zelf zorgt voor subtielere kleureffecten, die vooral bij hogere concentraties met het blote oog te zien zijn, zoals bij smog.

Een groot voordeel van het meten van fijn stof met behulp van verstrooid licht is dat het ook vanaf een satelliet toegepast kan worden. Hierdoor is het mogelijk om de volledige aarde in slechts enkele dagen in groot detail in kaart te brengen. Terwijl de satelliet over een stuk atmosfeer vliegt wordt het vanuit verschillende hoeken en in verschillende kleuren bekeken door het fijn stof meetinstrument. Maar om echt nauwkeurig de hoeveelheid fijn stof, de grootte van de deeltjes, en de chemische samenstelling te kunnen bepalen, moet nog een eigenschap van het licht gemeten worden: de polarisatie. Licht is een elektrisch golfje dat in een bepaalde richting trilt terwijl het zich voortbeweegt, zoals je een golf kunt maken door een touw op en neer te schudden. De richting waarin het golfje trilt noemen we de polarisatie-richting van het licht. In de praktijk zien we altijd vele lichtgolfjes tegelijk, meestal



Figuur 6.7: Fijn stof in de lucht verstrooit inkomend zonlicht in verschillende richtingen. Door de kleuren en de polarisatie van het verstrooid licht te meten onder verschillende hoeken kunnen we de hoeveelheid fijn stof bepalen, evenals de grootte van de deeltjes en hun chemische samenstelling. *Bron: <http://www.ispex.nl>.*

met verschillende polarisatierichtingen, waardoor we het beschrijven met de netto polarisatierichting en de graad van polarisatie die aangeeft welke fractie van het licht deze voorkeursrichting heeft.

Polarisatie meten

Het enige instrument dat vanaf een satelliet fijn stof metingen heeft uitgevoerd met behulp van polarisatie is het Franse POLDER (POLARization and Directionality of the Earth's Reflectances), dat in gebruik was van 2004 tot 2013. Hoewel het succesvol bleek in het gelijktijdig karakteriseren van fijn stof en wolken, en daarmee het volledige effect van fijn stof op het klimaat kan onderzoeken, om een echte doorbraak in het klimaat onderzoek te bewerkstelligen is een veel nauwkeuriger polarisatiemeting nodig. Met dat doel heeft NASA de APS (Aerosol Polarimetry Sensor) ontwikkeld, die helaas in 2011 tijdens de lancering in de Grote Oceaan is neergestort. Op dit moment is er wereldwijd een handvol nieuwe instrument concepten in ontwikkeling, waaronder het Nederlandse SPEX (Spectropolarimeter for Planetary EXploration), dat het onderwerp is van dit proefschrift. Deze instrumenten gebruiken fundamenteel verschillende methodes om polarisatie te meten, wat een directe weerslag heeft op de nauwkeurigheid van de meting. Polarisatie is niet zichtbaar met het blote oog, en is zelfs niet direct waarneembaar met professionele meetapparatuur. Om het toch te kunnen meten wordt een filter gebruikt dat alleen licht met een polarisatie in een bepaalde richting doorlaat. Door dit filter rond te draaien, en de verandering in de intensiteit van het doorgelaten licht te meten, kan de hoeveelheid polarisatie en de richting ervan gereconstrueerd worden. Dit experiment kunt u zelf uitvoeren door een Polaroid zonnebril rond te draaien voor het polariserende scherm van een laptop of mobiele telefoon. Een groot nadeel van een roterend polarisatiefilter, zoals gebruikt in het POLDER instrument, is dat elke verandering in intensiteit, ook die door de verplaatsing van de satelliet tijdens de verschillende filterstanden, geïnterpreteerd wordt als polarisatie. Dit probleem is opgelost in APS door het instrument uit te rusten met meerdere camera's, elk met een polarisatiefilter in een andere richting, zodat de metingen gelijktijdig genomen kunnen worden. Het is belangrijk dat de camera's precies hetzelfde zijn om valse polarisatie signalen te voorkomen. Ons SPEX instrument gebruikt een derde meetmethode, waarbij de polarisatie informatie wordt opgeslagen in een enkele meting van het kleuren spectrum. De omslag van dit proefschrift laat elf metingen zien waarbij de graad van polarisatie geleidelijk toeneemt van volledig ongepolariseerd (links) tot volledig gepolariseerd (rechts). De graad van polarisatie wordt dus uitgedrukt in het contrast tussen de donkere en lichte banden in het spectrum, en als de polarisatierichting draait verschuiven de donkere en lichte banden omhoog of omlaag. Misschien herkent u de beelden op de omslag wel van uw eigen smartphone, waarmee u zelf fijn stof kunt meten met behulp van het iSPEX opzetstukje dat gebruikmaakt van hetzelfde meetprincipe (<http://www.ispex.nl>).

Dit proefschrift

Hoofdstuk 2 is geschreven aan het begin van het promotie onderzoek, en presenteert het optische en mechanische ontwerp van het SPEX instrument, en het prototype dat zojuist ontwikkeld was. Ook worden de stappen beschreven die noodzakelijk zijn om de camerabeelden te verwerken tot kleurafhankelijke intensiteiten en polarisatiegraden en richtingen. Met behulp van een polarisatiefilter wordt volledig gepolariseerd licht aangeboden, waarna we kunnen corrigeren voor het feit dat SPEX minder dan 100% polarisatie meet, wat ook afhankelijk blijkt te zijn van de kleur van het licht en de richting van de polarisatie. Vervolgens maken we gedeeltelijk gepolariseerd licht aan met een geleidelijk toenemende graad van polarisatie, door licht door een glasplaat te schijnen terwijl deze langzaam gekanteld wordt. We kennen de polarisatie eigenschappen van de lichtbron en de glasplaat niet goed genoeg om de absolute graad van polarisatie te kunnen kalibreren, maar we weten wel precies de toename in polarisatie als de glasplaat een beetje meer gekanteld wordt. Uit deze metingen blijkt dat SPEX een verandering in de graad van polarisatie kan waarnemen van 0.02%. Dit is een belangrijk resultaat, omdat de gewenste nauwkeurigheid voor fijn stof metingen vanaf een satelliet slechts in de orde van 0.2% ligt. Tenslotte worden de eerste testmetingen van de blauwe lucht vanaf de grond beschreven, op basis waarvan verschillende verbeteringen doorgevoerd zijn aan het instrument en de dataverwerking.

Hoofdstuk 3 presenteert een zo compleet mogelijke theoretische foutenanalyse voor het SPEX instrument. Verschillende foutenbronnen worden geïdentificeerd, en onderverdeeld naar gelang hun effect na kalibratie: statische fouten, zoals optische componenten die scheef staan, zorgen ervoor dat het instrument niet optimaal werkt, maar wel op een voorspelbare manier, terwijl dynamische fouten, bijvoorbeeld door temperatuurgevoeligheid of vervuiling die neerslaat op het instrument na lancering, onherroepelijk zorgen voor fouten in de polarisatiemeting. Vervolgens wordt het SPEX instrument gesimuleerd op de computer, inclusief alle foutenbronnen en de kalibratie ervan op aarde, waaruit met grote zekerheid blijkt dat SPEX in de ruimte zal voldoen aan de vereiste polarisatie nauwkeurigheid voor fijn stof metingen, zonder dat extra kalibraties nodig zijn na de lancering.

Hoofdstuk 4 heeft als doel om de nauwkeurigheid van polarisatiemetingen met SPEX in het lab experimenteel vast te stellen. Hiertoe is een kalibratielichtbron ontwikkeld die eerst grondig depolariseert, en vervolgens gedeeltelijke polarisatie aanmaakt met behulp van kantelbare glasplaten. Hoewel deze glasplaten zorgvuldig geselecteerd zijn, zijn hun polarisatie eigenschappen nog steeds onvoldoende bekend om SPEX op de vereiste nauwkeurigheid te kalibreren. Speciaal om de polarisatie van de kalibratielichtbron te karakteriseren is nog een meetinstrument ontwikkeld, gebaseerd op een roterend polarisatiefilter, maar aangezien deze ook gekalibreerd moet worden, ontstaat een kip-en-eiprobleem. Een uitgebreide vergelijking tussen deze kalibratiemetingen, verschillende soorten kalibratiemetingen met SPEX, en een

model van de kalibratielichtbron, laat uiteindelijk overeenstemming zien precies op het nauwkeurighedsniveau waarop SPEX geacht wordt fijn stof te meten.

Zodra de uitstekende polarisatie eigenschappen van SPEX aan het licht kwamen, toonde het RIVM interesse in een eigen SPEX instrument, om te onderzoeken of het mogelijk is om in een toekomstig meetnetwerk vanaf de grond fijn stof te karakteriseren. **Hoofdstuk 5** presenteert dit groundSPEX instrument, een relatief goedkoop en weerbestendig instrument op een gemotoriseerd statief om autonoom de polarisatie van de hemel te meten. De ruis en systematische fouten in de metingen van intensiteit en polarisatie worden geanalyseerd, en hoe ze doorwerken naar de fijn stof eigenschappen die uit de metingen afgeleid worden. Het instrument wordt voor het eerst ingezet gedurende vier zonnige dagen in 2013, waarbij de hoeveelheid fijn stof, de grootte van de deeltjes, en hun chemische samenstelling wordt gemeten, die in overeenstemming blijken te zijn met nabijgelegen instrumenten. GroundSPEX is overgedragen aan het RIVM, die het permanent zal gaan gebruiken.

Hoofdstuk 6 introduceert nieuwe functionaliteiten die mogelijk zijn met een SPEX instrument dat niet één maar altijd twee spectra tegelijk meet, zoals het SPEX prototype en groundSPEX. De twee spectra zijn precies uit fase, zodat de donkere en de lichte polarisatie banden omgewisseld zijn. Hierdoor is de som van de twee spectra weer het complete intensiteit spectrum, zonder donkere banden erin. Dit komt de nauwkeurigheid van de intensiteit en polarisatiemetingen sterk ten goede, omdat er soms donkere banden in het spectrum zitten waarvan onduidelijk is of het door de polarisatie komt, of door een moleculaire absorptieband in het intensiteit spectrum. Als de som van de twee spectra toch nog donkere banden vertoont, duidt dit op een transmissie verschil tussen de twee spectra. Dit gegeven kan gebruikt worden om eenmaal op de satelliet zonder extra kalibratie apparatuur de transmissie te bepalen, en ervoor te corrigeren in de dataverwerking, wat leidt tot een sterke verbetering van de meetnauwkeurigheid. Doordat SPEX uitgerust is met een spectrograaf kan de polarisatie ook op hoge spectrale resolutie gemeten worden. Een demonstratie hiervan wordt gegeven met een polarisatie in de zuurstof-A absorptieband, die meerdere procenten af blijkt te wijken van de polarisatie rondom de band. Aangezien de atmosfeer minder transparant is in een absorptieband kijkt het instrument effectief op een andere hoogte in de atmosfeer, zodat de unieke spectrale resolutie van SPEX het mogelijk maakt de hoogteverdeling van fijn stof te bepalen.

Curriculum Vitae

Gerard van Harten was born on November 11, 1984, in Katwijk, the Netherlands. He spent most of his childhood in Amersfoort, where he graduated from high school in 2002, with a focus on natural and life sciences. His passion for experimental (astro)physics led to an MSc degree in Astrophysics from Utrecht University in 2010. For the MSc thesis in the Experimental Astrophysics group of professor Christoph Keller, he developed and characterized the first breadboard model of the SPEX spectropolarimeter, and performed clear-sky measurements including forward aerosol modeling.

Gerard continued his work on SPEX as a PhD candidate, which resulted in this thesis, describing the instrument development, polarimetric error analysis and calibration, ground-based aerosol characterization, and absorption band polarimetry. Results of his work were presented in refereed journals and at various international conferences and institute visits.

Gerard executed several projects parallel to his thesis work, including the development of polychromatic polarization modulators for the 300–2500 nm X-shooter spectrograph on the Very Large Telescope and for the ExPo imaging polarimeter on the William Herschel Telescope. Furthermore, he was involved in hardware and software development for iSPEX, the network of smartphone spectropolarimeters that successfully mapped aerosol optical thickness throughout the Netherlands through citizen science.

Gerard will continue to work on high-accuracy polarimetry for remote aerosol characterization, starting in 2014 with preparations for an airborne SPEX instrument at SRON Netherlands Institute for Space Research, followed in 2015 by in-flight characterization of the AirMSPI and AirMSPI-2 airborne imaging polarimeters, and in-flight intercomparisons with other polarimeters, including SPEX, at the NASA Jet Propulsion Laboratory in California.

Acknowledgements

Many people have inspired me on the way that ultimately led to this thesis. In keeping with the Leiden tradition of not acknowledging official supervisors, I would like to start by thanking Jeroen Rietjens for being such an excellent mentor and sparring partner during the past four years. Other coworkers who taught me a lot, but just outside the specific work that is described in this thesis, are Alfred de Wijn (introduction to polychromatic modulation), Thijs Krijger and Ralph Snel (discussions about the total polarization of multiple mirrors in 3D), and Michiel Rodenhuis (observing at the William Herschel Telescope). It was a great pleasure to work with several students for their BSc and MSc projects: Erik Lumens (measuring circular polarization of trees), Bart Jansen (creating a SPEX demonstration setup for live monitoring of Mie particle growth), Jos de Boer (developing groundSPEX), Pierre Hendrix (modeling polarized spectral fringes), Renia Diamantopoulou (developing a polychromatic ellipsometer), David Bekkers and Annelies Vreeker (characterizing the SPEX calibration stimulus), Ritse Heinsbroek (characterizing iSPEX), and Ronniy Joseph (commissioning the polychromatic integral field unit for ExPo). The mechanical and electronic development of groundSPEX and the calibration stimulus for the SPEX prototype would not have been possible without the expertise of the engineers at Scientific Instrumentation of Utrecht University, Marcel Rossewijn, Christian Straman, Dante Kilian, Jos van Gemert, Sander Deelen, and Kees van der Neut, and at the Finemechanical Department of Leiden University, Raphaël Zwier. I thank the greater remote sensing community at Cabauw for unlimited practical support and scientific insights: Marcel Brinkenbergh, Alfons Driever, Henk Klein Baltink, Cor van Oort, Piet Stammes, René van der Hoff, Jan Vonk, Stijn Berkhout, and Marty Haaima. I truly enjoyed sharing the office, or really the countless stories and the mutual mental support, with my buddies Aswin, Guus, Maria, Tim, and Visa. Maria and Tim, it is a great honor that you will be my paranymphs. I am greatly indebted to my family and friends in Amersfoort, Utrecht and Leiden, and in particular the ones who are not bound by place or time, for being so supportive, encouraging, and patient. Leah, thank you so much for being such a great person.

The characterization of aerosols in the Earth's atmosphere is important, because of their impact on public health and climate. This requires a new generation of accurate space-based instruments that measure the atmospheric radiance and polarization at multiple wavelengths and scattering angles. This thesis describes the development, characterization, and field-deployment of such an instrument, the Spectropolarimeter for Planetary EXploration (SPEX).